Electronic, magnetic and thermodynamic properties of magnetic shape memory alloys from first principles

Dissertation

zur Erlangung des Grades
"Doktor der Naturwissenschaften"

an der Fakultät für Physik
der Universität Duisburg-Essen

vorgelegt von
Dipl.-Phys. Mario Siewert
aus Duisburg, Deutschland

Erstgutachter: Prof. Dr. P. Entel
Zweitgutachter: Prof. Dr. P. H. Dederichs

Tag der mündlichen Prüfung: 5. Dezember 2012

Zusammenfassung

Der magnetische Formgedächtnis-Effekt ist eine funktionale Eigenschaft die von wissenschaftlicher, aber auch industrieller Bedeutung ist. In magnetischen Formgedächtnis-Legierungen lassen sich durch das Anlegen moderater magnetischer Felder makroskopisch messbare Verzerrungen erzielen. Die Physik magnetischer Formgedächtnis-Materialien wird durch die Wechselwirkung magnetischer und struktureller Phasen bestimmt, da die Materialien sowohl einen ferromagnetischen als auch einen martensitischen Phasenübergang zeigen. Die Heusler-Legierung Ni_2MnGa ist ein vielversprechendes magnetisches Formgedächtnis-Material, dass allerdings eine für industrielle Anwendungen zu niedrige martensitische Übergangstemperatur aufweist und vergleichsweise spröde ist.

In der vorliegenden Arbeit wurden die bisherigen in der Literatur erwähnten Untersuchungen an Ni_2MnGa durch *Ab Initio* Untersuchungen zum Einfluss der Beiträge von Gitterschwingungen, magnetischen Anregungen, elektronischen Korrelationen und Fermiflächennesting auf den Martensit-Übergang erweitert. Es wird gezeigt, dass der martensitische Phasenübergang von mehreren Beiträgen getrieben wird.

In einem nächsten Schritt wurden Mangan-reiche Zusammensetzungen der Legierungssysteme Ni-Mn-Z ($Z = $ Ga, In, Sn, Sb) untersucht, die hohe martensitische Übergangstemperaturen aufweisen. Es zeigt sich, dass ein direkter Ansatz, der die Energiedifferenzen zwischen Austenit und Martensit, die in den Dichtefunktionalrechnungen auftreten, mit der Übergangstemperatur identifiziert zu qualitativen und teilweise sogar quantitativen Übereinstimmungen mit experimentellen Ergebnissen führt. Der Ansatz, der nicht-stöchiometrische Zusammensetzungen über Superzellen berücksichtigt, ermöglicht die Berechnung vollständiger Phasendiagramme mittels *Ab Initio* Methoden. Die dazu erforderliche Rechenleistung steht in einem angemessenen Verhältnis zu den erzielbaren Resultaten.

In einem weiteren Schritt wurden die vorgestellten Methoden auf die Legierungssysteme Ni-Pt-Mn-Z ($Z = $ Ga, Sn) angewandt, die noch nicht ausführlich in der Literatur behandelt wurden. Die partielle Substitution von Nickel durch Platin ist von besonderem Interesse, da diese die Valenzelektronenkonzentration nicht verändert. Es zeigt sich, dass durch das Hinzufügen von Platin höhere Übergangstemperaturen erwartet werden. Kürzlich veröffentlichte experimentelle Arbeiten bestätigen die vielversprechenden Eigenschaften dieser Legierungssysteme.

Eine weitere magnetische Formgedächtnis-Legierung die im Rahmen dieser Arbeit untersucht wurde ist Co-Ni-Ga. Dieses System zeichnet sich durch die Abwesenheit weicher Phononen und antiferromagnetischer Wechselwirkungen aus, die in Ni-Mn-Ga beobachtet werden. Die Tendenz, dass die erwarteten martensitischen Übergangstemperaturen bei Erhöhung der Valenzelektronenkonzentration ansteigen, lässt sich hingegen auch in Co-Ni-Ga beobachten.

Abstract

The magnetic shape memory effect (MSME) is a functional property which is of outmost interest from a scientific point of view but also regarding industrial applications. Magnetic shape memory alloys (MSMA) allow to obtain large magnetic field induced strains (MFIS) in moderate magnetic fields and hence qualify for actuator and sensor devices. The underlying physics of MSMAs is governed by an interplay between different structural and magnetic phases as a ferromagnetic and a martensitic transition are required for the appearance of the MSME. Several alloys are known to show the MSME. From these Ni_2MnGa is promising with regard to industrial applications but still shows too low operating temperatures and is rather brittle.

In this thesis the comprehensive investigation of Ni_2MnGa which was undertaken by a lot of scientific groups in the past is expanded by an investigation of the different contributions to the martensitic transformation (MT) using first-principles calculations. In particular the influence of lattice vibrations, magnetic excitations, correlation effects and Fermi surface nesting on the MT are investigated. It is shown that the structural phase transition that appears in Ni_2MnGa is driven by several martensitic driving forces.

In a further step the Mn-rich compositions of the alloys systems Ni-Mn-Z ($Z =$ Ga, In, Sn, Sb) have been investigated. The Mn-rich compositions are of particular interest as they show increased MT temperatures. It turns out that a simple approach which relates the transformation temperature to the energy difference between the austenite and martensite structure which appears in first-principles calculations yields good qualitative and in some cases even quantitative agreement with experimental results. The approach which models off-stoichiometric compositions by using supercells makes it possible to calculate the transformation temperatures of off-stoichiometric compositions within feasible computational demand. This gives rise to the calculation of complete phase diagrams by *ab initio* methods.

In the next step, the established methods which have been applied to phase diagrams which are already known experimentally have been applied to the alloy systems Ni-Pt-Mn-Z ($Z =$ Ga, Sn) which has not been discussed extensively in the literature before. The (partial) substitution of Ni by Pt is interesting as it is an isoelectronic substitution which sustains the valence electron concentration e/a. It turns out that higher martensitic transformation temperatures are expected when adding platinum to the alloys. The promising properties of such alloys have recently been confirmed experimentally.

Another magnetic shape memory alloy which has been studied within this thesis is Co-Ni-Ga. This system is of special interest as the phonon softening that is present in Ni_2MnGa as well as antiferromagnetic interactions which are found in Mn-rich compositions of the latter alloy are absent in Co-Ni-Ga. Nevertheless, the basic trend that the martensitic transformation temperature increases with e/a is also observed in this alloy system.

Contents

List of Figures

List of Tables

Chapter 1

Introduction

Ferromagnetic shape memory alloys are of industrial relevance as they may reveal large magnetic field induced strains (MFIS) which qualify these materials for actuator or sensor applications. So far, the largest strains have been achieved for the Heusler compound Ni_2MnGa. However, due to its brittleness and the limited operating temperatures of devices based on this material it is of industrial but also scientific interest to search for new ferromagnetic shape memory alloys which are less brittle and reveal higher martensitic transformation temperatures.

The aim of this work is the first-principles investigation of ferromagnetic shape memory alloys which have not been studied extensively by other research groups in the past and to predict specific compositions which reveal promising material properties with regard to the magnetic shape memory effect. The methods that are used, in particular the methods of density functional theory which are applied in the calculations and the theoretical description of lattice vibrations and spin waves is introduced in chapter 2 of this thesis. Chapter 3 contains a short introduction on the shape memory effect and the magnetic shape memory effect and also includes a summary of the properties of Ni_2MnGa.

As the martensitic transformation is a requirement for the appearance of the magnetic shape memory effect its origin and the different driving forces of the transition are investigated in detail for the magnetic shape memory reference compound Ni_2MnGa in chapter 4 which actually is the first chapter which contains results.

In chapter 5 the methods that have been used to study the martensitic transformation in Ni_2MnGa are applied to the four alloy series Ni-Mn-Z ($Z =$ Ga, In, Sn, Sb), in particular the Mn-rich sites of the phase diagrams of these systems which reveal increased martensitic transformation temperatures. It is shown that *ab initio* calculations are able to model the phase diagrams of the investigated alloys and to obtain a qualitative and in some cases even quantitative agreement between theory and experiment. Moreover the calculations based on density functional theory allow to investigate the origin of the phase transformation by studying the changes of the magnetic and electronic properties that arise when changing the atomic composition in detail.

Chapter 6 contains the results of the *ab initio* investigation of Ni-Pt-Mn-Z ($Z =$ Ga, Sn). It turns out that the substitution of Ni by Pt which keeps the valence electron concentration constant ($e/a = 7.5$) increases the predicted transformation temperatures.

Finally in chapter 7 the ferromagnetic shape memory system Co-Ni-Ga will be discussed.

This alloy is remarkable as neutron scattering measurements suggest that the martensitic transformation is not driven by phonon softening as is the case in Ni_2MnGa. In agreement with experimental results the *ab initio* calculations suggest that there exists a competition between different types of structures in Co-Ni-Ga which results in disordered structures.

Chapter 8 contains a short conclusion. In particular, all obtained results are once again briefly summarized in this chapter.

Very recently it has been discovered that several of the Heusler compounds which have been studied here are able to lower their energy not only by a tetragonal transformation of their cubic structure but also by transforming from the bcc- to a nearly hcp-structure. This issue as well as the importance of magnetic excitations will be briefly discussed in the outlook given in chapter 9.

Chapter 2

Theoretical background

2.1 Density functional theory

When trying to calculate the electronic structure of a solid, problems arise due to the large number of interacting particles. Density functional theory provides an approach to overcome this problem by making some assumptions that have proven to correctly describe many properties of solid state physics in the past.

This section describes the basic ideas and steps towards the application of density functional theory. It is mainly based on the lecture about density functional theory and molecular dynamics given by R. Meyer in the years 2006 and 2007 at the University of Duisburg-Essen [1], the book *Electronic structure* by Richard M. Martin [2], and the German summary in Ref. [3].

A quantum-mechanic many body problem is described by the solution of Schrödinger's equation containing the Hamilton-Operator

$$\begin{aligned}\mathbf{H} = &-\frac{\hbar}{2m_e}\sum_i \nabla_i^2 - \frac{1}{4\pi\epsilon_0}\sum_{i,I}\frac{Z_I e^2}{|\mathbf{r}_i - \mathbf{R}_I|} + \frac{1}{8\pi\epsilon_0}\sum_{i\neq j}\frac{e^2}{|\mathbf{r}_i - \mathbf{r}_j|} \\ &-\sum_I \frac{\hbar^2}{2M_I}\nabla_I^2 + \frac{1}{8\pi\epsilon_0}\sum_{I\neq J}\frac{Z_I Z_J e^2}{|\mathbf{R}_I - \mathbf{R}_J|}\end{aligned} \tag{2.1}$$

where i denotes an indice that is related to the electrons and I denotes an indice that is related to the atomic cores. Thus $\mathbf{r}_i$ gives the position of an electron and M_I, Z_I, and $\mathbf{R}_I$ are related to the mass, the proton number and the position of an atomic core.

It is clear that due to the large number of interacting particles in a solid a numerical solution of this problem becomes nearly impossible. Therefore, further assumptions are needed to simplify the model while at the same time taking care that the model still describes the physical properties of the system.

2.1.1 The Hartree-Fock method

A first approach to find a wave function which minimizes the energy of Schrödinger's equation for the Hamilton operator introduced in equation (2.1) makes use of the Pauli-principle. This states that the ground state many body wavefunction Ψ_0 of a many body system is anti-symmetric in the case of electrons (Fermions). The basic idea of the Hartree-Fock method is

therefore to construct a many body wave function Ψ that is built up from several one electron wavefunctions χ_i and is antisymmetric by definition using a Slater determinant

$$\Psi = \frac{1}{\sqrt{N!}} \begin{vmatrix} \chi_1(\mathbf{x}_1) & \chi_2(\mathbf{x}_1) & ... & \chi_N(\mathbf{x}_1) \\ \chi_1(\mathbf{x}_2) & \chi_2(\mathbf{x}_2) & & \chi_N(\mathbf{x}_2) \\ ... & & & ... \\ \chi_1(\mathbf{x}_N) & ... & ... & \chi_N(\mathbf{x}_N) \end{vmatrix} \tag{2.2}$$

where N denotes the number of electrons in the system.

The many body wavefunction Ψ can now be varied by separate variation of the one electron wavefunctions χ_i. As the variational principle

$$H\Psi_0 \leq H\Psi \tag{2.3}$$

states that the wave function of the ground state always has the lowest energy, Ψ_0 can be approximated by minimizing Ψ.

Although the Hartree-Fock method describes a simple approach to find the ground state of a many body system the results are not very accurate in many cases. This is due to the fact that the method completely neglects the correlations between the seperate electrons in the system.

2.1.2 Born-Oppenheimer approximation

As the time scale of changes in the electronic structure is much smaller than the time scale which describes the movement of the ions, the atomic cores can be assumed to be stationary. This means that the kinetic energy of the atomic cores can be neglected. As the ground state energy does not depend on the positions of the atomic cores anymore in this case, the term that describes the Coulomb interaction between the atomic cores ($\frac{1}{8\pi\epsilon_0} \sum_{I \neq J} \frac{Z_I Z_J e^2}{|\mathbf{R}_I - \mathbf{R}_J|}$) is also reduced to a constant value.

The assumption of static atomic cores yields the following Hamilton operator:

$$H_{\mathrm{BO}} = -\frac{\hbar^2}{2m_e} \sum_i \nabla_i^2 - \frac{1}{4\pi\epsilon_0} \sum_{i,I} \frac{Z_I e^2}{|\mathbf{r}_i - \mathbf{R}_I|} + \frac{1}{8\pi\epsilon_0} \sum_{i \neq j} \frac{e^2}{|\mathbf{r}_i - \mathbf{r}_j|} + const. \tag{2.4}$$

2.1.3 The theorems of Hohenberg and Kohn

Density functional theory (DFT) is based on the idea to use the electron density $n(\mathbf{r})$ instead of the many body wavefunction Ψ as the basic variable that describes all physical properties of the system. A first application of this idea was the Thomas-Fermi model proposed in 1927 [4] which assumed that electrons in a solid can be described in a similar manner as electrons in a free electron gas.

Although the Thomas-Fermi model already yielded feasible results the assumptions made within the model could not be justified coherently. In 1964 Hohenberg and Kohn provided a

justification of the idea to use the electron density as the basic variable [5]. This justification is based upon these two theorems:

- The external potential of a system of interacting particles is uniquely defined (expect for a constant value) by the electron density $n_0(\mathbf{r})$ of the ground state
- The ground state energy is the minimum of the energy functional $E[n]$ that can be defined for any external potential

The proof of the first theorem is done by assuming the existence of two different external potentials V_1 and V_2 which both give the same electron density n_0. In this case the respective Hamilton operators H_1 and H_2 that belong to V_1 and V_2 only differ regarding the contribution of the external potential. The variational principle says that

$$E_1 = \langle \Psi_1 | H_1 | \Psi_1 \rangle < \langle \Psi_2 | H_1 | \Psi_2 \rangle \tag{2.5}$$

$$E_2 = \langle \Psi_2 | H_2 | \Psi_2 \rangle < \langle \Psi_1 | H_2 | \Psi_1 \rangle \tag{2.6}$$

while at the same time

$$\langle \Psi_2 | H_1 | \Psi_2 \rangle = \langle \Psi_2 | H_2 | \Psi_2 \rangle + \langle \Psi_2 | H_1 - H_2 | \Psi_2 \rangle = E_2 + \int d\mathbf{r} [V_1 - V_2] n_0(\mathbf{r}) \tag{2.7}$$

$$\langle \Psi_1 | H_2 | \Psi_1 \rangle = \langle \Psi_1 | H_1 | \Psi_1 \rangle + \langle \Psi_1 | H_2 - H_1 | \Psi_1 \rangle = E_1 + \int d\mathbf{r} [V_2 - V_1] n_0(\mathbf{r}) \tag{2.8}$$

is valid. If one inserts equation (2.7) in equation (2.5) and equation (2.8) in equation (2.6) and then adds up the two equations one ends up with

$$E_1 + E_2 < E_2 + E_1 \tag{2.9}$$

This contradiction shows that the assumption made in the first theorem always is true which means that all properties of the system are determined by the electron density. This means that the total energy of the system can be described as a functional of the electron density. Due to the variational principle the electron density that minimizes this functional $E[n]$ is the ground state electron density. Thus, the ground state energy can be obtained by a variation of the electron density which is exactly the statement of the second theorem.

The interaction of the electrons with the nuclei can be described in terms of an external potential V_{ext}. Thus, the Hohenberg-Kohn theorems in combination with the Born-Oppenheimer approximation allow to modify the Hamilton operator introduced in equation (2.1) in the following way

$$H = -\frac{\hbar^2}{2m_e} \sum_i \nabla_i^2 + \frac{1}{8\pi\epsilon_0} \sum_{i \neq j} \frac{e^2}{|\mathbf{r}_i - \mathbf{r}_j|} + \int V_{\text{ext}}(\mathbf{r}) n(\mathbf{r}) d\mathbf{r} + const. \tag{2.10}$$

2.1.4 The Kohn-Sham Ansatz

The Hamilton operator given in equation (2.10) still contains the electron-electron interaction and the momentum operator of single electrons that are interacting with each other. The idea behind the Kohn-Sham Ansatz is to replace the electron density of the interacting system by the electron density of a non-interacting reference system [6]. The eigenstates ϕ_i of this auxiliary system are called Kohn-Sham orbitals and the electron density is defined by

$$n(\mathbf{r}) = \sum_i |\phi_i(\mathbf{r})|^2 \tag{2.11}$$

which allows to set up the energy functional based on the Hamilton operator proposed in equation (2.10). The so-called Hartree term describes the Coulomb interaction between the electrons:

$$E_{\text{Hartree}} = \frac{1}{8\pi\epsilon_0} \sum_i \sum_j \int |\phi_i(\mathbf{r})|^2 \frac{1}{|\mathbf{r} - \mathbf{r}'|} |\phi_j(\mathbf{r}')|^2 d\mathbf{r} d\mathbf{r}' \tag{2.12}$$

The complete energy functional can be written as

$$E[n] = -\frac{\hbar^2}{2m_e} \sum_i \langle \phi_i | \nabla^2 | \phi_i \rangle + E_{\text{Hartree}} + E_{\text{xc}}[n] + \int V_{\text{ext}}(\mathbf{r}) n(\mathbf{r}) d\mathbf{r} \tag{2.13}$$

where $E_{\text{xc}}[n]$ denotes the exchange-correlation functional. The exchange-correlation functional compensates the error that is introduced by neglecting the exchange term and the correlation between the electrons (i.e. the difference between the original many particle system and the auxiliary system). Thus, a feasible description of the exchange-correlation functional is needed to obtain proper results in practice.

From the energy functional $E[n]$ the Kohn-Sham equations can be constructed

$$\left[-\frac{\hbar^2}{2m_e} \nabla^2 + \frac{1}{8\pi\epsilon_0} \int \frac{n(\mathbf{r}')}{|\mathbf{r} - \mathbf{r}'|} d\mathbf{r}' + V_{\text{xc}}(\mathbf{r}) + V_{\text{ext}}(\mathbf{r}) \right] \phi_i = \epsilon_i \phi_i \tag{2.14}$$

where $V_{\text{xc}}(\mathbf{r})$ is given by

$$V_{\text{xc}}(\mathbf{r}) = \frac{\delta E_{\text{xc}}[n]}{\delta n(\mathbf{r})} \tag{2.15}$$

and ϵ_i is the eigenenergy of the Kohn-Sham orbital ϕ_i.

In practice, a density functional theory calculation is performed by solving the Kohn-Sham equations for a particular starting value for the electron density $n(\mathbf{r})$. Once the eigensystem for this electron density has been calculated the eigenstates ϕ_i give rise to a new electron density which is generated according to equation (2.11). In the next step the Kohn-Sham equations which now contain the new electron density have to be solved again. The solution then gives rise to a further electron density. In most types of calculations this iterative procedure is repeated until a self-consistent solution is obtained. This means that the change of the electron density between two iterative steps is smaller than a particular convergence criterion.

2.1.5 The local density approximation (LDA)

Expect for the exchange-correlation functional the Kohn-Sham Ansatz is in principle exact. Therefore, the choice of the exchange-correlation functional is of utmost importance (as it has already been pointed out before).

A simple approach to defince E_{xc} is the local density approximation (LDA). This approximation assumes that the electrons in a solid behave just like electrons in a homogenous electron gas. This means that E_{xc} in a specific region only depends on the local electron density in that region:

$$E_{\mathrm{xc,LDA}}[n] = \int n(\mathbf{r})\varepsilon_{\mathrm{xc,hom}}(n(\mathbf{r}))d\mathbf{r} \tag{2.16}$$

Here $\varepsilon_{\mathrm{xc,hom}}(n(\mathbf{r}))$ denotes the exchange-correlation energy per particle in an unpolarized homogenous electron gas with electron density $n(\mathbf{r})$. As there is no analytic description of $\varepsilon_{\mathrm{xc,hom}}(n(\mathbf{r}))$, approximations have to be used in practice. Parameterized descriptions for example can be obtained by quantum Monte Carlo simulations [7, 8].

2.1.6 Spin-dependent density functional theory

So far, the degree of freedom introduced by the spin of the electron was not considered in the calculation of the electron density. Spindependent calculations allow to investigate magnetic systems and can be achieved by splitting up the electron density in a spin-up density $n^{\uparrow}$ and a spin-down density $n^{\downarrow}$. In this case, the Kohn-Sham equations introduced in equation (2.14) are solved seperately for each spin channel. While the charge density is obtained by adding up the densities of the two spin channels ($n^{\uparrow} + n^{\downarrow}$), the so-called spin density is obtained as the difference of the electron densities between the two spin channels ($n^{\uparrow} - n^{\downarrow}$). Spindependent calculations require that the exchange-correlation functionals are modified appropriately. This leads to modifications like the local spin density approximation (LSDA) which is obtained when considering the spin of the electron in the LDA.

2.1.7 The generalized gradient approximation (GGA)

The LDA and LSDA already yield feasible results in many cases. However, the question arises whether there are other approximations for the exchange-correlation functional which qualitatively improve the results. One approach to extend the LDA is the so-called generalized gradient approximation (GGA) [9, 10, 11, 12]. The GGA is a modification of the gradient expansion approximation (GEA) which assumes that the exchange-correlation functional can be improved by not only considering the local electron density as in the LDA but also the gradient of the electron density. In fact, the GEA can be regarded as a Taylor expansion of the LDA taking into account the first order term. It turns out that the GEA itself does not improve the results that have been obtained with LDA. A modification of the exchange-correlation functional in case of large electron densities finally results in the GGA which significantly

outperforms the results obtained with LDA in some cases. In general the exchange-correlation functional of the GGA can be written as

$$E_{\mathrm{xc,GGA}}[n^{\uparrow}, n^{\downarrow}] = \int n(\mathbf{r})\epsilon_{\mathrm{xc,GGA}}(n^{\uparrow}, n^{\downarrow}, |\nabla n^{\uparrow}|, |\nabla n^{\downarrow}|, ...)d\mathbf{r} \quad (2.17)$$

$$= \int n(\mathbf{r})\epsilon_{\mathrm{x,hom}}(n^{\uparrow} + n^{\downarrow})F_{\mathrm{GGA}}(n^{\uparrow}, n^{\downarrow}, |\nabla n^{\uparrow}|, |\nabla n^{\downarrow}|, ...)d\mathbf{r} \quad (2.18)$$

where $\epsilon_{\mathrm{x,hom}}$ is the exchange energy of the unpolarized homogeneous electron gas [2]. In practice, there exist several realizations of the GGA [13, 14].

2.1.8 Correlation effects

For strongly correlated systems the LDA as well as the GGA fail which for example is expressed in the underestimation of band gaps of semiconductors [15, 16]. The reason for this behaviour is found in the mean-field treatment of the Coulomb repulsion between the electrons which does not take into account strong electronic correlations [17]. In particular, when making use of the LDA exchange-correlation functional the potential of the Kohn-Sham orbitals does not depend on the occupancy of the orbitals [16]. However, in case of strong on-site correlations the addition of an electron to a localized site which already contains an electron requires an additional energy U [18]. This term which is called "Hubbard U" stems from the Hubbard model which was introduced by J. Hubbard in 1963 and takes into account the on-site Coulomb repulsion by an additional term in the Hamiltonian [19]. The introduction of the "Hubbard U" in the energy functional of LDA gives rise to the so-called LDA+U method [20, 21, 22]. The basic idea behind this method will be described in the following based on the explanation in the comprehensive review by Anisimov *et al.* [23]. In the LDA+U method the on-site Coulomb interaction of localized electrons, i.e. d- or f-electrons, is considered in a mean-field like manner by the term

$$\tfrac{1}{2}U\sum_{i\neq j} n_i n_j \quad (2.19)$$

which is added to the energy functional of the local density approximation (LDA). Here, n_i denotes the occupation of the d-orbital i. The total number of localized d electrons is therefore defined as $N = \sum_i n_i$. As however, the localized electrons are already contained in the LDA functional the problem of this so-called double counting is solved by subtracting the term $UN(N-1)/2$ from the LDA functional. The energy functional of the LDA+U method therefore becomes

$$E_{\mathrm{LDA+U}} = E_{\mathrm{LDA}} - UN(N-1)/2 + \tfrac{1}{2}U\textstyle\sum_{i\neq j} n_i n_j. \quad (2.20)$$

The orbital energies ϵ_i are derived by the derivation of equation (2.20) with respect to n_i which makes

$$\epsilon_i = \frac{\partial E}{\partial n_i} = \epsilon_{\mathrm{LDA}} + U\left(\frac{1}{2} - n_i\right). \quad (2.21)$$

It follows from equation (2.21) that depending on the orbital occupation n_i the orbital energy is shifted with respect to the energy that is obtained within the LDA. In particular, occupied orbitals are shifted by -U/2 while unoccupied orbitals are shifted by U/2.

A problem which remains is the identification of the orbital occupancies. Liechtenstein *et al.* proposed to solve this problem by expanding the wave functions around the atoms in a localized orthonormal basis $|ilnm\sigma>$ [22]. Here, i corresponds to the site, n refers to the main quantum number, l to the orbital quantum number, m to the magnetic quantum number, and σ to the spin. As both spin-channels are considered seperately the uncorrelated energy functional now refers to the LSDA. If one restricts to the situation of only one nl shell which is partly filled one can define the density matrix by

$$n^{\sigma}_{mm'} = -\frac{1}{\pi}\int^{E_{\mathrm{F}}} \mathrm{Im}\, G^{\sigma}_{inlm,inlm'}(E)\mathrm{d}E \tag{2.22}$$

with $G^{\sigma}_{inlm,inlm'}(E) =< inlm\sigma|(E-H)^{-1}|inlm'\sigma >$ being the matrix elements of the Green-function within the localized representation whereas the effective single-electron Hamiltonian is denoted as H [22]. The generalized LDA+U functional after Liechtenstein *et al.* is defined as

$$E_{\mathrm{LDA+U}} = E_{\mathrm{LSDA}}[\rho^{\sigma}(\mathbf{r})] + E_{\mathrm{U}}[\{n^{\sigma}\}] - E_{\mathrm{dc}}[\{n^{\sigma}\}] \tag{2.23}$$

where the effects due to orbital polarizations are included by the term

$$\begin{aligned} E_{\mathrm{U}}[\{n\}] = \quad \frac{1}{2}\sum_{m,\sigma}\{&< m,m''|V_{\mathrm{ee}}|m',m''' > n^{\sigma}_{mm'}n^{-\sigma}_{m''m'''} - (< m,m''|V_{\mathrm{ee}}|m',m''' > \\ &- < m,m''|V_{\mathrm{ee}}|m''',m' >)n^{\sigma}_{mm'}n^{\sigma}_{m''m'''}\} \end{aligned} \tag{2.24}$$

and the double counting is corrected by the term

$$E_{\mathrm{dc}}[\{n^{\sigma}\}] = \frac{1}{2}UN(N-1) - \frac{1}{2}J[N^{\uparrow}(N^{\uparrow}-1) + N^{\downarrow}(N^{\downarrow}-1)] \tag{2.25}$$

where the different occupation numbers are defined as $N^{\sigma} = \mathrm{Tr}(n^{\sigma}_{mm'})$ and $N = N^{\uparrow} + N^{\downarrow}$ and V_{ee} corresponds to the screened Coulomb interactions between the nl electrons [22] (see also Ref. [23]). Here, U and J refer to screened Coulomb and exchange parameters [24].

The calculations that will be presented within this thesis have been obtained using the implementation of the LSDA+U method by Dudarev *et al.* [25]. In this implementation the energy is defined as

$$E_{\mathrm{LSDA+U}} = E_{\mathrm{LSDA}} + \frac{U-J}{2}\sum_{\sigma}\left(\sum_{m} n^{\sigma}_{mm} - \sum_{m,m'} n^{\sigma}_{mm'}n^{\sigma}_{m'm}\right). \tag{2.26}$$

In a similar manner as it is done in the LDA+U method, a term which takes into account correlation effects can also be added to GGA exchange-correlation functional which gives rise to the GGA+U method. In fact, the GGA+U method is derived by replacing the energy

functional of the LSDA (E_{LSDA}) with the particular GGA energy functional that is used (E_{GGA}) in the equations that are listed above.

The introduction of the Hubbard term raises however the question about the absolute value of the U. While this value can either be estimated from experimental observations (see for example Ref. [26]) there also exist different computational approaches to estimate the value of the Hubbard term [27, 28, 29, 30].

2.1.9 Pseudopotentials

The application of the previously discussed techniques still faces problems regarding its practicability. In particular, the computational effort that is needed exceeds the available computational power for many known problems. This is due the large number of electrons (and thus, the number of orbitals for which the Kohn-Sham equations have to be solved) in a solid. However, while only a few electrons, in particular the valence electrons, play a role in the binding processes of the solid, the so-called core electrons that belong to the inner shells of the atoms do not take part in the binding processes in general. As the Kohn-Sham orbitals have to be orthogonal to each other, the presence of the core electrons also increases the size of the basis set that is needed for a proper description of the wavefunction.

The pseudopotential method accounts for the problems mentioned above by neglecting the core electrons and instead replacing the Coulumb potential of the core by some artifical potential such that the spectrum of the original Hamilton operator with the Coulomb potential is nearly exactly reproduced by the Hamilton operator with the artificial potential [31]. As a main criterion the wavefunctions that are obtained using the pseudopotential method should mostly agree with wavefunctions that are obtained withouth the use of pseudopotentials in regions with a certain distance to the atomic cores. This distance is the so-called core radius.

In the following the theory of pseudopotentials based on orthogonalized plane waves (OPW) will be introduced [32, 33]. Although this method is not state of the art it already demonstrates how to deal with the problems that are arising from the presence of the core electrons. If one assumes that the wavefunction can be described by plane waves the valence states are described as

$$\chi_{\mathbf{k}}(\mathbf{r}) = e^{i\mathbf{kr}} - \sum_j \langle c_j|\mathbf{k}\rangle c_j(\mathbf{r}) \tag{2.27}$$

where

$$\langle c_j|\mathbf{k}\rangle = \int d\mathbf{r} c_j(\mathbf{r}) e^{i\mathbf{kr}} \tag{2.28}$$

is the projection of the function $c_j(\mathbf{r})$ on the plane wave $e^{i\mathbf{kr}}$. By construction, $\chi_{\mathbf{k}}(\mathbf{r})$ and $c_j(\mathbf{r})$ are orthogonal. If additionally the $c_j(\mathbf{r})$ are localized around the atomic cores and vanish in the interstitial regions between the cores the $\chi_{\mathbf{k}}(\mathbf{r})$ are equivalent to $e^{i\mathbf{kr}}$ in these regions. A proper choice of the $c_j(\mathbf{r})$ function allows to reproduce the scattering properties of atoms using a smaller number of wave vectors $\mathbf{k}$ than the number of wave vectors that is needed

when taking into account all electrons as valence electrons.

Another class of pseudopotentials are the so-called norm-conserving pseudopotentials. Norm-conserving pseudopotentials are generated using the effective potential of all-electron calculations (also referred to as full potential calculations) such that the pseudo wavefunctions which are satisfying the Kohn-Sham equations are normalized. As a consequence there is no connection between the all-electron wavefunctions and the pseudo wavefunctions in the core region. This is in contrast to the orthogonalized plane wave method where the discussed functions $c_j(\mathbf{r})$ which are localized around the core, can be related to actual electronic core states.

A common problem related to norm-conserving pseudopotentials is the fact that the effective potential of an all-electron calculation contains contributions from the Hartree potential and contributions from the exchange-correlation potential. While in principle the Hartree potential can be substracted from the effective potential, this is not possible for the exchange-correlation potential as it cannot be separated into a core and a valence part.

Norm-conserving pseudopotentials still may face problems in specific systems. Such systems are, for example, atoms from the first period of the periodic table of the chemical elements or atoms containing d- or f-electrons where it is not possible to find pseudo wavefunctions that are softer than wavefunctions which have been obtained using all-electron calculations (which means both wavefunctions show approximately the same number of oscillations in the region around the core). Ultrasoft pseudopotentials provide a solution to this problem by abandoning the criterion of norm-conservation. This means that the pseudo wavefunctions are not normalized anymore which leads to softer wavefunctions and reduces the size of the basis set needed for a proper description of the wavefunction.

Ultrasoft pseudopotentials are generated from the electronic density of the system. As the density changes with every iteration, the pseudopotentials also have to be generated iterative during the calculation. Although this seems to introduce additional computational effort needed for the solution of the problem ultrasoft pseudopotential still are able to give reasonable results in acceptable computational time when studying systems where the effort to generate the pseudopotential is small compared to the calculation of the electronic structure itself [34].

Although pseudopotentials allow the calculation of very complex systems their use disables the possibility to get information about the behaviour of the wavefunction near the atomic cores. One approach to overcome this problem is the projector augmented wave (PAW) method [35].

The PAW method is a full-potential calculation which keeps the all-electron wavefunction. However, at the same time it also makes use of pseudopotential methods. In particular, many parts of the main idea behind the OPW method which was previously introduced are also used in the PAW method. The pseudo wavefunction and the all-electron wavefunction disagree in the so-called augmentation regions that are centered around the atomic core but are equal outside these regions. It is assumed that the all-electron wavefunction can be generated from the pseudo wavefunction using a linear transformation. In this case the expectation values of

operators that are applied to the all-electron wavefunction agree with the expectation values that are obtained when applying this linear transformation on the operators and applying the result on the pseudo wavefunction.

2.1.10 Density functional theory codes

Several software packages which make use of the previously discussed methods and techniques are available. In addition to programs which are published under public licences like the PWSCF code [36] commercial codes are also available. Unless noted otherwise all results presented in this thesis have been obtained using the Vienna Ab Initio Simulation Package (VASP) [37, 38] using PAW pseudopotentials [35] and the generalized gradient approximation in the forumulation of Perdew, Burke, and Ernzerhof as the exchange-correlation functional [14].

2.2 Lattice dynamics

Lattice vibrations play an important role in the description of finite temperature effects in the solid state. Therefore the fundamental aspects related to the dynamics of atoms in a crystal and the physical properties that can be derived by an analysis of the dynamical properties will be introduced in the following. The description is based on the introductions to this topic by J. R. Christman, H. Ibach, K.-H. Hellwege, and H. Lüth [39, 40, 41].

2.2.1 The harmonic approximation

The periodically arranged atoms in a crystal are exposed to a potential U that is generated by their surrounding neighbours. Assuming that the system is in the ground state, all atoms are sitting on their ideal lattice positions and no forces act upon the atoms in equilibrium. It is clear that a displacement of any atom away from its equilibrium position introduces forces that act on the displaced atom or any other atom in the lattice. In the harmonic approximation the displacements are assumed to be small so that the forces that appear depend linearly on the displacement size. This means that the component α of the force that acts on atom i can be written as

$$F_i^\alpha = -\sum_\beta \sum_j \Phi^{\alpha\beta}(i,j) u_j^\beta \tag{2.29}$$

where the first sum is a sum over all components β (in three dimensions these components are x, y, and z), the second sum is a sum over all atoms j, and u_j^β denotes the component β of the displacement of atom j. $\Phi^{\alpha\beta}(i,j)$ is the so-called force constant that relates the displacements and forces in exactly the same way as the spring constant in Hooke's law that is known from classical mechanics. Making use of Newton's second law results in

$$M_i \frac{d^2 u_i^\alpha}{dt^2} = -\sum_\beta \sum_j \Phi^{\alpha\beta}(i,j) u_j^\beta \tag{2.30}$$

where m_i is the mass of atom i. The displacements u_j^β are assumed to be plane waves

$$u_i^\alpha = \frac{1}{\sqrt{M_i}} A_i^\alpha e^{i(\mathbf{q}\cdot\mathbf{r}_i - \omega t)} \tag{2.31}$$

with the wave vector $\mathbf{q}$. If one inserts this approach for the displacements in equation (2.30) one obtains

$$-\omega^2 M_i u_i^\alpha = -\sum_\beta \sum_j \Phi^{\alpha\beta}(i,j) u_j^\beta \tag{2.32}$$

which leads to

$$0 = \sum_\beta \sum_j \Phi^{\alpha\beta}(i,j) u_j^\beta - \omega^2 M_i u_i^\alpha \tag{2.33}$$

Multiplying this equation with $\frac{1}{\sqrt{M_i}} e^{-i(\mathbf{q}\mathbf{r}_i - \omega t)}$ gives

$$\left[\sum_\beta \sum_j \Phi^{\alpha\beta}(i,j) u_j^\beta - \omega^2 M_i u_i^\alpha \right] \frac{1}{\sqrt{M_i}} e^{-i(\mathbf{q}\mathbf{r}_i - \omega t)} = 0 \tag{2.34}$$

Replacing u_j^β and u_i^α by the definition given in (2.31) results in

$$\sum_\beta \sum_j \Phi^{\alpha\beta}(i,j) \frac{1}{\sqrt{M_i M_j}} A_j^\beta e^{i\mathbf{q}(\mathbf{r}_j - \mathbf{r}_i)} - \omega^2 A_i^\alpha = 0 \tag{2.35}$$

In the next step the sum over all atoms j is split into a sum over all unit cells n and a sum over the different atoms v of the basis. As the plane waves considered in equation (2.31) are assumed to travel through the whole crystal, it is clear that the amplitudes of atoms of the same type in different unit cells will be the same. Therefore, A_j^β can be replaced by A_v^β when splitting up the summation over all atoms j as described above. Becasue of the translational invariance of the crystal the atom i may be considered to be in the 0-th unit cell and therefore can be replaced by w being one atom of the basis. The force constant therefore just depends on v and w:

$$\Phi^{\alpha\beta}(i,j) = \Phi^{\alpha\beta}_{w0,vn} \tag{2.36}$$

where the index $w0$ denotes the atom of type w in the 0-th unit cell and in analogy vn denotes the atom of type v in the n-th unit cell. This makes

$$\sum_\beta \sum_v \sum_n \frac{1}{\sqrt{M_v M_w}} \Phi^{\alpha\beta}_{w0,vn} e^{i\mathbf{q}\cdot(\mathbf{r}_{vn} - \mathbf{r}_{w0})} A_v^\beta - \omega^2 A_w^\alpha = 0 \tag{2.37}$$

If one defines the so-called dynamical matrix element $D_{wv}^{\alpha\beta}(\mathbf{q})$ as

$$D_{wv}^{\alpha\beta}(\mathbf{q}) = \sum_n \frac{1}{\sqrt{M_v M_w}} \Phi^{\alpha\beta}_{w0,vn} e^{i\mathbf{q}\cdot(\mathbf{r}_{vn} - \mathbf{r}_{w0})} \tag{2.38}$$

it finally follows

$$\sum_{\beta}\sum_{v} D_{wv}^{\alpha\beta}(\mathbf{q})A_v^{\beta} - \omega^2 A_w^{\alpha} = 0 \tag{2.39}$$

which is a homogeneous linear algebra problem that has non-vanishing solutions in the case of

$$\mathrm{Det}\left[D_{wv}^{\alpha\beta}(\mathbf{q}) - \omega^2\delta_{\alpha\beta}\delta_{wv}\right] = 0 \tag{2.40}$$

These solutions allow to obtain the dispersion $\omega(\mathbf{q})$ which relates the frequencies of the lattice vibration modes to their wave vectors. As the lattice vibrations are also called phonons, $\omega(\mathbf{q})$ is also called phonon dispersion relation. In the case of 3 dimensions and a basis consisting of N different atoms the dynamical matrix is a $3N \times 3N$ matrix and equation (2.40) has exactly $3N$ solutions.

Calculation of phonon dispersion curves

As the force $\mathbf{F}_i$ that acts on atom i is defined as the negative gradient of the potential U, equation (2.29) can also be written as

$$\Phi_{\alpha\beta}(i,j) = \frac{\partial^2 U}{\partial u_i^{\alpha}\partial u_j^{\beta}} \tag{2.41}$$

Equation (2.41) basically contains all necessary information that is needed to compute the force constants of a system in practice (which then give rise to the phonon dispersion according to equation (2.40)). In particular the second derivative of the potential with respect to small atomic displacements from their equilibrium positions has to be calculated. Making use of the Hellmann-Feynman theorem [42, 43], state of the art density functional theory codes allow to calculate the forces, which are acting on individual atoms, which may then be inserted into additional tools to calculate the force constants and phonon dispersion curves [44, 45]. As an example Fig. 2.1 contains the phonon dispersion of the Mn_3Fe alloy.

Determination of thermodynamic properties

As it has been pointed out in the previous paragraphs the lattice vibrations in a periodic crystal can be described using a plane wave approach which decouples the atomic equations of motion into a linear algebra problem that has $3N$ solutions in the case of 3 dimensions and an atomic basis consisting of N atoms. As the waves are not interacting the energies of each solution can be considered as the energies of a quantum mechanical oscillator

$$E_n = \hbar\omega(\tfrac{1}{2} + n) \tag{2.42}$$

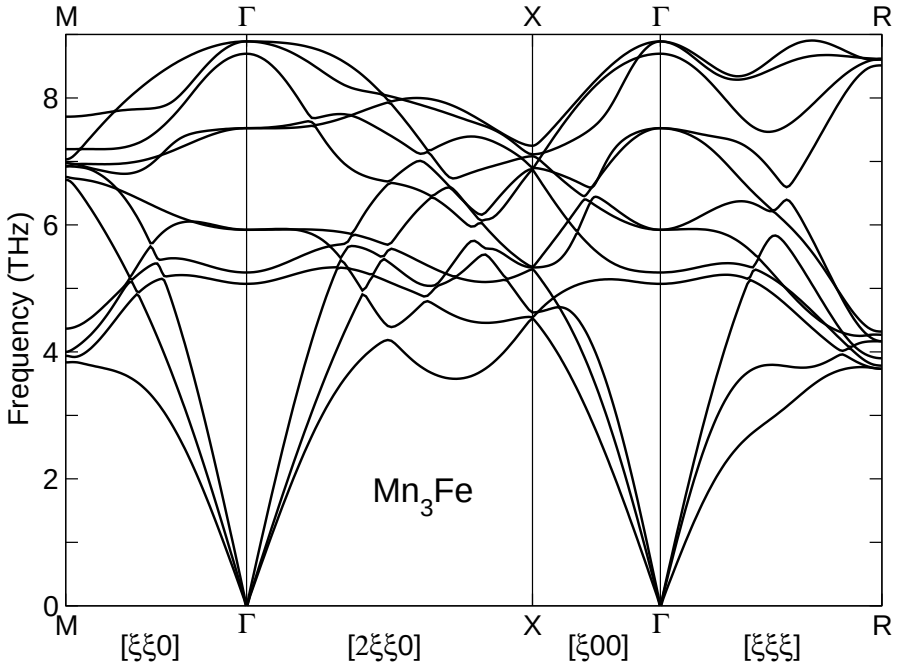

Figure 2.1: Phonon dispersion of Mn_3Fe calculated in a $3 \times 3 \times 3$ supercell using VASP and the PHON code [44]. Figure adapted from Ref. [46]

At finite temperature T the partition function $Z(\omega, T)$ can therefore be written as

$$\begin{aligned} Z(\omega,T) &= \sum_{n=0}^{\infty} e^{-\frac{E_n}{k_\mathrm{B}T}} = \sum_{n=0}^{\infty} e^{-(\frac{1}{2}+n)\frac{\hbar\omega}{k_\mathrm{B}T}} = e^{-\frac{\hbar\omega}{2k_\mathrm{B}T}} \sum_{n=0}^{\infty} e^{-n\frac{\hbar\omega}{k_\mathrm{B}T}} \\ &= e^{-\frac{\hbar\omega}{2k_\mathrm{B}T}} \frac{1}{1-e^{-\frac{\hbar\omega}{k_\mathrm{B}T}}} = \frac{e^{-\frac{\hbar\omega}{2k_\mathrm{B}T}}}{1-e^{-\frac{\hbar\omega}{k_\mathrm{B}T}}} \end{aligned}$$

If the partition function is known, the energy $\epsilon(\omega, T)$ for a given frequency ω can be calculated

$$\begin{aligned} \epsilon(\omega,T) &= \frac{1}{Z}\sum_{n=0}^{\infty} E_n e^{-\frac{En}{k_\mathrm{B}T}} = \frac{1}{Z}\left(\sum_{n=0}^{\infty} \tfrac{1}{2}\hbar\omega e^{-\frac{En}{k_\mathrm{B}T}} + \sum_{n=0}^{\infty} n\hbar\omega e^{-\frac{En}{k_\mathrm{B}T}}\right) \\ &= \tfrac{1}{2}\hbar\omega + \hbar\omega\frac{1}{Z}e^{-\frac{\hbar\omega}{2k_\mathrm{B}T}} \sum_{n=0}^{\infty} n e^{-n\frac{\hbar\omega}{k_\mathrm{B}T}} = \tfrac{1}{2}\hbar\omega + \hbar\omega\frac{1}{Z}e^{-\frac{\hbar\omega}{2k_\mathrm{B}T}} \frac{e^{-\frac{\hbar\omega}{k_\mathrm{B}T}}}{(e^{-\frac{\hbar\omega}{k_\mathrm{B}T}}-1)^2} \\ &= \tfrac{1}{2}\hbar\omega + \hbar\omega e^{-\frac{\hbar\omega}{k_\mathrm{B}T}} \frac{1-e^{-\frac{\hbar\omega}{k_\mathrm{B}T}}}{(e^{-\frac{\hbar\omega}{k_\mathrm{B}T}}-1)^2} = \hbar\omega\left(\frac{1}{2} - e^{-\frac{\hbar\omega}{k_\mathrm{B}T}}\frac{1}{e^{-\frac{\hbar\omega}{k_\mathrm{B}T}}-1}\right) \\ &= \hbar\omega\left(\frac{1}{2} - e^{-\frac{\hbar\omega}{k_\mathrm{B}T}}\frac{e^{\frac{\hbar\omega}{k_\mathrm{B}T}}}{1-e^{\frac{\hbar\omega}{k_\mathrm{B}T}}}\right) = \hbar\omega\left(\frac{1}{2} + \frac{1}{e^{\frac{\hbar\omega}{k_\mathrm{B}T}}-1}\right) \end{aligned}$$

The total energy E of the crystal is derived by adding up the energies of all different frequencies multiplied with the number of states that exist in the frequency interval $d\omega$ around the

respective frequency. If one defines $g(\omega)$ as the phonon density of states (often also referred to as the vibrational density of states), the sum can be replaced by the integral

$$E(T) = \int_0^\infty \epsilon(\omega, T) g(\omega) d\omega = \int_0^\infty g(\omega) d\omega \hbar\omega \left(\frac{1}{2} + \frac{1}{e^{\frac{\hbar\omega}{k_\mathrm{B}T}} - 1} \right) \tag{2.43}$$

If the phonon dispersion curve is known, this term can easily be evaluated for different temperature values. Beneath the total energy E, the free energy F is also an important quantity when studying the phase stability of different type of crystal structures. The free energy is defined as

$$f(\omega, T) = -k_\mathrm{B}T \log(Z) \tag{2.44}$$

Inserting the expression for Z that has been derived above into this equation yields

$$\begin{aligned} f(\omega, T) &= -k_\mathrm{B}T \log \left(\frac{e^{-\frac{\hbar\omega}{2k_\mathrm{B}T}}}{1 - e^{-\frac{\hbar\omega}{k_\mathrm{B}T}}} \right) \\ &= -k_\mathrm{B}T \log \left(e^{-\frac{\hbar\omega}{2k_\mathrm{B}T}} \right) + k_\mathrm{B}T \log \left(1 - e^{-\frac{\hbar\omega}{k_\mathrm{B}T}} \right) \\ &= \frac{\hbar\omega}{2} + k_\mathrm{B}T \log \left(1 - e^{-\frac{\hbar\omega}{k_\mathrm{B}T}} \right) \end{aligned}$$

using this expression the total free energy of the crystal F can be derived in a similar manner as in the case of the total energy E

$$F(T) = \int_0^\infty f(\omega, T) g(\omega) d\omega = \int_0^\infty g(\omega) d\omega \left(\frac{\hbar\omega}{2} + k_\mathrm{B}T \log \left(1 - e^{-\frac{\hbar\omega}{k_\mathrm{B}T}} \right) \right) \tag{2.45}$$

2.2.2 Anharmonic effects

As it was already stated the harmonic approximation that is used here is an approximation for small displacements of the atoms from their ideal lattice positions. If the displacements become larger (for example at elevated temperatures) the harmonic approximation fails as in this case also anharmonic terms become important. This means that the forces do not just depend linearly on the displacement sizes anymore but also on higher order terms of the displacements sizes like quadratic terms.

2.3 Spin Dynamics

In a magnetic system, not only lattice vibrations, but also fluctuations of the alignments of the magnetic spins of the atoms may be important. While displaced atoms interact with the potential U the different spins of a magnetic system interact directly with each other via so-called magnetic exchange constants that can be viewed as an analogon of the force constant matrices. The short introduction to spin dynamics that is presented in the following

is an extension to three dimensions and multiple types of atoms of the solution for a one-dimensional spin-chain that can be found in many textbooks, see for example Ref. [47]. A more detailed derivation of spin wave properties in ferromagnets and antiferromagnets is given by Anderson [48].

In the Heisenberg model the Hamiltonian of interacting atoms is defined as

$$\mathcal{H} = -\frac{1}{2}\sum_{i,j} J_{ij}\mathbf{S}_i \cdot \mathbf{S}_j \tag{2.46}$$

where the spin $\mathbf{S}_i$ of atom i is defined as

$$\mathbf{S}_i = \begin{pmatrix} S_i^x \\ S_i^y \\ S_i^z \end{pmatrix}$$

and J_{ij} is the magnetic exchange constant between the atom i and the atom j. If one considers the system to be in the ferromagnetic case so that the magnetic moments are aligned along the z-direction ($S_i^x \ll S_i^z, S_i^y \ll S_i^z, S_i^z \approx \mu_i$) one may write

$$\mathbf{S}_i = \begin{pmatrix} S_i^x \\ S_i^y \\ \mu_i \end{pmatrix}$$

where μ_i is the magnetic moment of atom i. Each atom i is exposed to a magnetic field $\mathbf{H}_i$ which is generated by the surrounding atoms

$$\mathbf{H}_i = \begin{pmatrix} H_i^x \\ H_i^y \\ H_i^z \end{pmatrix} = \begin{pmatrix} \sum_j J_{ij}S_j^x \\ \sum_j J_{ij}S_j^y \\ \sum_j J_{ij}S_j^z \end{pmatrix} = \begin{pmatrix} \sum_j J_{ij}S_j^x \\ \sum_j J_{ij}S_j^y \\ \sum_j J_{ij}\mu_j \end{pmatrix} \tag{2.47}$$

Once the magnetic field is known the Landau-Lifshitz-Gilbert equation can be used to retrieve an expression for the derivative of the spin with respect to the time t (the damping term is neglected here) [49, 50].

$$\frac{1}{\gamma}\frac{d\mathbf{S}_i}{dt} = \mathbf{H}_i \times \mathbf{S}_i = \begin{pmatrix} \mu_i \sum_j J_{ij}S_j^y - S_i^y \sum_j J_{ij}\mu_j \\ S_i^x \sum_j J_{ij}\mu_j - \mu_i \sum_j J_{ij}S_j^x \\ S_i^y \sum_j J_{ij}S_j^x - S_i^x \sum_j J_{ij}S_j^y \end{pmatrix} \tag{2.48}$$

Here, γ is the gyromagnetic ratio. In the next step all products containing x- and y-components of the spin may be neglected ($S_i^x S_j^y \approx 0$, $S_i^y S_j^x \approx 0$) as S_i^x and S_i^y are assumed to be significantly smaller than μ_i

$$\frac{1}{\gamma}\frac{d\mathbf{S}_i}{dt} = \mathbf{H}_i \times \mathbf{S}_i = \begin{pmatrix} \mu_i \sum_j J_{ij}S_j^y - S_i^y \sum_j J_{ij}\mu_j \\ S_i^x \sum_j J_{ij}\mu_j - \mu_i \sum_j J_{ij}S_j^x \\ 0 \end{pmatrix} \tag{2.49}$$

The vector equation (2.49) yields two scalar equations which can be written as one complex equation. If one assumes plane waves as solutions for S_i^x and S_i^y one may write

$$S_i^x = u_i\, e^{i(\mathbf{q}\cdot\mathbf{r}_i - \omega t)}$$
$$S_i^y = v_i\, e^{i(\mathbf{q}\cdot\mathbf{r}_i - \omega t)}$$

which, in a complex notation yields

$$\sigma_i = S_i^x + i\, S_i^y = c_i\, e^{i(\mathbf{q}\cdot\mathbf{r}_i - \omega t)} \tag{2.50}$$

where $c_i = u_i + i\, v_i$ is the complex amplitude. Using the definition of σ_i, equation (2.49) can be written as

$$\frac{1}{\gamma}\frac{d\sigma_i}{dt} = \left(\mu_i \sum_j J_{ij} S_j^y - S_i^y \sum_j J_{ij}\mu_j\right) + i\left(S_i^x \sum_j J_{ij}\mu_j - \mu_i \sum_j J_{ij} S_j^x\right) \tag{2.51}$$

which results in

$$\begin{aligned}\frac{1}{\gamma} i\omega c_i\, e^{i(\mathbf{q}\cdot\mathbf{r}_i - \omega t)} &= \left(\mu_i \sum_j J_{ij} v_j\, e^{i(\mathbf{q}\cdot\mathbf{r}_j - \omega t)} - v_i\, e^{i(\mathbf{q}\cdot\mathbf{r}_i - \omega t)} \sum_j J_{ij}\mu_j\right) \\ &\quad + i\left(u_i\, e^{i(\mathbf{q}\cdot\mathbf{r}_i - \omega t)} \sum_j J_{ij}\mu_j - \mu_i \sum_j J_{ij} u_j\, e^{i(\mathbf{q}\cdot\mathbf{r}_j - \omega t)}\right)\end{aligned}$$

when inserting the plane wave approach. Dividing both sides of this equation by $i\, e^{i(\mathbf{q}\cdot\mathbf{r}_i - \omega t)}$ yields

$$\begin{aligned}\frac{1}{\gamma}\omega c_i &= \left(u_i \sum_j J_{ij}\mu_j - \mu_i \sum_j J_{ij} u_j\, e^{i\mathbf{q}\cdot(\mathbf{r}_j - \mathbf{r}_i)}\right) \\ &\quad - i\left(\mu_i \sum_j J_{ij} v_j\, e^{i\mathbf{q}\cdot(\mathbf{r}_j - \mathbf{r}_i)} - v_i \sum_j J_{ij}\mu_j\right) \\ &= c_i \sum_j J_{ij}\mu_j - \mu_i \sum_j J_{ij} c_j\, e^{i\mathbf{q}(\mathbf{r}_j - \mathbf{r}_i)}\end{aligned}$$

In the next step the periodicity of the crystal and the translational invariance are used in a very similar way as described in the section about lattice dynamics. In particular, the sum over all atoms j is replaced by a sum over all unit cells n and a sum over all basis atoms v. At the same time the atom i, which is any atom of the crystal is chosen to be contained in the 0-th unit cell and therefore is replaced by w which denotes one atom of the basis.

$$\frac{1}{\gamma}\omega c_w = c_w \sum_v \sum_n J_{w0}^{vn}\mu_v - \mu_w \sum_v \sum_n J_{w0}^{vn} c_v\, e^{i\mathbf{q}(\mathbf{r}_{vn} - \mathbf{r}_{w0})} \tag{2.52}$$

If one defines

$$H_w = \sum_v \sum_n J_{w0}^{vn} \mu_v \tag{2.53}$$

and, in analogy to the dynamical matrix in the case of the phonons,

$$D_{wv}(\mathbf{q}) = \sum_n J_{w0}^{vn} \, e^{i\mathbf{q}(\mathbf{r}_{vn} - \mathbf{r}_{w0})} \tag{2.54}$$

one obtains the homogeneous linear algebra problem

$$\frac{\omega}{\gamma} c_w = H_w c_w - \sum_v \mu_w D_{wv}(\mathbf{q}) c_v \tag{2.55}$$

which has non-vanishing solutions in the case of

$$\mathrm{Det}\left[\mu_w D_{wv}(\mathbf{q}) - \left(H_w - \frac{\omega}{\gamma}\right)\delta_{wv}\right] = 0 \tag{2.56}$$

Equation (2.56) allows to derive the magnon dispersion $\omega(\mathbf{q})$ of spin waves, that are traveling through the crystal. In analogy to the phonons, these spin waves are called magnons. The magnon dispersion of a crystal with N basis atoms consists of N branches.

Chapter 3

Experimental background

3.1 The shape memory effect

The shape memory effect (SME) is named after the characteristic property of certain materials which are able to recover their original shape after a plastic deformation. Alloys exhibiting the SME are called shape memory alloys (SMA).

The SME originates from microscopic changes of the crystal structures in the material. These changes are related to a so-called martensitic transformation which is a necessary condition for the SME. A martensitic transformation is a displacive, difussionless first-order phase transformation [51]. The transformation is often governed by a shear-like transformation of the crystal structure and is characterized by a cooperative movement of atoms [52]. The cooperative movement of atoms results in macroscopic shape changes caused by the transformation although the displacements of the individual atoms of the crystal are small compared to the inter-atomic distances.

In certain cases a martensitic transformation is accompanied by a dynamical instability of the parent phase that appears when approaching the transition temperature. In other words, the restoring forces that act on the atoms of the crystal as they are displaced from their ideal lattice sites start to vanish. The phonon mode that corresponds to the atomic displacements where the instability appears is called "soft mode". The name originates from the fact that phonon frequency of a soft mode is decreasing as the transition temperature is approached (see Fig. 3.1) while for materials showing no softening the frequencies should increase with decreasing temperature. The decrease of the frequencies is directly related to the amount of energy that is connected with the displacement. The system becomes thermodynamical unstable, if it gains energy by transforming into another phase. As *ab initio* calculations of phonons are usually carried out at $T = 0\,\mathrm{K}$, the resulting frequencies of a structure that is unstable at low temperatures can even become imaginary. The origin of the softening of phonon modes is related to the electronic structure. In particular, for certain shapes of the Fermi surface the derivative $|grad_{\mathbf{q}}\,\omega(\mathbf{q})|$ diverges [53]. This behaviour is known as the Kohn anomaly and is also related to the phonon anomalies that appear in materials which undergo a martensitic transformation [54].

As a martensitic transformation is of first-order type, different characteristic temperatures which are relevant for the transformation are obtained depending on weather the system is heated or cooled. If the system is cooled from the high temperature phase (called austenite), it

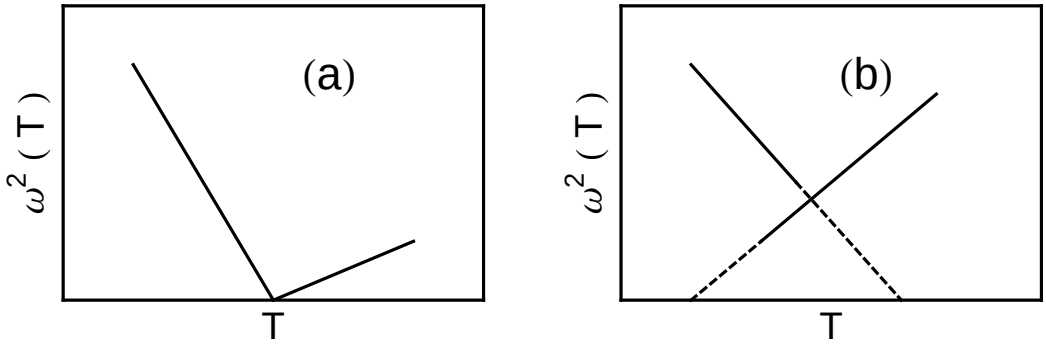

Figure 3.1: Schematic plot of the soft-mode behaviour after Delaey [51]. The squared phonon frequencies w^2 are plotted as a function of temperature T for (a) a second order and (b) a first order transformation.

starts to transform to the low temperature phase (called martensite) at the so-called martensitic start temperature M_S. The transformation to the martensite structure is completed at the martensitic finish temperature M_F. When heating up the sample, the transformation from the martensite to the austenite structure starts at the so-called austenitic start temperature A_S and finishes at the austenitic finish temperature A_F [55], see also Fig. 3.2

In the example which is plotted in Fig. 3.2 the austenite phase is a cubic phase while the martensite phase has a lower symmetry. The shear plane of a martensitic transformation is called habit plane and separates the martensite from the austenite structure. The lowered symmetry of the martensite introduces different orientations of the crystal structure in the martensite phase with respect to the austenite phase which are called variants. As the macroscopic shape of the system does not change under a martensitic transformation, the different types of variants are aligned in an order that satisfies this condition when the transition takes place. The resulting alignment is called twinned martensite, whereas the boundaries between regions of differently orientated variants are called twin boundaries. By applying mechanical load to a shape memory material the twinned martensite may be transformed into the detwinned martensite. In this structure only one type of martensitic variant (the one that is energetically favoured when applying the mechanical load) is present. Fig. 3.2 contains a schematic illustration of the martensitic transformation, the different types of variants and the detwinning under mechanical load in a shape memory material.

Due to the existence of different variants many structural configurations (which differ in the particular arrangement of the variants) of a system exist in the martensite structure which all transform into the same austenite structure upon heating. This relationship is crucial for the shape memory effect: Transformations that are applied on the martensite structure by the movement of twin boundaries caused by mechanical load do not effect the shape of the austenite that is restored when heating up the system. This type of shape memory behaviour is sometimes also called one-way shape memory effect. The so-called two-way shape memory

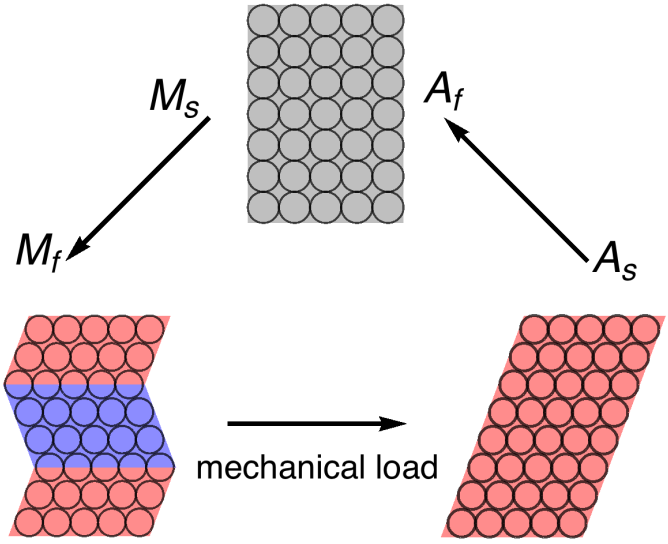

Figure 3.2: Schematic illustration of the martensitic transformation in a shape memory material. When cooling below M_S the austenite (upper middle) starts to transform to the twinned martensite structure (lower left). At $T = M_F$ the transformation is completed. The twinned martensite can be transformed to the detwinned martensite (lower right) by applying mechanical load. When cooling above A_S the sample starts to transform back to the austenite structure. The transformation is finished at $T = A_F$.

effect describes the phenomenon that after several cycles of heating and cooling the system also remembers the shape of the martensite structure. The two-way SME appears due to dislocations in the martensite that are also present in the austenite phase and stabilize a specific configuration of martensitic variants [56].

Beside from the shape memory effect, also another phenomenon called superelasticity (sometimes also referred to as pseudoelasticity or hyperelasticity) is observed in materials showing a martensitic transformation. The appearance of superelastic behaviour is related to the fact that martensitic transformations can be induced even above M_S by the application of external stress [57]. If the stress-induced transformation takes place above A_F the sample immediately transforms back to the original austenite structure when the stress is removed which results in a rubber-like elastic behaviour. Superelasticity as well as the magnetic shape memory effect require highly mobile twin boundaries that allow for easy deformation within the martensite phase [56].

3.1.1 The magnetic shape memory effect

The magnetic shape memory effect appears in ferromagnetic materials that show shape memory behaviour. Ferromagnetic shape memory alloys (FSMAs) are shape memory materials which are ferromagnetic which means that they undergo a ferromagnetic phase transition. While the origin of the shape memory effect (the martensitic phase transformation) is the same in FSMAs as in conventional SMAs, the apperance of magnetic domains bears additional functional properties. In particular, the transformation temperature is shifted in some materials when applying an external magnetic field. This makes it possible to drive the phase transformation at a constant temperature [58].

However, an external magnetic field can also be used in a different way to interact with an FSMA. In general, the application of a magnetic field leads to a reorientation of the magnetic domains in a ferromagnetic material such that the easy axis and the magnetic field are parallel. The deformation that is associated with this process is known as magnetostriction and is not related to the process which appears in FSMAs that is discussed in the following.

In a martensitic material, the magnetic energy of a martensitic variant under the application of a magnetic field depends on the orientation of the variant. The energy difference between different crystallographic orientations is called magnetocrystalline anisotropy energy (MAE). If the MAE of the martensite structure is large enough, the application of a magnetic field leads to a rearrangement of twin boundaries in the martensite phase instead of reorientating the magnetic domains like it is known from ordinary magnetostriction [59, 60]. This means that one specific orientation of the variant (at which the easy axis is aligned parallel to the magnetic field) is favoured over all other orientations and variants with this specific orientation will grow at the expense of other variants if the energy that is associated with the movement of twin boundaries is smaller than the MAE. If this is the case, large shape changes associated with the reorientation of martensitic variants can be observed under the application of a magnetic field.

The concept of rearrangement of martensitic variants by the movement of twin boundaries using an external magnetic field is schematically plotted in Fig. 3.3. If the sample is in the twinned martensite state without a magnetic field ($H = 0$), the favoured variant grows by moving the twin boundaries when the magnetic field is turned on. At some critical value H_C the sample is saturated and only one variant (the one that is energetically favoured) is left so that the sample is found to have a detwinned martensite structure.

The possibility to achieve a macroscopic strain (which is related to the rearrangement of martensitic variants) using an external magnetic field draws attention to the magnetic shape memory effect from an industrial point of view. Applications that are considered in this context are, for example, actuation and sensor devices [62].

An FSMA has to fulfill certain conditions in order to be used for industrial applications. For example, a high magnetocrystalline anisotropy energy and a high twin boundary mobility are

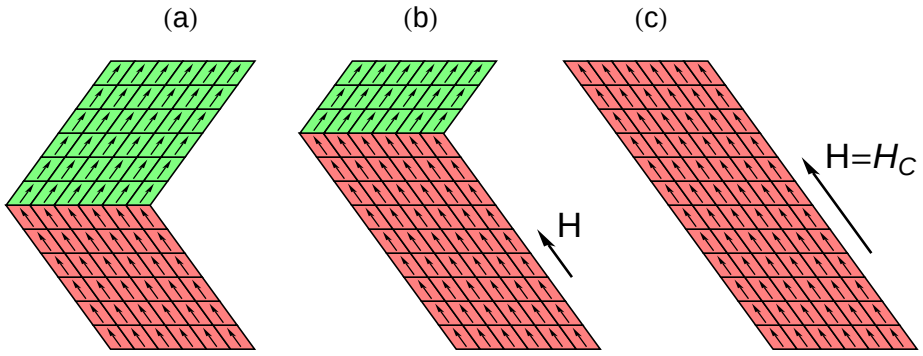

Figure 3.3: Twin boundary movement in an external magnetic field after Ullakko *et al.* [61]. If the sample is in the twinned martensite state withouth any field (a), the energetically favoured variant starts to grow when applying a magnetic field H (b). At some critical value H_C the sample is in the detwinned state where only the variant with the preferred orientation is left.

needed. The twin boundary mobility is determined by several characteristics like composition, sample preparation or training [63]. On the other hand, the transformation temperatures (for the structural, as well as for the magnetic phase transition) also have to be high enough in order to operate devices at room temperature or even above (which is necessary, for example, in devices that are used in the automotive industry). The industrial potential in combination with the widespread requirements that have to be fullfilled by a magnetic shape memory material have lead to an intensive search for possible FSMAs in the past. Compounds that have been studied are Heusler compounds like Ni_2MnGa [64, 65], Fe-based compounds, like the binary alloys Fe-Pt or Fe-Pd [66, 67], Co-Ni-(Al, Ga) [68, 69, 70, 71], Cu-Mn-Ga [72], and quaternary alloys like Ni-Mn-In-Co [73] or Fe-Ni-Co-Ti [74], to mention a few. From these, the ternary alloy Ni_2MnGa, which will be introduced in section 3.2, is one of the most studied compounds. Very recently, a ferrous alloy consisting of 6 constituents, namely Fe-Ni-Co-Al-Ta-B, has been shown to reveal outstanding superelastic properties [75]. This shows that the class of materials which may be used as conventional and magnetic shape memory alloys can still be expanded by extensive investigations [76].

In order to model magnetic shape memory materials and their physical properties it is crucial to make use of a description that properly takes into account the magnetic interaction. So far the description of magnetic systems using model potentials, for example, within molecular dynamics (MD), is very difficult and limited to particular cases. Therefore, the use of *ab initio* techniques like density functional theory is necessary in order to model magnetic shape memory systems on the atomistic scale [77]. In combination with the industrial potential of the magnetic shape memory effect this demand for accurate theoretical calculations in this field encourages the motivation behind the present work.

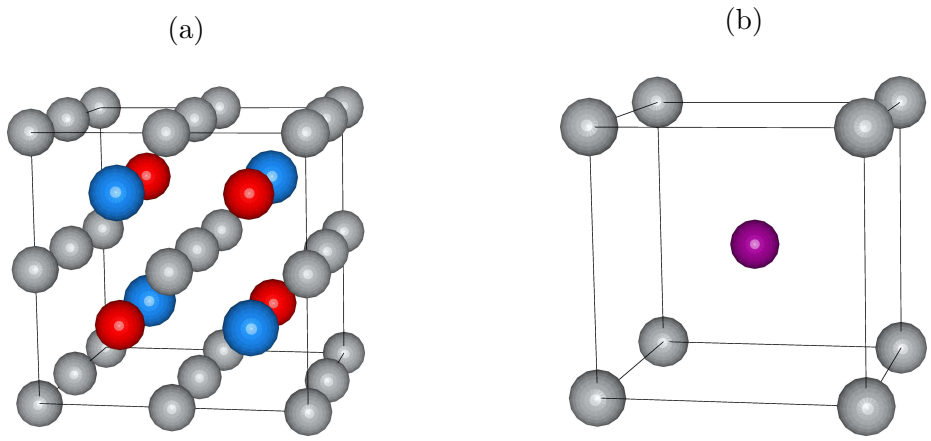

Figure 3.4: Schematic represenation of (a) the $L2_1$-structure and (b) the B2-structure of Ni_2MnGa. The Ni atoms are marked grey in both cases. In the $L2_1$-structure the Mn atoms are coloured red while the Ga atoms are coloured blue. In the B2-structure the two atom types are distributed randomly on a sublattice which is denoted by the violet sphere.

3.2 Ni_2MnGa

A reference material for the magnetic shape memory effect is the ternary alloy Ni_2MnGa. At about room temperature this material is found in the cubic $L2_1$-structure with a lattice parameter of $a = 5.825\,\text{Å}$ [78]. A schematic plot of the $L2_1$-structure of Ni_2MnGa is shown in Fig. 3.4 (a). This structure is also known as the Heusler structure and is named after Friedrich Heusler who reported on it as early as 1903 [79]. It consists of two simple cubic sublattices which are shifted against each other so that the atomic sites of one sublattice are in the center of the cubes that are built up from the atomic sites of the other sublattice. One simple cubic sublattice is occupied by the nickel atoms while the other sublattice is occupied by the manganese and gallium atoms. The ordering in this sublattice is equivalent to the ordering in NaCl and is called B1-structure. The $L2_1$-structure can also be interpreted as four interpenetrating fcc-lattices. In this description two of these lattices are occupied by Ni atoms while the Mn atoms and the Ga atoms each occupy a separate fcc-lattice. The $L2_1$-structure is a bcc-type structure as every atom has 8 nearest neighbours. It should be pointed out that the nickel atoms are not nearest but next-nearest neighbours and the manganese atoms are third nearest neighbours to each other.

When heated Ni_2MnGa undergoes a phase transition from the ordered $L2_1$-structure to the partially disordered B2-structure at 1071 K before it melts at 1382 K [80]. The B2-structure is known from CsCl. While in the latter case the two simple cubic (sc) sublattices that form the bcc-structure are each occupied by just one atomic species, one of these sublattices is occupied by two different atomic species in a disordered manner in case of partially ordered Heusler

compounds. In the case of Ni_2MnGa this means that the sc-sublattice that is occupied in a regular order by Mn and Ga in the $L2_1$-structure is occupied randomly by Mn and Ga in the B2-structure while the other sc-sublattice is occupied completely by the nickel atoms. The difference between the $L2_1$- and the B2-structure is also depicted in Fig. 3.4.

In 1984 Webster *et al.* discovered that stoichiometric Ni_2MnGa undergoes a martensitic phase transformation from the cubic $L2_1$-structure (associated with the parent austenite phase) to a martensitic phase when cooling below 202 K [78]. The martensite phase is found to be a tetragonal structure with a c/a ratio of 0.94 which in addition to the tetragonality also shows signs of a periodic superstructure. Besides the martensitic transformation a premartensitic transformation is also observed at 260 K in Ni_2MnGa. The premartensitic phase as well as the periodic superstructures in the martensitic phase have been related to so-called modulated structures [81]. In these types of structures the atoms are displaced wavelike along the [110] direction. Several wavelengths belonging to different types of structures like the 5M- or 7M-structure have been observed [82, 83]. The specific name refers to the number of primitive cells that are needed to construct the modulated structure, i.e. the wavelength. In addition to the premartensitic phase and the modulated martensitic structures also a nonmodulated tetragonal structure which evolves at low temperatures is found in experiments and confirmed by *ab initio* calculations as being the ground state of Ni_2MnGa [84, 85, 86]. However, the ground state as well as the sequence of phase transformations that appear upon cooling strongly depend on the composition of the crystal [87].

Stoichiometric Ni_2MnGa is ferromagnetic with a ground state magnetization per formula unit (f.u.) of $M = 4.07\,\mu_B$/f.u. at $T = 0$ K which is mainly built up by the magnetic moment of the manganese atom ($3.38\,\mu_B$) which is around one order of magnitude larger than the magnetic moments of the nickel atoms ($0.35\,\mu_B$ each) [3]. The magnetic transition takes place at $T_C \approx 380$ K [88]. The fact that the magnetic transition temperature is larger than the structural transition temperature gives rise to the appearance of a ferromagnetic martensite phase.

In 1996 macroscopic strains of nearly 0.2% that appeared due to the motion of twin boundaries in a magnetic field of 8 kOe were observed in Ni_2MnGa by Ullakko *et al.* [89]. In 2002 Sozinov *et al.* reported on a "giant magnetic-field-induced strain" in off-stoichiometric Ni-Mn-Ga [65]. The strain of 9.5% in a magnetic field that was smaller than 1 T was obtained in a seven-layered martensite phase (7M-structure) at the composition $Ni_{48.8}Mn_{29.7}Ga_{21.5}$. Recent results suggest, that the modulated structures of the Ni-Mn-Ga alloy system, where the magnetic field induced strains are observed, are closely related to the nonmodulated tetragonal $L1_0$-structure. In particular, Kaufmann *et al.* showed, that the modulated structures can be constructed from different variants of the nonmodulated structure [90]. In this case, the different variants are connected by microscopic twin boundaries that appear periodically in the crystal. The underlying idea is known as the concept of adaptive martensite and was established in 1991 by Khachaturyan *et al.* [91].

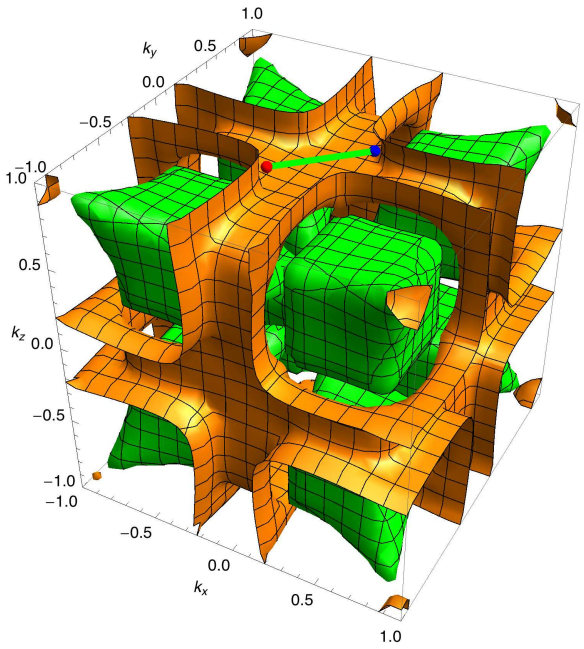

Figure 3.5: Fermi surface of the minority spin-channel of Ni_2MnGa. The Γ-point is found at the center and at each corner of the surrounding cube. The different colors denote different bands. For a better understanding the nesting vector $[\xi\xi 0]$ with $\xi \approx 0.4$ is also plotted. Figure adapted from Ref. [92]

In the temperature region where the structural transformation takes place, phonon softening is observed in Ni_2MnGa as well as in off-stoichiometric compositions [93]. Already in 1995 neutron scattering measurements of the stoichiometric composition from Zheludev *et al.* revealed a temperature dependent softening of one acoustic phonon branch along the $[\xi\xi 0]$ direction in the austenite structure [94]. The wave vector $\xi \approx 0.33$ where the softening appeared corresponds to the three-times modulated premartensitic structure, into which the crystal transformed upon cooling below 260 K [81]. Because of this mathematical relation the softening is often considered to be connected with the premartensitic transition rather than with the martensitic tranformation. The experimental findings of phonon softening have been successfully reproduced in the past using *ab initio* methods [95, 96]. In detail phonon calculations of the $L2_1$-structure reveal the softening of one acoustic phonon branch up to imaginary frequencies. This means that the austenite structure is not stable at $T = 0$ K. The wave vector where the softening appears is in agreement with the one that is observed in the neutron scattering measurements. The softening is therefore also theoretically interpreted as a precursor phenomenon of the premartensitic transition.

It is known that the reasons for phonon anomalies often can be found in the electronic band

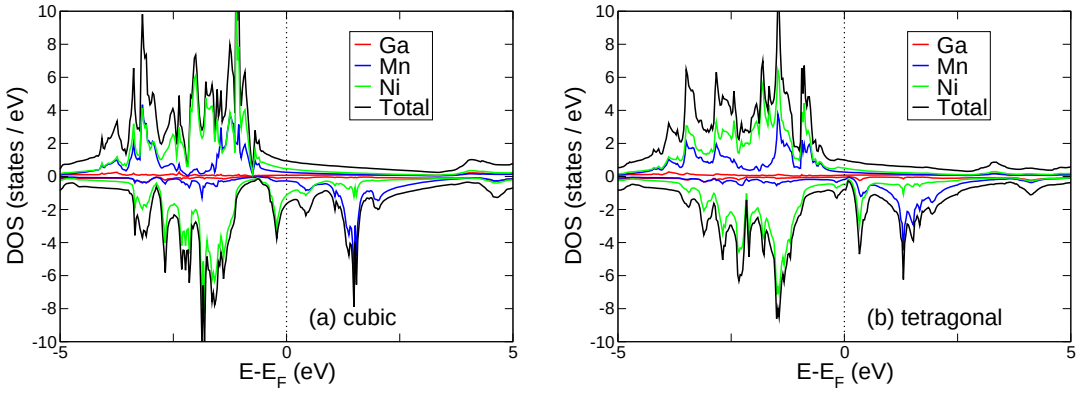

Figure 3.6: Electronic density of states (DOS) of Ni_2MnGa for (a) the cubic case and (b) the tetragonal case. The c/a ratio which describes the ratio between the two different crystal cell parameters is 1.26 in the tetragonal case. It is clearly visible that the peak situated just below E_F in (a), which can be related to the Ni atoms, splits up and mainly is shifted above E_F in (b). Figures adapted from Ref. [3].

structure near the Fermi level, more precisely in the shape of the Fermi surface [53, 97, 98]. In particular nesting effects of the Fermi surface, associated with large values of the generalized susceptibility $\chi(\mathbf{q})$, are related to such anomalies [99]. In Ni_2MnGa nesting of the Fermi surface is observed in the minority-spin channel in *ab initio* calculations [95, 92]. The corresponding Fermi surface is plotted in Fig. 3.5. However, the nesting vector is found at $\xi \approx 0.4$ and therefore does not correspond to the modulation that is found in the premartensitic phase. First-principles calculations by Lee *et al.* reveal that the generalized susceptibility which considers the bands of the minority spin bands but also the generalized susceptibility which considers the majority spin bands reveals a peak at this specific wave vector [100]. In the same article the authors showed, that the position of the peak for the susceptibility which takes into accounts the bands of the majority spin-channel is reduced to $\xi \approx \frac{1}{3}$ as the magnetic moment is reduced. This indicates, that the different modulations, which appear at different temperatures in Ni_2MnGa, may be explained by changes of the electronic structure caused by finite temperature effects and that nesting effects of both, majority spin and minority spin Fermi surface might be important regarding the appearance of the martensitic transformation.

Apart from the shape of the Fermi surface also another property of the electronic structure is important for the description of the martensitic transformation in Ni_2MnGa. In particular, the band Jahn-Teller effect has been observed experimentally and theoretically [101, 64]. The band Jahn-Teller appears in certain systems which are able to lower their energy by breaking their symmetry. In the case of Ni_2MnGa this means that the cubic symmetry is broken (which leads to a tetragonal symmetry). By breaking the symmetry a peak situated just below the Fermi level in the minority spin-channel of the electronic density of states (DOS) which is associated with the Ni atoms is split up into two parts. While one part is shifted above

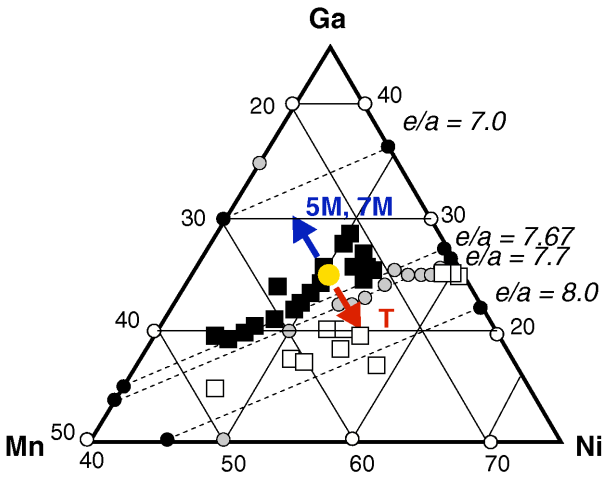

Figure 3.7: Excerpt from the ternary phase diagram of Ni-Mn-Ga. The capital letter T refers to non-modulated tetragonal structures whereas the yellow dot corresponds to the stoichiometric composition Ni_2MnGa. Figure adapted from Ref. [103].

the Fermi level (and therefore is not occupied any more) the other part is shifted to a lower energy (see Fig. 3.6). Thereby the band energy of the tetragonal structure is lower than the band energy of the austenite structure. As density functional theory calculations provide the possibility to directly investigate the electronic DOS of a specific material, they may be considered as an important tool to study the role of the band Jahn-Teller effect in the field of martensitic transformation.

By systematically changing the composition, fundamental properties of Ni-Mn-Ga, like for example the magnetocrystalline anisotropy energy (MAE) [59], can be tuned. This is of interest as the martensitic transformation temperature of Ni_2MnGa is rather low and the material also is rather brittle [102]. While the stoichiometric composition Ni_2MnGa shows a premartensitic transformation from the austenite structure into the 3M-phase upon cooling, this phase disappears when adding Ni in favour of Mn to the system because the martensitic transformation temperature increases while the premartensitic transformation temperature does not change significantly as Ni is added to the system [103]. Another approach to increase the transformation temperature is the substitution of Gallium by Manganese. This type of substitution will be discussed in detail in chapter 5. While excess Mn increases the transformation temperature, it has been observed experimentally that even small amounts of excess Ga in favour of Ni decrease the martensitic transformation temperature below 4.2 K in a polycrystalline sample [104]. The search for optimal compositions is even more challenging as it has been observed that the increase of the martensitic transformation temperature often goes hand in hand with a reduction of the Curie temperature [105, 106].

The composition dependent properties of Ni-Mn-Ga can be extracted from the ternary

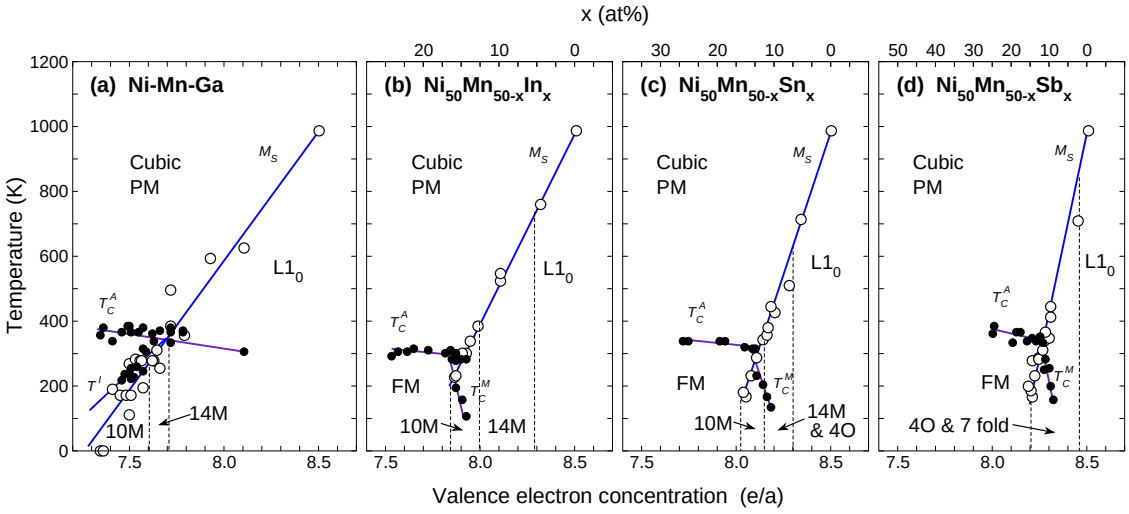

Figure 3.8: Experimental phase diagram of $Ni_{50}Mn_{50-x}Z_x$ (Z =Ga, In, Sn, Sb). The open circles denote measurements of M_S while the closed circles denote measurements of T_C. In case of Ni-Mn-Ga the atomic concentration of the nickel atoms is not fixed which results in rather scattered data points. Figure adapted from Ref. [105].

phase diagram [106, 103]. An excerpt of this phase diagram is plotted in Fig. 3.7. It shows that non-modulated tetragonal structures become preferred with increasing valence electron concentration e/a while modulated structures like the 5M or the 7M structure become preferred as e/a is decreased (see also Ref. [107]).

By replacing Ga with In, Sn, or Sb further Heusler alloys are obtained which also reveal magnetic shape memory properties for certain compositions [108]. The combination of the different types of possible substitutions gives rise to several more or less rich phase diagrams containing information on the compositional dependency of structural and magnetic transformation temperatures of the investigated magnetic shape memory alloy systems [105]. An example for such a series of phase diagrams is plotted in Fig. 3.8 which has been published by Planes *et al.* based on experimental results [105]. One of the key features that can be extracted from Fig. 3.8 is the linear dependency of the transformation temperature M_S (which will be denoted as T_M in the following unless it is mentioned in the context of experimental measurements or with regard to the other martensitic transformation temperatures M_F, A_S, and A_F) on the valence electron concentation e/a. In the present work it will be shown that *ab initio methods*, in particular density functional theory calculations, are able to model such phase diagrams and predict phase diagrams for new magnetic shape memory materials.

Chapter 4

Ab Initio investigation of the martensitic phase transformation in Ni_2MnGa

This chapter will describe the different methods that are available when trying to determine the structural phase transition temperature T_M. It will focus on the stoichiometric case Ni_2MnGa which is easy to handle in the calculations. In later parts of this work the methods which are introduced here will also be applied to off-stoichiometric compositions.

It has recently been shown that correlation effects related to localized electrons significantly influence the electronic and structural properties of Ni_2MnGa [109]. The effect of such electronic correlations on the results which are presented here is briefly discussed in section 4.4.

The last section of the chapter focuses on the influence of Fermi surface nesting on the martensitic transformation in Ni_2MnGa. Here, special emphasis is devoted to the role of the generalized susceptibility, thereby expanding previous works on this topic by other authors.

The two phases of Ni_2MnGa that will be discussed here are the high temperature $L2_1$-structure (austenite) and the nonmodulated tetragonal martensite structure ($L1_0$-structure) which is found to be the ground state of the stoichiometric composition at very low temperatures while modulated structures appear at other compositions or higher temperatures [103]. The tetragonality of the $L1_0$-structure is defined by the c/a ratio which describes the ratio of the two different crystal cell parameters in a tetragonal symmetry ($a = b \neq c$). In the case of Ni_2MnGa the c/a ratio of the $L1_0$-structure is 1.26 [110, 103, 3].

In classical thermodynamics the phase transformation temperature is derived as the point where the free energies of two different phases are equal. It is shown in equation (2.45) that the free energy taking into account the vibrational entropy can be calculated when the vibrational density of states $g(\omega)$ is known. Thus, the calculation of the phonon spectrum of the $L2_1$- and $L1_0$-structure of Ni_2MnGa will give rise to the transformation temperature within the harmonic approximation.

4.1 The phonon dispersion curves of Ni_2MnGa

Fig. 4.1 contains the calculated phonon dispersion curve of the $L2_1$-structure of stoichiometric Ni_2MnGa and the experimental results of neutron scattering measurements for a stoichiometric sample of Ni_2MnGa by Ener *et al.* [111]. A $4 \times 4 \times 4$ supercell containing 256 atoms was used to calculate the force constant matrices. The diagonalization of the dynamical matrices was carried out using the PHON code [44]. In case of the cubic structure and the $4 \times 4 \times 4$

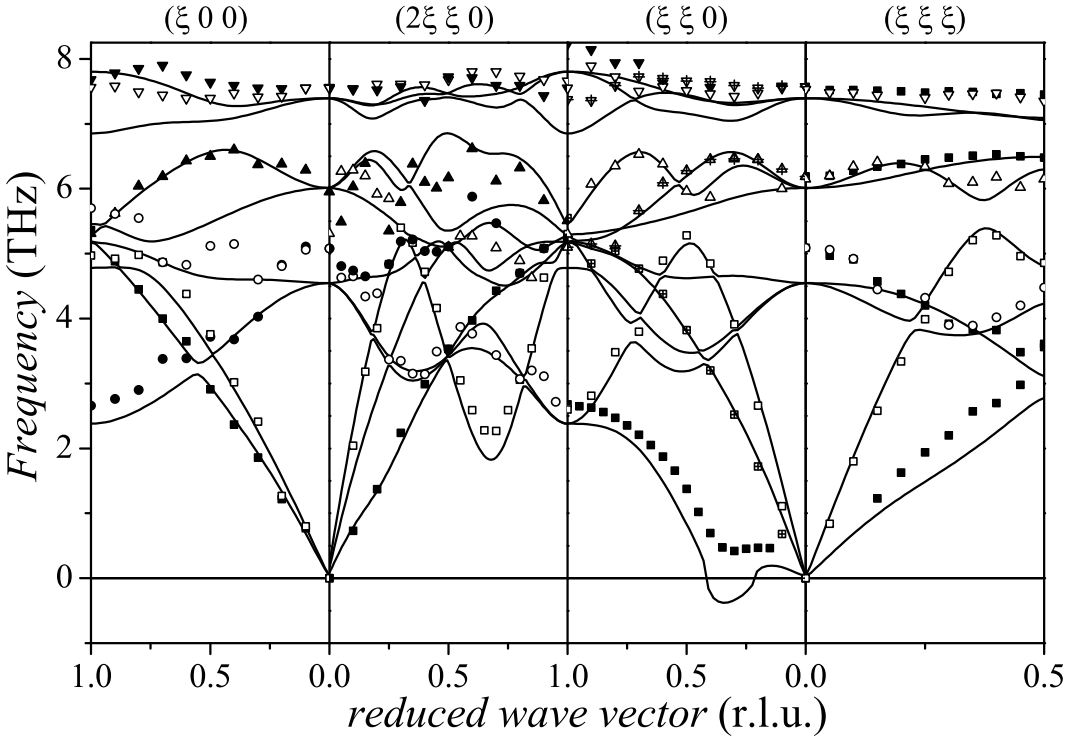

Figure 4.1: Phonon dispersion spectrum of stoichiometric Ni_2MnGa. The lines refer to *ab initio* calculations while the symbols denote results of neutron scattering measurements. Figure adapted from Ref. [111].

supercell the forces needed to obtain the force constant matrices were calculated by M. E. Gruner using VASP [37, 38], pseudopotentials based on the projector augmented wave (PAW) method [35], Methfessel-Paxton smearing [112], and the generalized gradient approximation in the formulation of Perdew, Burke and Ernzerhof as exchange-correlation functional [14]. A $2 \times 2 \times 2$ k-point set, an energy cut-off of 500 eV and Methfessel-Paxtion smearing with a smearing parameter of $\sigma = 0.1$ eV were used as the parameters of the calculation. The phonons were calculated for the ground state lattice constant of the $L2_1$-structure ($a_0 = 5.815$ Å) and the atoms were displaced by 0.02 Å in order to compute the force constant matrices. It is clearly visible that the measurements and the calculations are in good agreement in most parts of the Brillouin zone. A significant disagreement however appears along the [$\xi\xi$0] direction. Here the frequencies of the lowest lying acoustical branch become imaginary in the calculations which means that the structure is not stable. As the *ab initio* calculations are performed at $T = 0$ K while the measurements are carried out at 300 K, the difference between the calculations and the measurements already gives a clue that finite temperature effects are needed to stabilize the $L2_1$-structure. It should be mentioned that the results obtained within the density functional theory calculations are in good agreement with previously published

theoretical results [95, 96, 113].

Besides the phonon dispersion of the cubic structure the phonon spectrum of the $L1_0$-structure has also been calculated. For this structure, which has a lower symmetry, the k-point grid was increased to $4 \times 4 \times 4$ points in k-space. At the same time, the lattice constant was reduced to the ground state lattice constant of the $L1_0$-structure ($a_0 = 5.805\,\text{Å}$) and also the energy cut-off was reduced to 450 eV. As can be seen in Fig. 4.2 (a) the imaginary frequencies along the [$\xi\xi$0] direction disappear in the $L1_0$-structure which means that the structure is stable. The results are furthermore in good agreement with previous calculations of the phonon dispersion along the [$\xi\xi$0] direction of Zayak *et al.* [96, 114]. However, the $4 \times 4 \times 4$ supercell that has been used here makes it possible to look at different directions of the phonon spectrum or even sample the whole Brillouin zone while the calculations of Zayak *et al.* focused on the [$\xi\xi$0] direction and used a special supercell where the unit cell only was repeated along the direction of interest.

In order to obtain the vibrational density of states $g(\omega)$, it is necessary to not only look at directions of high symmetry but to take into account all **q**-values by integrating over the total Brillouin zone. For both cases, austenite and martensite structure, the Brillouin zone integration was performed using $61 \times 61 \times 61$ **q**-points. It should be noted here that the calculation of the dynamical matrix as described in equation (2.38) is only correct for wave vectors that are commensurate with the positions of the atoms in the supercell. In all other cases the values of the frequencies are interpolated. This is also true for the dispersion curves.

The element-resolved vibrational density of states (VDOS) of the austenite and martensite structure that are obtained using the Brillouin zone integration are plotted in Fig. 4.2 (b-c). One of the main differences between the two VDOS-curves is located in the region of the lowest optical branches around 4 THz. In the $L2_1$-structure the frequency values near this point are occupied mainly by the Ni atoms while the maximum of the contribution of the Ga atoms to the VDOS is located at 6 THz. This behaviour is unexpected as the Ga atoms have the largest mass of all involved atoms and should therefore be oscillating at the lowest optical frequencies. At these frequencies, however, the Ni atoms are found in the VDOS. In the past this anomalous behaviour has already been observed in the vibrational density of states obtained by a phonon calculation along the [$\xi\xi$0] direction [113] and is therefore related to oscillations along this direction which also reveals the imaginary frequencies. In contrast to this, the $L1_0$-structure shows a behaviour that is as expected. The maximum of the Ga contribution is now situated at 4 THz and is as large as the contribution of the Ni atoms at this point. It should be noted in this context, that the Ni contribution is twice as high as the contribution of the other two atom types as there are two Ni atoms in the primitive cell.

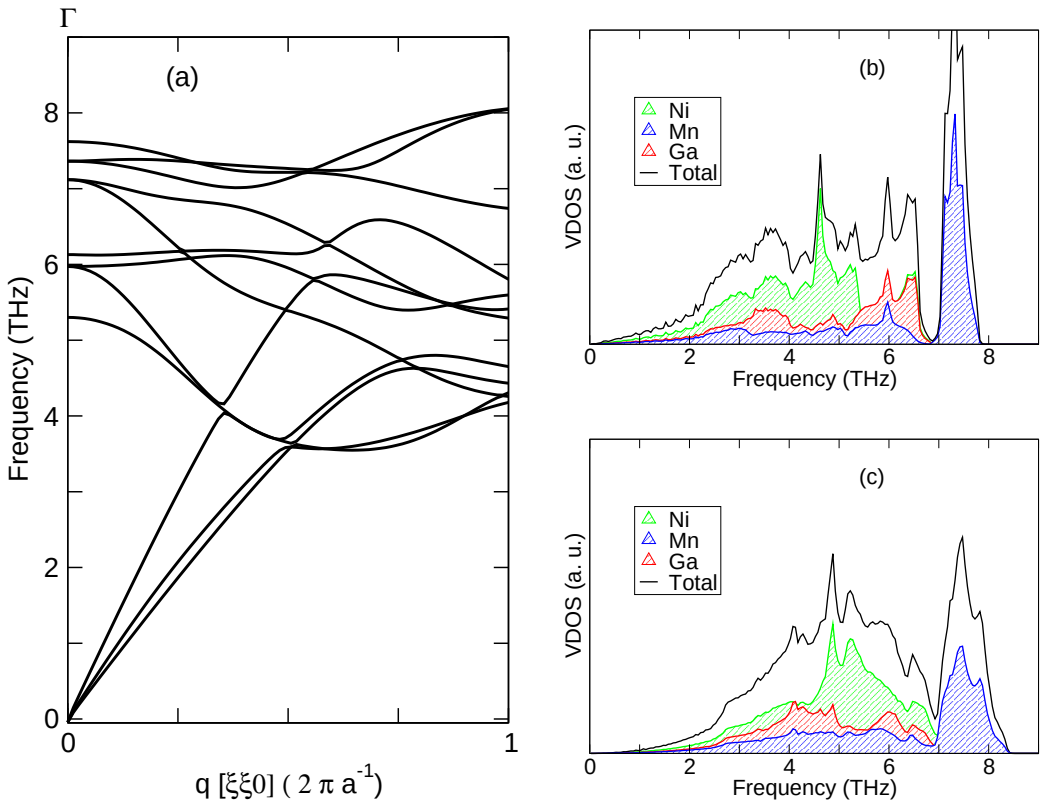

Figure 4.2: (a) Phonon dispersion along the [ξξ0] direction of the $L1_0$-structure of stoichiometric Ni_2MnGa. Vibrational density of states (VDOS) of (b) the $L2_1$-structure and (c) the $L1_0$-structure.

4.2 Determination of T_M within the harmonic approximation

After the determination of the vibrational densities of states by Brillouin zone integration the free energy of the austenite and martensite structure has been calculated using equation (2.45). The temperature dependent free energies of both structures are illustrated in Fig. 4.3. It should be noted here that besides the free energy of the lattice vibrations also the ground state energy obtained with the VASP code has to be taken into account when comparing the free energies of the two phases. As the ground state energy of the $L1_0$-structure is 27.25 meV/f.u. lower than the ground state energy of the $L2_1$-structure [3], this value has been subtracted from the original free energy curve of the martensite structure to obtain Fig. 4.3. The phase transformation temperature, i.e. the crossing of the free energy curves of the two structures, is found at $T_M \approx 315\,K$. This value overestimates the experimental value (202 K [115, 78]) by more than 100 K. There are several reasons for this discrepancy. On the one hand the measured transformation temperature depends on the quality of the sample, i.e. the amount of stacking faults and lattice defects. On the other hand stoichiometric Ni_2MnGa undergoes several phase transformations when cooling from the austenite structure, including the premartensitic phase, whereas the

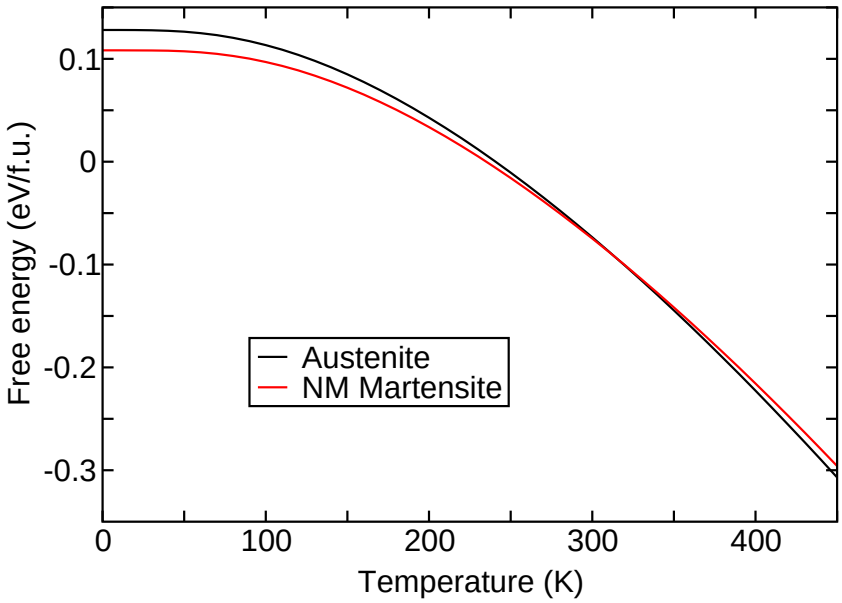

Figure 4.3: Temperature dependent free energy $F(T)$ for the $L2_1$-structure (austenite) and the $L1_0$-structure (nonmodulated martensite) of Ni_2MnGa obtained within the harmonic approximation.

calculations only take into account the austenite structure and the low temperature martensite structure. However, the most important reason for the discrepancy is found in the method that was used, i.e. the harmonic approximation. As it does not take into account finite temperature effects like the phonon-phonon interaction (which can theoretically be described taking into account anharmonic terms of the lattice Hamiltonian [116, 117, 118]) or the influence of finite temperature on the magnetic properties of the system. Therefore, the obtained value of 315 K for the phase transformation temperature should be regarded as a first approximation. Another problem that turns up in the specific case of Ni_2MnGa is the question how to deal with imaginary frequencies when calculating the free energy. In this work they have been neglected as the values of $g(\omega)$ are only of interest for real frequency values in the calculation of $F(T)$. However, it is clear that, as soon as the imaginary phonon branches become real with increasing temperature, the values of $g(\omega)$ will also change in the frequency interval where the former imaginary phonon branches appear.

4.3 Estimation of the transformation temperature using further methods

The results of the harmonic approximation can be increased when taking into account the volume expansion that is related with an increase of the temperature. This approach is called the quasi-harmonic approximation. In 2009, Uijttewaal *et al.* showed that the use of the quasi-harmonic approximation leads to an estimated phase transition temperature be-

low 300K ($T_M \approx 270\,K$) [119]. Thus, the use of the quasi-harmonic approximation enhances the agreement between theory and experiment although a significant discrepancy still remains. However, Uijttewaal *et al.* showed in the same paper, that this discrepancy and also the correct order of phase transformations can be obtained by taking into account also magnetic excitations besides the vibrational excitations. The magnetic vibrations were treated by reducing the magnetic moment in the phonon calculations according to an $M(T)$-curve in this case. Although this yields accurate results, the procedure is not completely *ab initio* anymore and, more importantly, requires a lot of computational effort as the phonon calculations have to be carried out for several magnetic moments.

Besides the calculation of free energies using the harmonic approximation other models also allow the estimation of the phase transformation temperature. For example in 2002 Enkovaara *et al.* used the Debye model and found a value for the transition temperature at around 175 K [120]. In the following, a simple approach that is able to estimate the transformation temperature based on the differences of the ground state energies of different structures will be introduced and motivated.

As it has already been pointed out, the total energy obtained with DFT calculations is lower for the $L1_0$-structure of Ni_2MnGa than for the $L2_1$-structure. The value of the energy difference between the two structures can be determined through the calculation of an $E(c/a)$-curve. In such a calculation the degree of tetragonality that is described by the c/a ratio is varied in order to find global and local minima of the total energy. In the interval between $c/a = 1$ (bcc) and $c/a = \sqrt{2}$ (fcc) the c/a-variation corresponds to the Bain path. The $E(c/a)$-curve of stoichiometric Ni_2MnGa has already been calculated in the past [121, 103, 3]. From the $E(c/a)$-curve the degree of tetragonality of the $L1_0$-structure (if it exists) can be extracted as well as the energy difference per atom between the $L2_1$- and $L1_0$-structure. The idea is now to relate this energy difference ΔE to the temperature that is needed to overcome the potential wall between the two structures in a first approximation. In other words,

$$\Delta E \approx k_B T_M \tag{4.1}$$

is assumed, where k_B is the Boltzmann constant and T_M the transition temperature between austenite and martensite. Using this equation a phase transformation temperature of 79.1 K is obtained for Ni_2MnGa which drastically underestimates the experimental value. Fig. 4.6 (a) exemplifies the described approach for the case of Ni_2MnGa.

As already mentioned before, the magnetic excitations have to be taken into account in order to correctly describe the martensitic phase transformation that is taking place in Ni_2MnGa. A possibility to include the magnetic excitations is the calculation of the magnon spectrum and derive the free energy contribution of the magnetic excitations using the harmonic approximation in analogy to the case of the lattice contribution. The magnon dispersion of Ni_2MnGa is exemplary presented in Fig. 4.4. It is clearly visible that the magnon energies are by an order of magnitude larger than the phonon energies, cf. Fig. 4.1. Furthermore, in agreement

with neutron spectroscopy measurements no softening can be observed in the acoustic magnon branch [122].

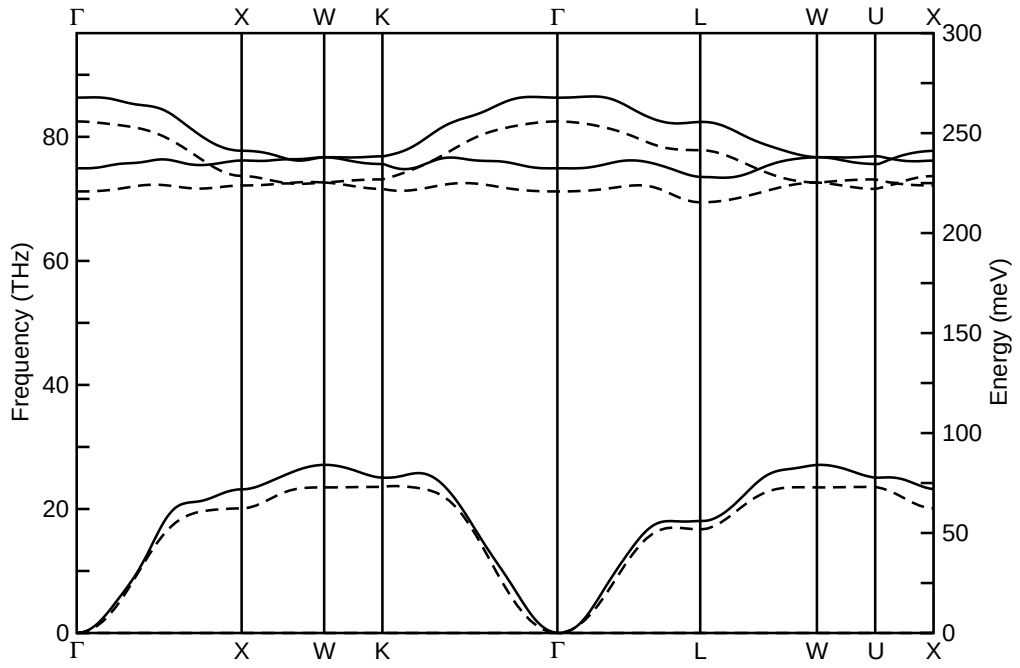

Figure 4.4: The magnon dispersion of the $L2_1$-structure of Ni_2MnGa. The solid curves have been obtained using the method described in section 2.3 and a set of exchange parameters calculated by Markus E. Gruner using the SPR-KKR code which makes use of the KKR approach [123, 124, 125, 126]. The dashed curves refer to results from Arthur Ernst which have been derived using the HUTSEPOT KKR code [127, 128].

In order to reduce the computational effort, the approach described in equation (4.1) can also be extended such that magnetic excitations can be taken into account without a calculation of the magnon spectrum. In particular, in the investigations of the $E(c/a)$-curves the effect of finite temperature on the magnetization can be treated by reducing the magnetic moment in the DFT calculations. In these so-called fixed spin moment (FSM) calculations the total magnetic moment of the investigated system is fixed to a specific value which actually becomes a parameter of the calculation [129, 130]. This is realized by assuming that the Fermi energies of the spin-up and spin-down channel are different [129].

The change of the magnetic moment, of course, influences the value of the total energy. Thus, by calculating $E(c/a)$-curves with a fixed magnetization, the influence of the reduction of the magnetization due to finite temperature on the energy difference between the different structures can be investigated. The complete binding energy surface $E(c/a, M)$ where M is the total magnetization has already been calculated in the past [131]. It turned out in these calculations, that a reduction of the magnetization leads to a decrease of the energy difference

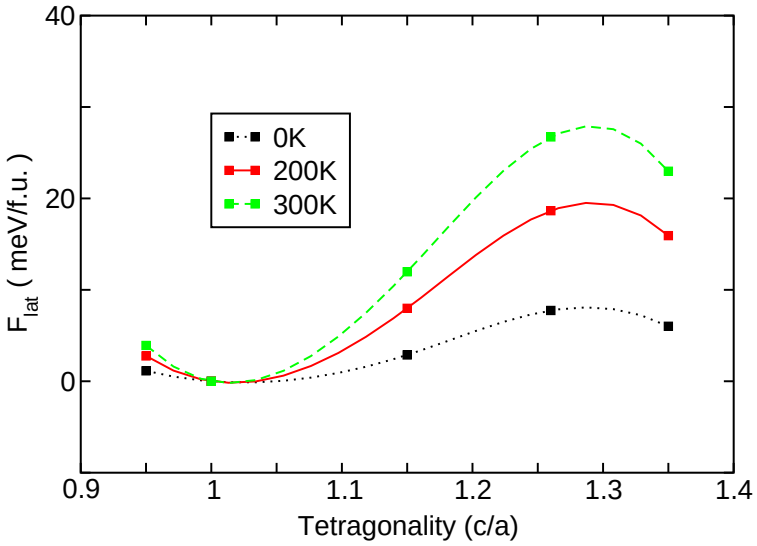

Figure 4.5: Lattice contribution to the free energy (F_{lat}) as a function of c/a. The values for each temperature are plotted relatively to the value of the cubic structure ($c/a = 1$) of the specific temperature. F_{lat} contains the phonon energy and the lattice entropy but neglects the total energy obtained from the DFT calculations. The calculated points are connected by a cubic spline interpolation function.

between the $L2_1$- and the $L1_0$-structure.

As the influence of the magnetic excitations on the $E(c/a)$-curves can be studied using the method described above, the question arises, whether the influence of the vibrational properties on the $E(c/a)$-curves can also be investigated. Fig. 4.5 contains the contribution of the lattice to the free energy (marked as F_{lat}) according to equation 2.45 for three different temperatures and five different c/a-ratios. The values of F_{lat} only contain the contribution of the phonons to the free energy but neglect the contribution from the total energy obtained from the DFT calculation. Due to the increased number of phonon spectra needed to calculate such a $F_{\text{lat}}(c/a)$-curve, the phonon spectra needed for the determination of the free energy curves have been calculated using a $3 \times 3 \times 3$ supercell containing 108 atoms. However, a comparison of the results for the $L2_1$- and $L1_0$-structure ($c/a = 1.26$) revealed, that the smaller size of the supercell does not influence the shape of the free energy curves significantly. Looking at the values of F_{lat} it is clearly visible that the cubic structure with $c/a = 1$ is preferred as the temperature is increased. In other words the lattice entropy stabilizes the austenite structure. If one now adds the DFT total energy curves given by $E(c/a)$ to the curve fitted through the values of F_{lat} one obtains the free energy F as a function of tetragonality c/a which is plotted in Fig. 4.6 (c). The phase transition temperature which is defined as the point where the two minima in the $F(c/a)$-curve are equal is found to be around 315 K and corresponds to the intersection of the two curves free energy curves which are plotted in Fig. 4.3.

The use of the $F(c/a)$-curves makes it possible to study the influence of lattice vibrations and magnetic excitations independently which allows to estimate the influence of both effects seperately. As it is shown in Fig. 4.6 different total energy curves $E_M(c/a)$ can be added to the phonon contribution F_{lat} to the free energy leading to different phase transformation temperatures. Here, the index M denotes the magnetization per formula unit which has been constrained using fixed spin moment calculations for values being smaller than the ground state magnetization ($M = 4.07\,\mu_{\mathrm{B}}$/f.u.). While the use of the $E(c/a)$-curve which is obtained for the ground state magnetization overestimates the transformation temperature, the value of T_{M} decreases when using an $E_M(c/a)$-curve where M is smaller than the ground state magnetization. This is in agreement with the results from Uijttewaal *et al.* [119]. Moreover, the method described above allows to understand the role of the different mechanisms involved in the phase transformation more exactly. For example, the $F_{\mathrm{lat}}(c/a)$-curves reveal that the lattice entropy stabilizes the austenite structure as the temperature is increased. On the other hand the fixed spin moment calculations show that the energy difference between austenite and martensite structure is maximized at the ground state magnetization. This allows to draw the conclusion that the martensite structure is stabilized by the magnetic moment which increases with decreasing temperature. This agrees with results from Gruner *et al.* who found that the phonon spectrum of cubic Ni_2MnGa becomes stable if the magnetization is reduced [131]. Nevertheless, the limitations of the described approach also should be pointed out. In particular, the different contributions from phonons and magnons are calculated seperately, thereby neglecting the magnon-phonon interaction which has been investigated in the past and was suggested to be the origin of the premartensitic transformation [132, 133, 134]. While it is in principle possible to include the magnon-phonon interaction by calculating for example phonon spectra for different magnetic moments the computational effort is significantly increased by such considerations, especially when also taking into account other finite temperature effects like volume expansion. The latter case requires that for each considered magnetization value several phonon spectra at different volumes are calculated.

Neglecting the contribution of the lattice vibrations by taking into account only the energy differences ΔE between austenite and martensite structure yields transition temperatures that do not agree quantitatively with the experimental results in the case of Ni_2MnGa. However, it turns out that this approach is able to model basic trends of the transition temperature in many alloy systems and also is in quantitative agrement with experimental results in some cases. The benefit of estimating the transition temperature from structural energy differences is the decreased computational effort compared to other methods. Especially the absence of phonon calculations significantly reduces the computational demand. This makes the approach also valuable for the investigation of off-stoichiometric compositions, as the computation of phonon spectra for such compositions is still a challenging issue. The calculation of the phonon spectrum for a primitive cell which contains four atoms in case of a Heusler alloy already requires density functional theory calculations using supercells containing more than a hundred

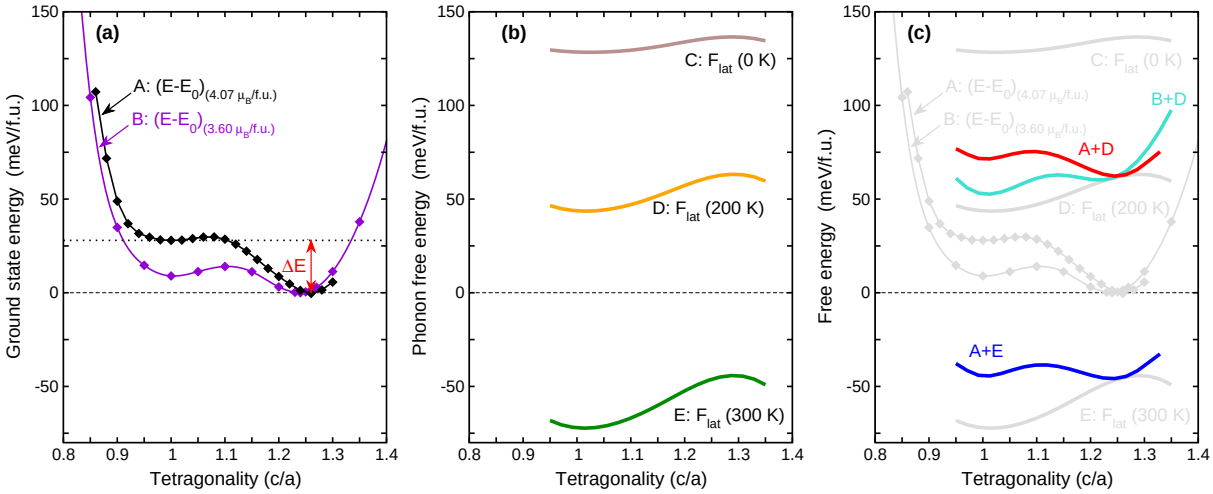

Figure 4.6: (a) Magnetization dependent total energy E_M, (b) lattice contribution to the free energy F_{lat}, and (c) the sum of the different contributions for Ni_2MnGa as a function of c/a. The energy difference ΔE between austenite and martensite structure (marked as red) is also included in (a) for the $E(c/a)$-curve which belongs to the ground state magnetization. Figure partially adapted from [135].

atoms for a proper grid of phonon wave vectors. If the same method is used to calculate the phonon spectrum of an off-stoichiometric composition the primitive cell of such a composition already contains more than four atoms which even further increases the size of the supercell that is needed in the phonon calculation if the resolution of the grid of phonon wave vectors is not reduced.

4.4 Correlation effects and their impact on the martensitic transformation

As it has been pointed out in section 2.1.8 the effect of electronic correlations is often underestimated by density functional theory calculations in case of systems containing d-electrons in the valence state. Very recently the effect of a Hubbard U term on the relative phase stabilities of the austenite and tetragonal martensite structure of Ni_2MnGa has been investigated by Himmetoglu *et al.* [109]. The authors calculated the U values based on the method described by Cococcioni *et al.* [136]. They found that the preference of the tetragonal structure vanishes if $U = 5.97\,\text{eV}$ is applied to the Mn d-orbitals and no additional U term is introduced for the orbitals of the other atoms of the structure.

Nevertheless, based on photoemission spectra a U value of about 6 eV has been theoretically predicted for Ni [137]. Therefore, the influence of two different sets of the parameters U and J on the $E(c/a)$-curve will be discussed briefly in the following. The investigation is motivated by a constrained random-phase approximation (cRPA, see Refs. [27, 28]) calculation of U and J values for Ni_2MnGa by Şaşıoğlu *et al.* who predict $U = 3.09\,\text{eV}$ and $J = 0.75\,\text{eV}$ for Ni and

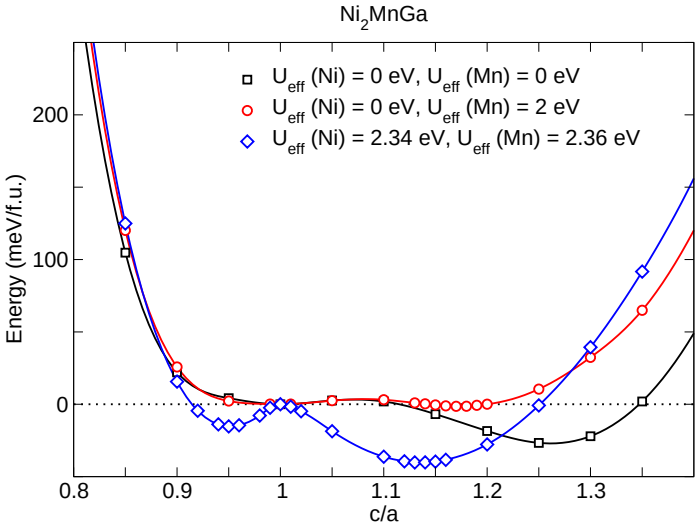

Figure 4.7: Energy as a function of c/a for different parameters of $U_{\text{eff}} = U - J$ in Ni_2MnGa. For each set of parameters the energy of the cubic structure ($c/a = 1$) is set to 0.

$U = 2.93\,\text{eV}$ and $J = 0.57\,\text{eV}$ for Mn [138].

Fig. 4.7 contains the $E(c/a)$-curves for two different sets of U and J which have been obtained using the VASP code, the PBE (GGA) exchange-correlation functional and the implementation of the GGA+U method by Dudarev *et al.* [25]. In addition, the curve which does not take into account additional U and J values is also included. All calculations have been performed at the corresponding ground state volumes of the cubic structures which means that the volume was kept fixed during the tetragonal transformation. The corresponding lattice constants as well as the partial magnetic moments of the cubic structures are contained in table 4.1.

It is clearly visible that the preference of the tetragonal structure is decreased when the additional terms which account for correlation are only considered for the Mn atoms. This is in agreement with the previous results by Himmetoglu *et al.* who used an even higher value for U in case of Mn [109].

A totally different $E(c/a)$-curve which corresponds rather to the case without taking into account correlation effects by an additional U is obtained when using the values from Şaşıoğlu *et al.* calculated within the cRPA. In this case the tetragonal $L1_0$-structure is clearly favoured over the $L2_1$-structure. In fact, the energy difference between the two structures even increases compared to the calculations without any U and a second minimum appears at $c/a < 1$.

The different sets of U and J values show that correlation effects significantly influence the results that are obtained when calculating the $E(c/a)$-curve of Ni_2MnGa. However, because of the fact that even the qualitative behaviour of the $E(c/a)$-curve strongly depends on the chosen values of U and J further investigations on the actual size of these quantities are required. Since it has been shown by Uijttewaal *et al.* that very accurate results for the different

Table 4.1: Effect of different values of U and J on the magnetic moments of the Mn and Ni atoms and the lattice constant of cubic Ni_2MnGa.

$U_{Mn}(eV)$	$J_{Mn}(eV)$	$U_{Ni}(eV)$	$J_{Ni}(eV)$	a(Å)	$M_{Mn}(\mu_B)$	$M_{Ni}(\mu_B)$
0	0	0	0	5.81	3.386	0.356
3	1	0	0	5.86	3.89	0.314
2.93	0.57	3.09	0.75	5.87	3.986	0.478

transformation temperatures including the premartensitic transformation temperature can be obtained for Ni_2MnGa from first-principles calculations without considering correlation effects seperately [119], no additional U values will be applied in the following.

4.5 Investigation of Fermi surface nesting effects in Ni_2MnGa

As it was mentioned before the appearance of the martensitic transformation in Ni_2MnGa is often linked to nesting effects appearing in the Fermi surface of this material. This is due to the appearance of modulated structures for certain compositions of the material. Velikokhatnyĭ *et al.* proposed that these long-period structures have to arrange because of long-range interactions caused by nesting effects of the Fermi surface [139]. Such behaviour is known from nonmagnetic shape-memory materials like NiTi or NiAl [140, 141, 142, 143].

Periodic lattice distortions that appear in crystals are often related to the so-called Peierls transition. The origin of this phenomenon which is named after Rudolf Peierls will be sketched in the following. For a one-dimensional chain of atoms with an odd number of electrons per ion it can be shown that a small distortion of every second atoms reduces the total energy of the system. The reason for this behaviour is found in the splitting of an electronic band crossing the Fermi level just between the zone boundary and the Γ-point. While the distortion increases the size of the primitive unit cell the size of the Brillouin zone decreases and the band structure becomes folded just at the Fermi wave vector. The splitting of the bands leads to an effective gain of energy because the lower part of the band (which is fully occupied) is shifted to lower energies while the upper part (which is not occupied) is shifted to higher energies [144]. Although the Peierls transition refers to a one-dimensional model system the idea behind it is also imagined to be the reason for distortions like charge density waves that appear in three-dimensional crystals although one has to keep in mind that the Peierls transition is very sensititve with regard to the particular shape of the Fermi surface [145, 144]. Nevertheless it is widely accepted that there is a close connection between phonon anomalies and the shape of the Fermi surface in certain metals [53, 146] which is of particular interest with regard to martensitic transformations [54] and motivates a detailed analysis of the Fermi surface in case of Ni_2MnGa.

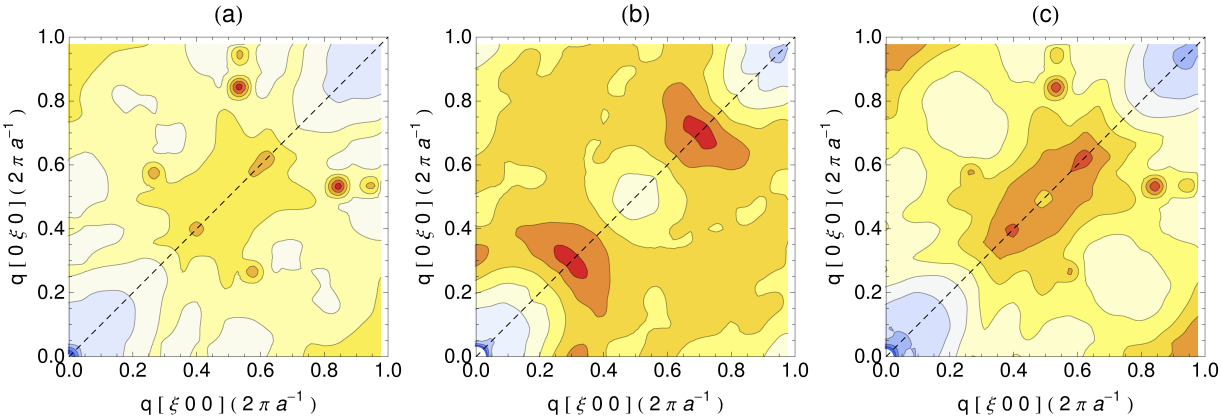

Figure 4.8: Generalized susceptibility $\chi(\mathbf{q})$ of Ni_2MnGa in the (001) plane in arbitrary units. In the evaluation of equation (4.2) all (a) spin-down, (b) spin-up, and (c) all bands crossing E_F have been considered. The color scale is not equal for the three different contour plots but has been chosen such that a clear contrast of the features of $\chi(\mathbf{q})$ is obtained for each contour plot. While blue corresponds to low values of the generalized susceptibility, red colours denote high values of $\chi(\mathbf{q})$. The dashed lines mark the [110] direction.

The Fermi surface of Ni_2MnGa has been calculated several times using *ab initio* methods [147, 92, 148, 95, 139]. In most of these calculations emphasis was put on the Fermi surface of the minority (spin-down) channel which consists of several rather flat sheets which already give a hint for the appearance of nesting (see Fig. 3.5). A quantitative description of the nesting features is obtained by the generalized susceptibility $\chi(\mathbf{q})$ which is defined as

$$\chi(\mathbf{q}) = \sum_{m,n,\mathbf{k}} \frac{f\left[\epsilon_m(\mathbf{k})\right]\left(1 - f\left[\epsilon_n(\mathbf{k}+\mathbf{q})\right]\right)}{\epsilon_n(\mathbf{k}+\mathbf{q}) - \epsilon_m(\mathbf{k})} \tag{4.2}$$

with f being the Fermi distribution function, $\mathbf{q}$ a reciprocal wave vector and $\epsilon_n(\mathbf{k})$ the energy of the n-th band at the electron wave vector $\mathbf{k}$ [100]. $\chi(\mathbf{q})$ describes the linear response of the conduction electrons to a perturbation introduced by a wave vector $\mathbf{q}$ [149, 150] and reveals peaks for such values of $\mathbf{q}$ which correspond to nesting vectors of the Fermi surface [99].

Different contributions of the generalized susceptibility $\chi(\mathbf{q})$ of Ni_2MnGa in the (001) plane are plotted in Fig. 4.8. Here, three different cases have been considered in the evaluation of the summation over the bands in equation (4.2) which is denoted by the indices m and n. In Fig. 4.8 (a) all bands in the spin-down channel which are crossing the Fermi level have been considered while in Fig. 4.8 (b) all bands of the spin-up channel obeying this condition have been considered. In Fig. 4.8 (c) bands from both spin-channels crossing the Fermi level have been considered in the evaluation of the sum in equation (4.2).

The behaviour of $\chi(\mathbf{q})$ along the [$\xi\xi$0] direction is obtained when following the dashed lines in Fig. 4.8. It is in agreement with previously published results of $\chi(\mathbf{q})$ along the [110] direction

[100, 139]. In particular, peaks at $\xi \approx 0.4$ and $\xi \approx 0.6$ are observed for the summation involving the minority bands. In case of the majority bands these peaks are shifted to $\xi \approx 0.3$ and $\xi \approx 0.7$. The fact that peaks of $\chi(\mathbf{q})$ also are observed when considering only the spin-up bands indicates that also in the majority Fermi surface nesting effects play a role [100]. Recent electronic structure calculations performed by Haynes *et al.* suggest that the peak positions of $\chi(\mathbf{q})$ which appear in different spin-channels are merged upon a reduction of the magnetic moment [147].

Looking at the whole (001) plane it is observed that for the calculations involving the spin-down bands, additional pronounced peaks of $\chi(\mathbf{q})$ appear at $\mathbf{q} \approx (0.55, 0.85, 0)$. Interestingly, the phonon dispersion of Ni_2MnGa does not reveal an anomalous behaviour of an acoustic phonon branch at this point. Thus, the investigation of the generalized susceptibility does not reveal a direct relation between the peaks of $\chi(\mathbf{q})$ which are associated with Fermi surface nesting and the phonon softening that is observed in the austenite structure of Ni_2MnGa. This is in agreement with previously published results where it was argued that the size of the electron-phonon matrix elements at the specific $\mathbf{q}$-vectors is also important for the appearance of the phonon anomaly, i.e. that the phase transition is driven by strong electron-phonon coupling [151, 95, 152].

It should however be pointed out that the peaks of the susceptibility which appear at $\mathbf{q} \approx (0.55, 0.85, 0)$ in the spin-down channel are very sharp while the increase of $\chi(\mathbf{q})$ which appears along the [110] direction is observed for a broad range of wave vectors. If the phonon softening is caused by the latter observation it is likely so suggest that the nesting of the Fermi surface of the majority spin-channel is as important or even more important than the nesting that is found in the Fermi surface of the minority-spin channel. This is because the values of $\chi(\mathbf{q})$ become more accentuated in the region of interest along the [110] direction when considering also the spin-up bands in the evaluation of the susceptibility (cf. Fig. 4.8). The observation that nesting of the majority spin Fermi surface might also be important for the appearance of phonon softening in Ni_2MnGa coincides with previous first-principles investigations by Lee *et al.* [100].

Chapter 5

The phase diagram of Ni-Mn-Z (Z = Ga, In, Sn, Sb)

As was pointed out already before, the magnetic shape memory reference material Ni_2MnGa still faces problems regarding its application in MSM devices that are operating at or above room temperature. A major issue is the martensitic transformation temperature that is too low for many industrial needs.

A common approach to overcome this problem and increase the transformation temperatures is the substitution of atoms in the alloy. In this sense, one may either completely replace one sort of atoms and consider, for example, Ni_2MnIn instead of Ni_2MnGa, or change the relative occurence of the different atom types. The latter approach gives rise to off-stoichiometric compositions. It is known, that the substitution of atoms can influence the value of T_C [153] as well as the value of T_M [154]. The valence electron concentration, in other words the number of valence electrons e per atom a (e/a) plays an important role regarding the occurence of martensitic phase transformations and the value of T_M. In 2002, Jin *et al.* showed that the martensitic transformation temperature of Ni_2MnGa increases nearly linear with e/a [155]. In accordance with these results, Zayak *et al.* discovered that the nearest neighbour force constants of several Heusler families decrease with increasing e/a ratio, which means that instabilities are introduced when increasing the valence electron concentration [156]. One way to increase the e/a ratio is the substitution of the Z atoms in Ni_2MnZ (Z = Ga, In, Sn, Sb) by additional manganese atoms which gives rise to the alloy system $Ni_2Mn_{1+x}Z_{1-x}$ with $0 \leq x \leq 1$. However, although the additional Mn atoms increase the valence electron concentration which is beneficial for the martensitic transformation temperature they also introduce antiferromagnetic interactions which give rise to antiferromagnetic alignments of spins lowering the total magnetic moment [157, 158, 159, 160]. This is disadvantageous as the magnetic energy that is required to move twin boundaries by applying a magnetic field in a magnetic shape memory material depends on the size of the magnetic moment. Thus, a larger magnetic moment reduces the magnetic field sizes that are needed to obtain a magnetic field induced strain (MFIS).

In 2009 Planes *et al.* published a comprehensive review where they reconstructed the phase diagram of the Ni-Mn-Z (Z = Ga, In, Sn, Sb) alloy series [105]. The data points they considered are illustrated in Fig. 3.8 and reveal two basic trends. First of all the martensitic transition temperature T_M increases linear in e/a independent from the atom type that is occupying the Z site. The second remarkable finding is the decrease of T_C with e/a. The critical magnetic temperature of the austenite, denoted as T_C^A, as well as the critical magnetic temperature of

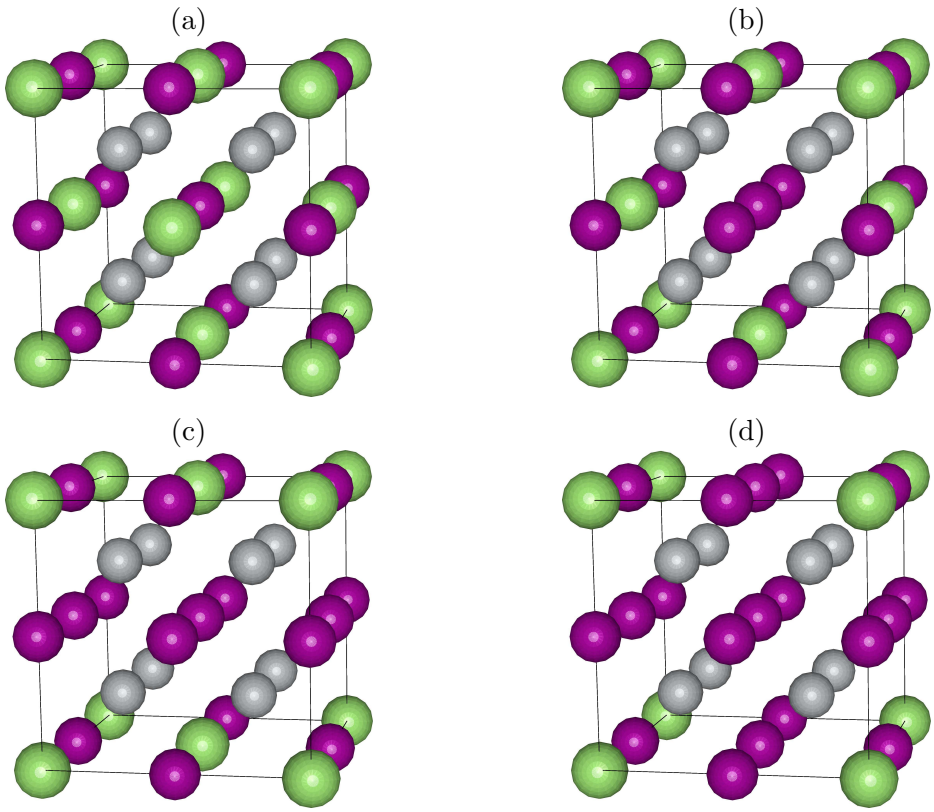

Figure 5.1: The supercell of Ni-Mn-Z containing 16 atoms that was used in the calculations. The Ni, Mn, and Z atoms are marked grey, purple, and green. (a) refers to the stoichoimetric composition Ni_2MnZ ($Ni_8Mn_4Z_4$ supercell), (b) to $Ni_2Mn_{1.25}Z_{0.75}$ ($Ni_8Mn_5Z_3$ supercell), (c) to $Ni_2Mn_{1.5}Z_{0.5}$ ($Ni_8Mn_6Z_2$ supercell), and (d) to the composition $Ni_2Mn_{1.75}Z_{0.25}$ (Ni_8Mn_7Z supercell).

the martensite, denoted as T_C^M, decrease linear with e/a. However, the slope of the T_C^A-curve is different from the slope of the T_C^M-curve. The scattering of the data points in the case of Ni-Mn-Ga is explained by the fact that for this alloy system data points with different concentrations of Ni were taken into account while for the other alloy systems the Ni-content was fixed to 50%.

In this chapter it will be shown how the methods, that have been introduced before, allow the modeling of phase diagrams based on the example of the Ni-Mn-Z ($Z =$ Ga, In, Sn, Sb) alloy series for which comprehensive experimental data is available. By comparing the theoretical and experimental results the reliability of the theoretical methods can be investigated before they are applied to new materials, which have not been studied as extensive as Ni-Mn-Z, in the next chapters. The modeling of concentration dependend phase diagrams requires the calculation of off-stoichoimetric compositions. Here, off-stoichiometry will be treated using the supercell approach. In this approach the primitive cell is repeated several times to obtain

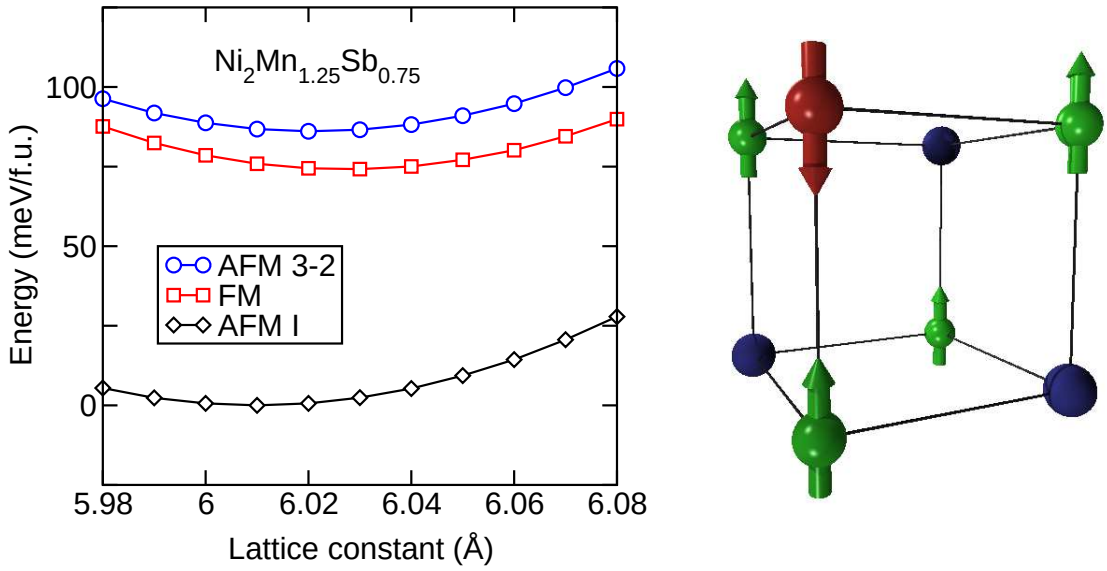

Figure 5.2: (left) Total energy E as a function of the lattice constant a of $Ni_2Mn_{1.25}Sb_{0.75}$ ($Ni_8Mn_5Sb_3$ supercell). (right) Schematic representation of the preferred magnetic order (AFM I) of the atoms in the $Ni_8Mn_5Sb_3$ supercell. All but the Ni atoms of the 16-atom supercell are plotted. The original Mn atoms are marked green while the additional Mn atom is marked red. The Sb atoms are marked as blue circles.

a larger supercell. By changing now the composition of the supercell, an off-stoichiometric composition of the primitive cell is obtained if the number of atoms of at least one of the atom types in the supercell is not a multiple of the number of primitive cells contained in the supercell. In case of the Ni_2MnZ Heusler alloys which have a primitive unit cell that consists of 4 atoms a supercell consisting of 16 atoms was used to study off-stoichiometric compositions in this work. By replacing one atom in the 16-atom supercell with an atom of another type the composition can thereby be changed by $\frac{1}{16} \mathrel{\hat{=}} 6.25\,\text{at.}\%$. Different compositions of the 16-atom supercell are plotted in Fig. 5.1.

While the supercell approach allows to calculate off-stoichiometric compositions without introducing additional computational methods it also faces some problems. The most severe one is the fact that the supercells itself are still considered to appear in perfect periodicity in the crystal. Thus, a random distribution of the atoms over the lattice sites as it is the case in disordered structures which might appear at off-stoichiometric compositions is not considered by the supercell approach. However, by calculating different configurations of the same composition and averaging the results the influence of disorder can in principle be approximated. Another limitation of the supercell approach originates from the fact that the number of atoms considered in the density functional theory calculation increases rapidly as the size of the supercell is increased. This means that the investigation of small compositional changes requires significant computational resources. It also arises the question how to deal

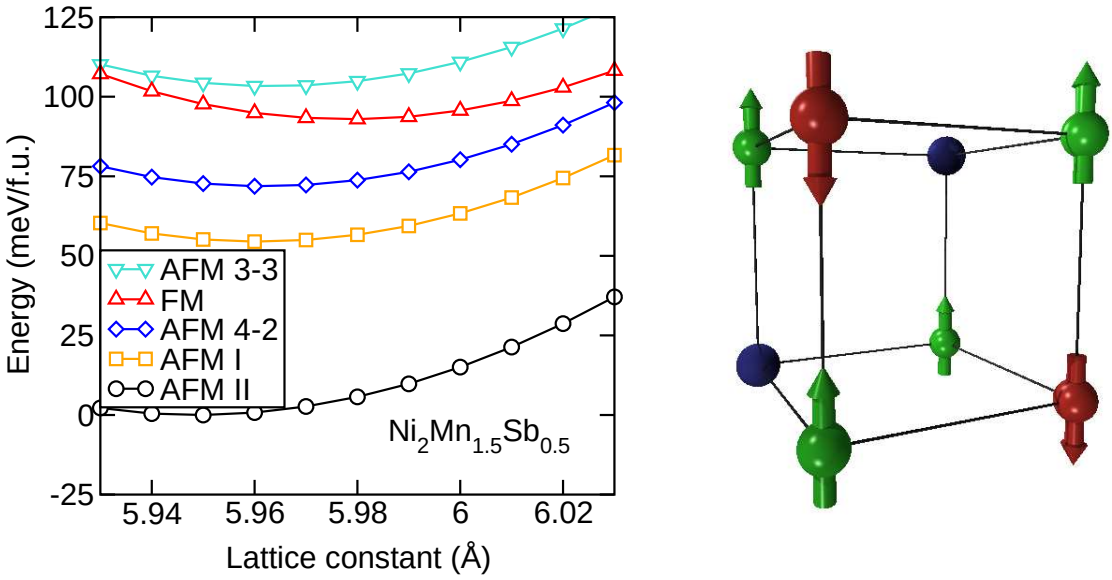

Figure 5.3: (left) Total energy E as a function of the lattice constant a of $Ni_2Mn_{1.5}Sb_{0.5}$ ($Ni_8Mn_6Sb_2$ supercell). (right) Schematic representation of the preferred magnetic order (AFM II) of the atoms in the $Ni_8Mn_6Sb_2$ supercell. All but the Ni atoms of the 16-atom supercell are plotted. The original Mn atoms are marked green while the additional Mn atoms are marked red. The Sb atoms are marked as blue circles.

with relaxations of the atoms from their ideal lattice positions when using supercells. This issue will be discussed in section 5.4.1.

5.1 Computational details

The supercell calculations were performed using VASP, PAW pseudopotentials and the PBE exchange-correlation functional. The $3p$ electrons of Ni and Mn as well as the $3d$ electrons of Ga and Sn were considered as valence electrons in the calculations and an energy cut-off of 459.9 eV was used. For the Brillouin zone integration the tetrahedron method with Blöchl corrections was applied [161]. A k-point grid containing $10 \times 10 \times 10$ points in the reciprocal space constructed using the method described by Monkhorst and Pack was used in the calculations [162]. In case of the stoichiometric compositions which can be calculated using a primitive cell containing 4 atoms the number of k-points was increased to $15 \times 15 \times 15$. The Fermi surface calculations were carried out using an even higher number of k-points. In particular, grid sizes of $31 \times 31 \times 31$ points centered around the Γ-point were used in this type of calculations.

5.2 Determination of the composition-dependent magnetic order

The 16-atom supercell allowed to consider three different Mn-rich compositions besides the stoichiometric composition which are plotted in Fig. 5.1 (b-d). As a first step, the ground state volume of the cubic structure was determined for all of these compositions. When adding manganese in favour of the Z atoms in the supercell the question arises which atomic sites are occupied by the additional Mn atoms. As is known that the nickel atoms occupy their cubic sublattice already at high temperatures in the B2-structure [80] the Ni sites were not considered when evaluating all possible configurations of the supercells. This significantly reduces the number of possible configurations. However, as the manganese atoms have a magnetic moment which is considered to be localized the magnetic spin introduces an additional degree of freedom [163, 164]. Therefore, different alignments of the magnetic moments of the manganese atoms (not only of the additional Mn atoms but also of the original Mn atoms) were considered when searching for the ground state volume of the cubic structure. Fig. 5.2 contains the $E(a)$-curve of $Ni_2Mn_{1.25}Sb_{0.75}$ ($Ni_8Mn_5Sb_3$ supercell) for three different types of magnetic orderings that are possible in the supercell. The black curve denotes the magnetic order where the magnetic moment of the additional Mn atom on the Sb site is aligned opposite to the magnetic moments of the Mn atoms on the original Mn sites while the red curve denotes a purely ferromagnetic alignment of the Mn moments. The blue curve contains results for a layerwise antiferromagnetic order of the Mn moments. Fig. 5.2 also illustrates the magnetic order that is favoured for the particular composition. It turns out that the spin of the additional manganese atom on the Sb site is aligned antiferromagnetic with respect to the magnetic moment of the manganese atoms on the original Mn sites in the ground state. A completely ferromagnetic alignment of the Mn atoms and also a layerwise antiferromagnetic order where the five Mn atoms of the supercell are seperated into layers of 2 and 3 atoms are energetically not favoured compared to the antiferromagnetic ground state.

Fig. 5.3 contains the results of a ground state determination for a second composition, namely $Ni_2Mn_{1.5}Sb_{0.5}$ ($Ni_8Mn_6Sb_2$ supercell). The black curve denotes the magnetic order where the magnetic moment of both additional Mn atoms on the Sb site is aligned opposite to the magnetic moments of the Mn atoms on the original Mn sites whereas the orange curve refers to the magnetic order where only one moment of the additional Mn atoms is aligned opposite to the moment of the Mn atoms on the original Mn sites. The red curve denotes a purely ferromagnetic alignment of the Mn moments and the blue and turquoise curves denote different types of layerwise antiferromagnetic orders where the numbers in the legend refer to the number of atoms per layer within the supercell. For this composition the favoured magnetic order is the one where the magnetic moments of the two additional manganese atoms on the Sb sites are aligned antiferromagnetically with respect to the magnetic moments of the manganese atoms on the Mn sites (see Fig. 5.3). For the particular composition $Ni_2Mn_{1.5}Sb_{0.5}$ even further configurations where the Sb atoms exchange their sites with Mn atoms were considered. The

resulting total energies however did not give any clue for such a change of the site occupancy at this composition.

It turns out that for all compositions where the magnetic order has been investigated the energetically favoured alignment of spins is always the configuration where the magnetic moments of the manganese atoms on the Z sites are aligned in the opposite direction than the magnetic moments of the manganese atoms on the original Mn sites. This observation is in agreement with the results from Lázpita *et al.* who investigated the alignment of magnetic moments in off-stoichiometric Ni-Mn-Ga alloys by a model which is based upon the results of neutron diffraction measurements [159]. The reason for this antiferromagnetic tendencies originates from the reduced distance between two manganese atoms in different sublattices compared to two manganese atoms in the same sublattice. While the Mn-Mn nearest neighbour (nn) distance is $\frac{a}{\sqrt{2}}$ in the $L2_1$-structure, where a is the lattice constant, the corresponding Mn-Z nn distance is $\frac{a}{2}$. This means that the distance between excess manganese atoms that occupy the Z site and manganese atoms that occupy the Mn site is reduced by the factor $\frac{1}{\sqrt{2}} \approx 71\%$ compared to the distance between two nearest neighbour manganese atoms that occupy the Mn sublattice. It is known that the alignment of spins in pure manganese strongly depends on the interatomic distance and ferromagnetic alignments become favoured with increasing distance [165, 166]. According to Kasper and Roberts the preferred alignment of spins switches from antiparallel to parallel order for distances larger than approximately 2.96 Å [165]. In the case of Ni_2MnGa ($a = 5.825$ Å [78]) the Mn-Mn distance is 4.119 Å while the Mn-Ga distance is 2.913 Å, which means that the threshold which divides ferromagnetic and antiferromagnetic spin order given by Kasper and Roberts lies just between these two distances. Thus, the antiferromagnetic spin alignment that is introduced when substituting Z atoms by Mn is related to the fact that the behaviour of the Mn atoms in the Heusler structure is quite similar to the behaviour in bulk Mn. The fact that the magnetic properties of Mn atoms in a Heusler structure depend on their local environment has recently also been investigated for Ni_2MnAl where an antiferromagnetic phase for certain degrees of disorder between the Mn and Al sublattices has been observed [167]. Nevertheless it should be reminded that the addition of manganese increases the valence electron e/a of the alloy. It is known from the Slater-Pauling curve that the magnetization increases linear with e/a for small e/a ratios but decreases linear with e/a for large e/a ratios [168]. Thus, the decreasing total magnetic moments which go hand in hand with the antiferromagnetic alignments of the Mn spins that appear upon the addition of Mn can also be viewed in the context of the e/a variation which is connected with the substitution. This issue will be discussed in detail in section 5.3. It should also be mentioned at this point that in case of Ni-Mn-In the ground state changes from an antiferromagnetic to a ferromagnetic structure when allowing for relaxation of the atomic positions in the supercell. This issue will be discussed in detail in section 5.4.1.

Beside the introduction of antiferromagnetic interactions it is observed that the addition of manganese leads to a reduction of the lattice constant compared to the stoichiometric

Table 5.1: Properties of the cubic structures with $c/a = 1$ of the considered compositions of the Ni-based Heusler alloys. The values for the stoichiometric compositions have been taken from Ref. [3].

System	e/a	a(Å)	$M(\mu_B$/f.u.)
Ni_2MnGa	7.5	5.813	4.07
$Ni_2Mn_{1.25}Ga_{0.75}$	7.75	5.815	3.11
$Ni_2Mn_{1.5}Ga_{0.5}$	8.0	5.81	2.05
$Ni_2Mn_{1.75}Ga_{0.25}$	8.25	5.81	0.94
Ni_2MnIn	7.5	6.07	4.21
$Ni_2Mn_{1.25}In_{0.75}$	7.75	6.013	3.18
$Ni_2Mn_{1.5}In_{0.5}$	8.0	5.95	2.11
$Ni_2Mn_{1.75}In_{0.25}$	8.25	5.885	1.0
Ni_2MnSn	7.75	6.06	4.08
$Ni_2Mn_{1.25}Sn_{0.75}$	7.94	6.01	2.94
$Ni_2Mn_{1.5}Sn_{0.5}$	8.13	5.95	1.93
$Ni_2Mn_{1.75}Sn_{0.25}$	8.31	5.89	0.94
Ni_2MnSb	8.0	6.07	3.99
$Ni_2Mn_{1.25}Sb_{0.75}$	8.13	6.01	2.86
$Ni_2Mn_{1.5}Sb_{0.5}$	8.25	5.95	1.76
$Ni_2Mn_{1.75}Sb_{0.25}$	8.38	5.884	0.8

composition. This behaviour is expected, as the Mn atoms are smaller than the Z atoms and it is also observed experimentally [105, 169]. Table 5.1 contains the e/a ratios, the lattice constants and the magnetic moments for the cubic structures ($c/a = 1$) of the investigated compositions.

5.3 Influence of e/a on the magnetic properties

As was pointed out before, the appearance of antiferromagnetic spin order that appears when manganese is added to the system can also be related to the number valence electrons per atom, e/a.

Fig 5.4 (a) contains the magnetic moment of the computed supercells as a function of e/a, i.e. the Slater-Pauling curve for the antiferromagnetic alignments of additional Mn moments which is in good agreement with experimental measurements except for the Ni-Mn-In system which is found at higher magnetic moments in the experiment and also reveals a maximal magnetic moment for an Mn-rich composition [170]. It is clearly visible that the total magnetization which is about $4\,\mu_B/f.u.$ is reduced in a linear manner as the valence electron concentration is

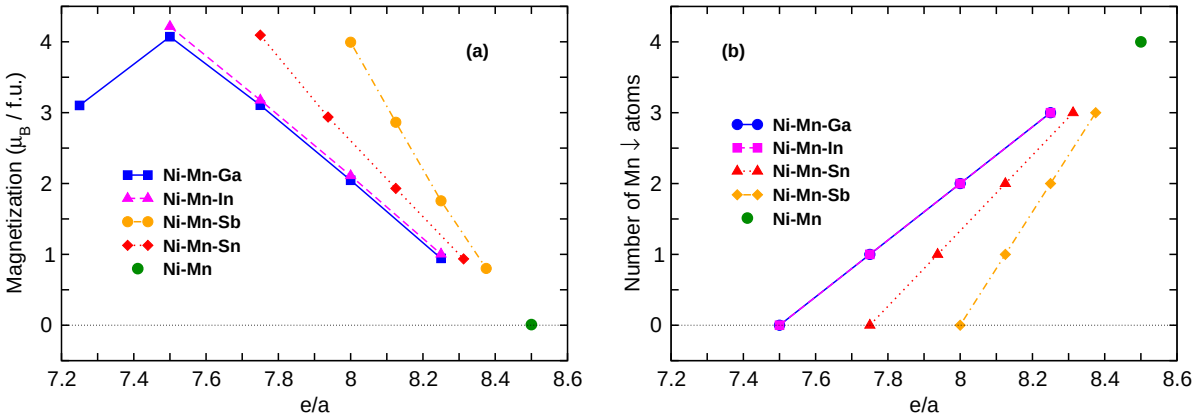

Figure 5.4: (a) Magnetization per formula unit (4 atoms) and (b) number of spin-down manganese atoms per supercell (16 atoms) of Ni-Mn-Z as a function of the valence electron concentration e/a. Figure taken from [135].

increased. The linear behaviour is directly related to the antiferromagnetic alignment of Mn moments that has been discussed above. While in the stoichiometric supercell 4 manganese atoms are available whose moments are aligned parallel (spin-up) the net number of spin-up Mn atoms decreases linear as more manganese atoms are added to the supercell because the spins of these additional atoms are aligned antiferromagnetically. The linear increase of the spin-down Mn atoms that goes hand in hand with the reduction of the magnetic moment is also plotted in Fig. 5.4 (b). It should be pointed out that the shape of Fig. 5.4 (b) is very similar to the behaviour of the structural phase transformation temperature as a function of e/a for the alloy series Ni-Mn-Z ($Z =$ Ga, In, Sn, Sb), when plotted within one graph (as in Ref. [171]). This already gives a clue that the change of T_M is related to the change of the magnetic properties that appear when changing the valence electron concentration.

Fig 5.4 (a) also contains results for a composition of Ni-Mn-Ga with Ga excess, namely $Ni_2Mn_{0.75}Ga_{1.25}$. As the magnetic moment in Ni_2MnGa is mainly contributed by the Mn moments it is clear that the total magnetization is reduced if Mn atoms are removed from the stoichiometric composition which has a ferromagnetic alignment of the manganese spins. This explains the different slopes of the Slater-Pauling curve. At the same time the crossover from ferro- to antiferromagnetism that takes place at the stoichoimetric composition clearly is visible. The results for Ni-Mn-Ga match previously published theoretical results by Enkovaara *et al.* [172]. In addition to the results for stoichiometric and off-stoichiometric compositions of Ni-Mn-Z Fig. 5.4 also contains results for the binary alloy NiMn which is obtained when substituting all Z atoms by Mn atoms. The results for this antiferromagnet fit well with the other results. Further properties of NiMn are discussed in detail in section 5.5.

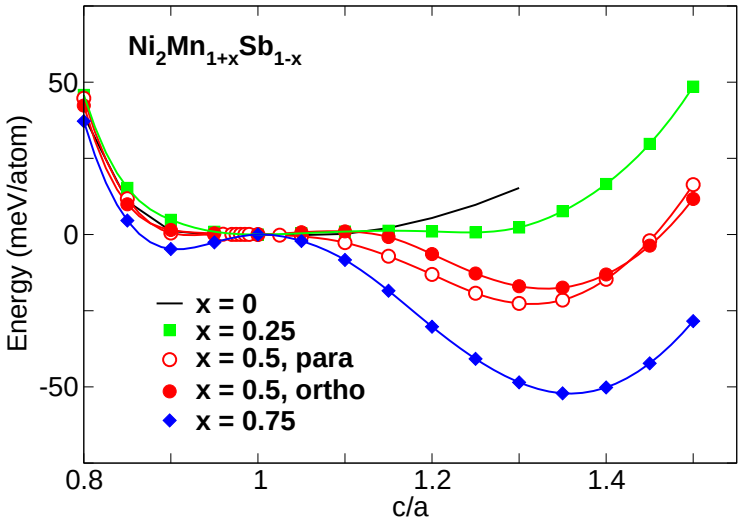

Figure 5.5: Total energy E as a function of tetragonality (c/a) for different compositions of Ni-Mn-Sb. The data points for the stoichiometric composition have been taken from Ref. [3]. Figure taken from Ref. [135].

5.4 Determination of phase transformation temperatures

The determination of the preferred magnetic alignment within the supercell of the considered composition allows to calculate the ground state lattice constant of the respective cubic structures. Once the lattice constant and the magnetic order of the austenite structure ($c/a = 1$) are known, the preference of a martensitic structure can be investigated by applying a volume-conserving tetragonal distortion on the supercell. In particular, the ground state energy E is calculated for several values of c/a, which allows to obtain an energy profile along the Bain path in analogy to Fig. 4.6 (a).

It turns out that for all alloy systems Ni-Mn-Z ($Z =$ Ga, In, Sn, Sb) tetragonal structures become preferred, as the valence electron concentration is increased by adding Mn in favour of Z to the system. This is in agreement with results obtained by Büsgen *et al.* for Ni-Mn-Al [173]. For the case of Ni-Mn-Sb this behaviour is shown in Fig. 5.5, where it can be clearly seen that for Mn-rich compositions a minimum of the total energy evolves at $c/a > 1$ while the stoichiometric composition does not reveal such a pronounced minimum for a tetragonal structure. The two different curves that are plotted in Fig. 5.5 for the composition $Ni_2Mn_{1.5}Sb_{0.5}$ (denoted as "para" and "ortho") originate from the fact that two crystallographic inequivalent directions appear in the supercell due to the limited size of the supercell for this specific composition. This special situation becomes more trivial when looking at Fig. 5.1 (c), which shows that one atomic layer withing the supercell completely consists of Mn atoms at the respective composition. The tetragonal distortion can now be applied parallel or orthogonal to this layer, which explains the two different curves for the respective composition in Fig.

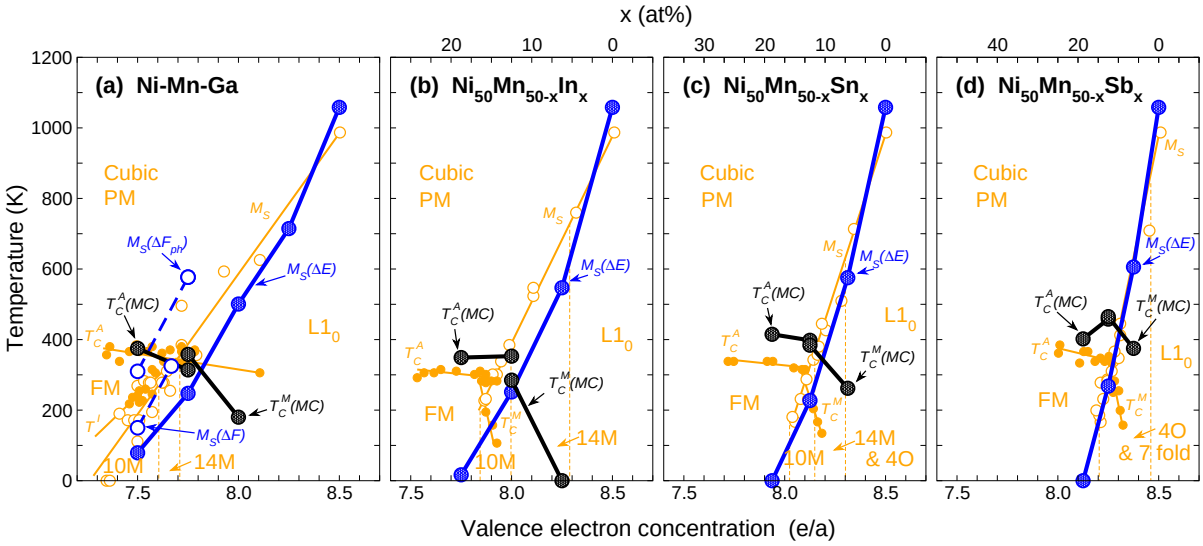

Figure 5.6: Theoretical phase diagram of Ni-Mn-Z. Figure taken from Ref. [175].

5.5. The situation is different for the other off-stoichiometric compositions where such atomic layers, which completely consists of Mn atoms, either do not appear at all or appear within all three planes that are defined by the cartesian unit vectors. It should be noted that the $E(c/a)$-curves which have been obtained for the Ni-Mn-Sn system agree well with previously published first-principles results by Ye *et al.* [174].

Since the transformation from the cubic to the tetragonal structure is accompanied by a volume change in certain alloys [3], volume changes were also considered in the calculation of the structural energy differences between the $L2_1$- and $L1_0$-structure. Therefore, after determining the position of the minima in the $E(c/a)$-curves, the ground state volumes for the corresponding c/a-ratios were calculated.

Once the total energy of the ground state volume of the cubic structure and the tetragonal structure are known, the structural energy difference between these two structures can be calculated. For each composition, the tetragonal structure with the lowest energy was considered as the ground state. The so obtained structural energy differences per atom can be related to a temperature scale as described in equation (4.1). This allows to establish the theoretical phase diagram of the Ni-Mn-Z alloy series, which is plotted in Fig. 5.6. While the yellow parts of the phase diagram refer to experimental measurements (open circles denote values of M_S, whereas closed circles denote values of T_C), the filled blue circles denote the theoretical values of M_S (T_M), which have been obtained using the method that has been described above. The open blue circles that are plotted within the phase diagram of Ni-Mn-Ga also denote the theoretically predicted martensitic transformation temperatures. However, in this case M_S has been obtained by using two different methods. While the values denoted as $M_S(\Delta F_{ph})$ have been obtained using the harmonic approximation the values denoted as $M_S(\Delta F)$ have been

obtained by Uijttewaal *et al.* taking into account also magnetic excitations using experimental magnetization curves and the quasiharmonic approximation [119, 176]. The filled black circles refer to Monte Carlo calculations of the critical magnetic temperature of the austenite (T_C^A) and martensite (T_C^M) structure by A. Dannenberg [177].

5.4.1 Discussion of the results

Although the calculation of transformation temperatures based on structural energy differences as described in equation (4.1) neglects magnetic excitations as well as the lattice entropy, the obtained results are in good qualitative agreement with the measured transformation temperatures. This is not only true for the linear behaviour of T_M, but also for the slope of the $T_M(e/a)$-curve, which increases as the mass of the Z atom increases. In case of Ni-Mn-Sn and Ni-Mn-Sb the theoretical and experimental transformation temperatures even agree quantitatively. The harmonic approximation, which was discussed in section 4.2 clearly overestimates the transformation temperatures, as depicted in Fig. 5.6 (a). However, even in this case the trend with e/a, namely the slope of the $T_M(e/a)$-curve, is in qualitative agreement with the experiment. Fig. 5.6 (a) also shows, that the results from Uijttewaal *et al.* yield a nearly perfect qualitative, but also quantitative agreement between theory and experiment. However, it should be mentioned in this context that calculations using the quasiharmonic approximation and taking into account the magnetic excitations using experimentally obtained magnetization curves are not only far more demanding than the estimation of the transformation temperatures based on structural energy differences between the austenite and the martensite structure, but also rely on additional experimental data and are therefore, in a sense, not truly *ab initio*.

Although the estimation of T_M based on the energy difference between the $L2_1$- and $L1_0$-structure is able to correctly describe the trends that appear in the alloy series Ni-Mn-Z, there still appear more or less significant deviations from the experimentally obtained values. There are several possible reasons that can be considered to be responsible for these deviations. At first the calculations consider perfectly periodic systems, whereas in an experimental sample lattice defects or impurities might appear. At the same time the treatment of disorder in the calculation of off-stoichiometric compositions might also influence the results. Unlike the situation in an experimental sample, where the excess atoms are expected to be randomly distributed over the sublattice that is affected by the atom substitution the excess atoms are assumed to always occupy the same lattice sites in a periodic manner when using the supercell approach. Another reason for the discrepancy between theory and experiment might be caused by atomic relaxations that appear in the supercell at off-stoichiometric compositions. While no forces appear in the stoichiometric composition and the binary NiMn alloy, when the atoms are placed at their ideal lattice positions, the situation changes as soon as one of the sublattices of the Heusler structure is not occupied solely by one type of atoms. Since it it known that local lattice distortions can significantly affect the shape of the binding energy surfaces in the magnetic shape memory alloy Fe-Pd, such distortions need to be taken care of

Table 5.2: Effect of atomic relaxations on the transformation temperature for compositions containing small amounts and large amounts of Mn. Δ describes the relative change of T_{M} between the value that has been derived considering volume changes and the value that also takes into account atomic relaxations during the tetragonal transformation. In the former case, the atomic positions are fixed to the ideal lattice sites. The composition $Ni_2Mn_{1.25}Sn_{0.75}$ is not listed as the $L2_1$-structure is energetically favoured over the $L1_0$-structure for both types of relaxations.

System	T_{M}(K) $volume-relaxation$	T_{M}(K) $full-relaxation$	Δ
$Ni_2Mn_{1.25}Ga_{0.75}$	247.6	238.6	3.6%
$Ni_2Mn_{1.75}Ga_{0.25}$	714.6	693.7	2.9%
$Ni_2Mn_{1.25}In_{0.75}$	16.7	17.8	6.6%
$Ni_2Mn_{1.75}In_{0.25}$	546.9	546.5	0.1%
$Ni_2Mn_{1.75}Sn_{0.25}$	575.4	592	2.9%
$Ni_2Mn_{1.25}Sb_{0.75}$	0	44.6	-
$Ni_2Mn_{1.75}Sb_{0.25}$	605.7	719.4	18.8%

also in the Ni-Mn-Z alloys [178]. Hence, the effect of relaxations has been studied using a Mn-rich composition (Ni_8Mn_7Z supercell) and a composition with only small amounts of excess Mn ($Ni_8Mn_5Z_3$ supercell). For all systems the relaxed atomic positions of the respective compositions were obtained using a conjugate gradient algorithm [179]. It turns out that the effect of relaxations in both cases is small and does not change the theoretically obtained transformation temperatures significantly. An exceptional case is Ni-Mn-Sb where the absolute changes of T_{M} caused by the relaxations become rather large. However, as the slope of the $T_{\mathrm{M}}(e/a)$-curve has the highest value for the alloy system containing Sb, this behaviour is somewhat expected. Table 5.2 relates the transformation temperatures obtained by atomic relaxation to the transformation temperatures that have been used to derive the phase diagram which is plotted in Fig. 5.6.

When considering atomic relaxations it turns out that Ni-Mn-In behaves different from the other alloy systems. While the energy difference between the antiferromagnetic austenite and martensite structures does not change significantly when the atoms are relaxed (see table 5.2) the energy difference between the ferromagnetic and antiferromagnetic orientation of manganese moments changes significantly and even changes its sign for all off-stoichiometric compositions of Ni-Mn-In that have been considered here. This means that the ferromagnetic structure with $c/a = 1$ becomes energetically favoured over the antiferromagnetic structure. However, as the energy difference between the two structures is less than 11 meV/atom for all considered compositions an antiferromagnetic tetragonal ground state still is expected for

compositions where at least 50% of the In atoms have been replaced by Mn as the antiferromagnetic tetragonal structure still is lower in energy than the ferromagnetic cubic structure for these compositions. The reasons for this somewhat unexpected behaviour of Ni-Mn-In can be manifold. The preference of ferromagnetic structures in the cubic state might for example originate from the already mentioned limited description of disorder within the supercell approach. It can however also be related to the fact that the valence electron concentration of the off-stoichiometric compositions of Ni-Mn-In are smaller than for Ni-Mn-Z ($Z =$ Sn, Sb) and amount to the same values as in the case of Ni-Mn-Ga which has however a reduced volume. Hence, the larger volume compared to Ni-Mn-Ga in connection with the smaller e/a ratio compared to Ni-Mn-Z ($Z =$ Sn, Sb) could lead to a stabilization of the ferromagnetic phase. The experimental Slater-Pauling curve which is contained in Ref. [170] indeed shows that an increase of the magnetic moment is observed for Ni-Mn-In up to some point which corresponds to an Mn-rich composition.

From another point of view the treatment of the magnetic moments in the calculations also gives rise to possible issues that could influence the results. In the calculations of the structural energy differences only collinear alignments of the moments could be considered. However, Kallmayer *et al.* pointed out that a more complex description of magnetism than the linear alignment of constant spins is needed to explain their results which have been obtained by investigating Ni-Mn-Ga films using x-ray absorbtion spectroscopy (XAS) and x-ray circular magnetic dichroism (XMCD) [180]. From a theoretical point of view such a description taking into account non-collinear alignments of magnetic moments so far requires huge computational effort and therefore is not feasible for the complete range of compositions that have been considered here for the near future.

5.5 The binary NiMn alloy

The end of the alloy series $Ni_2Mn_{1+x}Z_{1-x}$ ($x = 1$) corresponds to the binary NiMn alloy where all Z atoms have been replaced by Mn. It turns out that for this composition the antiferromagnetic order that was found for the Mn-rich compositions of Ni-Mn-Z is not the ground state for the cubic bcc-phase. In fact, Fig. 5.7 shows that a purely ferromagnetic state has the lowest energy at $c/a = 1$. Nevertheless, as the ferromagnetic order does not reveal a second minimum, the same type of antiferromagnetic order as for the Mn-rich compositions was considered in the evaluation of T_M of NiMn. In this type of structure each Mn atom is aligned antiferromagnetically with respect to the 6 Mn atoms which are the nearest Mn neighbours in the cubic structure with $c/a = 1$. The corresponding $E(c/a)$-curve is denoted as AFM II in Fig. 5.7. Experimental results, however, suggest a different type of antiferromagnetic order [181, 182]. In this structure, the Mn atoms that become nearest neighbours are aligned antiferromagnetically. However, as the crystal structure is tetragonal, the number of nearest neighbours is reduced, giving rise to an additional type of next nearest-neighbours, which are

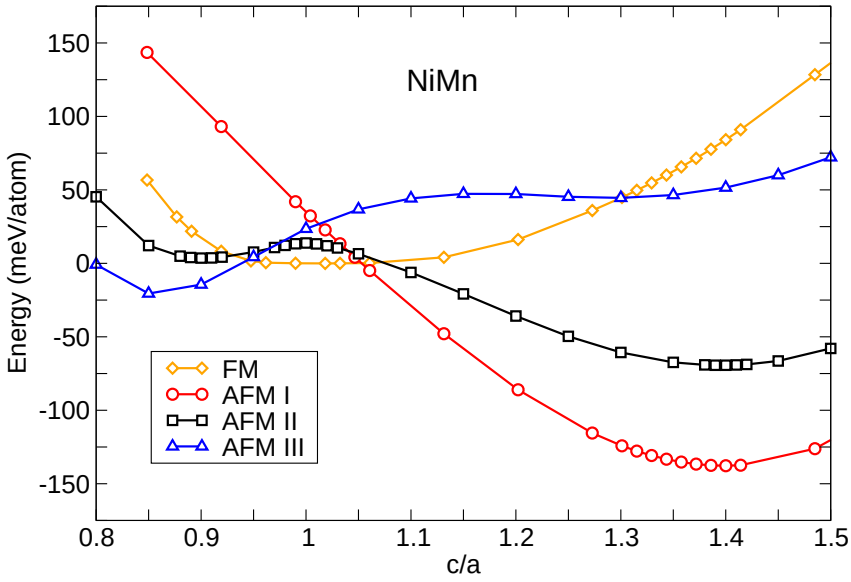

Figure 5.7: Total energy as a function of c/a for different alignments of the magnetic spins of the binary NiMn alloy. The orange curve denoted as FM corresponds to a ferromagnetic alignment of the spins of the Mn atoms whereas the other curves are associated with different types of antiferromagnetic alignments of the magnetic moments of the Mn atoms (see text). The red curve denoted as AFM I denotes the ground state, which has been reported by Kasper and Kouvel [181].

assumed to be aligned ferromagnetic in the ground state structure reported by Kasper and Kouvel [181]. Fig. 5.7 shows that this structure, denoted as AFM I, indeed yields the lowest energy. Besides the discussed ferro- and antiferromagnetic alignments of Mn moments a third antiferromagnetic alignment of the Mn moments in NiMn which is denoted as AFM III is also plotted in Fig. 5.7. In this type of structure the moments of Mn atoms which are located in the same (110) plane are aligned ferromagnetically. However, this structure is energetically only favoured for small values of c/a.

The martensitic transformation temperature that is obtained from the energy difference between the two structures assocotiated with austenite and martensite structure of the magnetic ordering AFM II (1058.1 K) is found to be in quantitative agreement with experimental results (965.2 K) [182]. Moreover, the obtained results for NiMn are in good qualitative agreement with previous *ab initio* results by Godlevsky and Rabe [183]. The investigation of the binary NiMn alloy nicely shows the importance of antiferromagnetism in the formation of martensitic tendencies. While the ferromagnetic structure does not reveal a second minimum under a variation of c/a two of the considered antiferromagnetic structures reveal two energy minima along the Bain path.

5.6 The effect of compositional changes on the electronic structure

So far, the supercell approach has been used to calculate structural properties of off-stoichiometric compositions of Ni-Mn-Z in this chapter. It has turned out that a simple approach, which relates the structural energy differences between the $L2_1$- and $L1_0$-structure to the phase transformation temperatures of the structural transition yields good agreement with experimental results. In the following, the origin of the martensitic transformation and the linear behaviour of T_M with e/a will be taken care of by investigating the effect of atomic substitutions on the electronic structure. The discussion will focus in particular on the band Jahn-Teller effect, the influence of the valence electron concentration on the tetragonal transformation and magnetic properties as well as the role of Fermi surface nesting in the off-stoichiometric compositions.

5.6.1 Appearance of the band Jahn-Teller effect

As was already mentioned in section 3.2, the martensitic transformation in Ni_2MnGa is accompanied by the appearance of the band Jahn-Teller effect [101, 64]. The calculations for the off-stoichiometric compositions show that the band Jahn-Teller effect also can be observed for the Mn-rich compositions of Ni-Mn-Z (Z =Ga, In, Sn, Sb). Nevertheless, the appearance of the band Jahn-Teller effect is far less pronounced for these compositions compared to stoichiometric Ni_2MnGa. This relationship is depicted in Fig. 5.8, which contains a density plot of the electronic density of states of the minority spin-channel as a function of the energy and c/a for (a) Ni_2MnGa and (b) $Ni_2Mn_{1.75}Ga_{0.25}$. For the case of Ni_2MnGa a clearly visible peak can be recognized for $c/a = 1$, which is situated about 0.2 eV below the Fermi level. For values of c/a which deviate from the cubic case with $c/a = 1$ this peak splits up and parts of it are shifted above E_F. For the Mn-rich composition $Ni_2Mn_{1.75}Ga_{0.25}$ which is shown in Fig. 5.8 (b), the situation is a little bit different. The peak that is situated below the Fermi level at $c/a = 1$ does not split up when applying a tetragonal distortion, but is just shifted above E_F. At the same time the peak is also not as pronounced as in Ni_2MnGa and situated more closely to the Fermi level in the cubic case, while becoming smeared out when being shifted above E_F. The latter behaviour is not found for Ni_2MnGa and marks another difference between the two compositions. The fact that the peak position at $c/a = 1$ is shifted to E_F with increasing Mn-content is in agreement with experimental and theoretical results by Ye *et al.* for Ni-Mn-Sn [174]. However, in this case the size of the peak also decreases with increasing valence electron concentration. Hence, as the evidence of a band Jahn-Teller effect is smaller for the Mn-rich composition, which at the same time show larger energy differences between $L2_1$- and $L1_0$-structure compared to Ni_2MnGa, these energy changes cannot be motivated by the band Jahn-Teller effect. Instead, the band Jahn-Teller effect should only be regarded as an accompanying feature of the martensitic transformation, but not as the dominant reason for the increase of T_M with e/a.

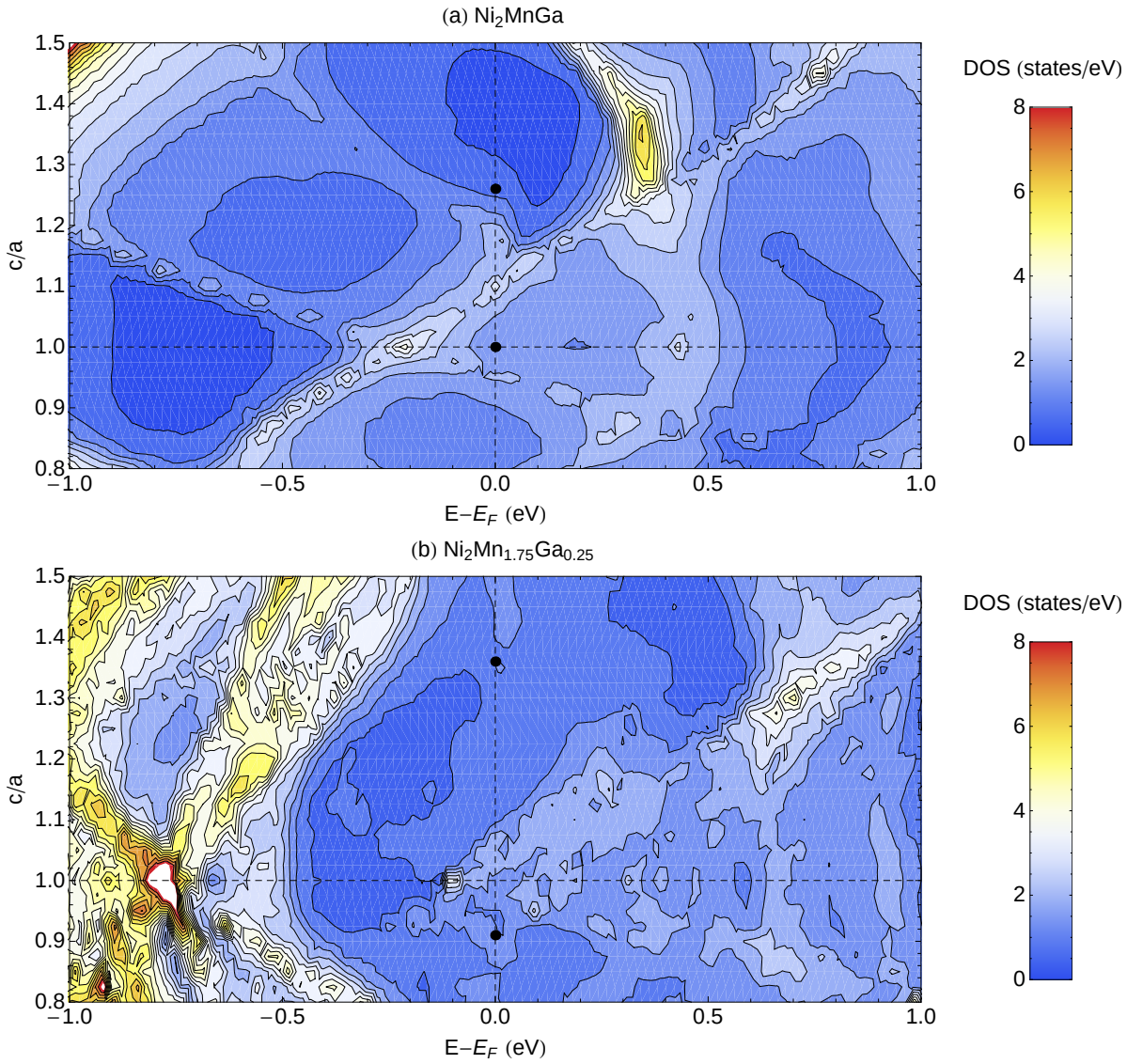

Figure 5.8: Electronic density of states (DOS) of (a) Ni_2MnGa and (b) $Ni_2Mn_{1.75}Ga_{0.25}$ (Ni_8Mn_7Ga supercell) for different values of c/a. Here, only the contribution of the minory spin-channel to the DOS is plotted. The black dots which are situated at $E_F = 0$ mark the positions of the total energy minima in the $E(c/a)$-curves of the respective compositions. In the white region in (b) the values of the density of states lie outside the plot range. Figure adapted from Ref. [135].

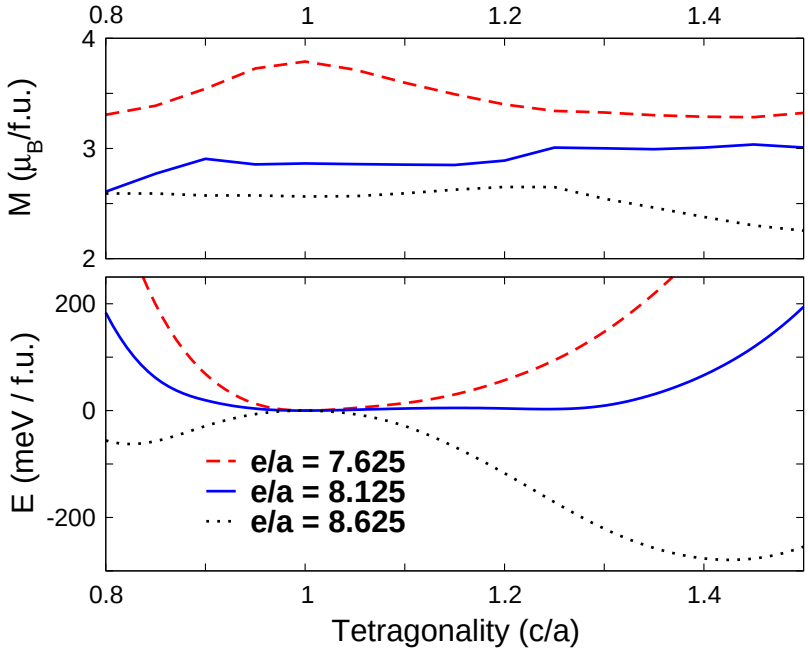

Figure 5.9: Behaviour of the total energy E and the total magnetization M of $Ni_2Mn_{1.25}Sb_{0.75}$ as a function of c/a under a variation of e/a. The different e/a ratios have been obtained by changing the number of electrons in the density functional theory calculation. The volume was kept constant during the calculations and was fixed to the ground state volume of the cubic structure without additional electrons. Figure adapted from Ref. [135].

5.6.2 The influence of e/a on the tetragonal transformation

As the transformation temperature of Ni-Mn-Z (Z =Ga, In, Sn, Sb) increases linearly with the valence electron concentration, it seems nearby to investigate in how far the structural changes are directly related to changes of e/a. In density functional theory this can be done by changing the number of valence electrons that are being considered in a calculation. In this case, the charge difference between the core charge and the electron charge is compensated by a homogenous background charge that is imposed in order to keep the system electrically neutral. It turns out that the variation of the number of electrons for a fixed concentration indeed shows the same characteristic trend as is obtained when changing the e/a ratio by substituting atoms. In particular, tetragonal distortions become favoured, as the valence electron concentration e/a is increased. Fig. 5.9 demonstrates this finding for the case of the Mn-rich composition $Ni_2Mn_{1.25}Sb_{0.75}$. The natural valence electron concentration of this composition is $e/a = 8.125$. At this e/a ratio the system reveals a very flat energy landscape where the $L2_1$- and $L1_0$-structure are almost degenerate. If the number of electrons that are treated within the calculation is increased to $e/a = 8.625$ the $L1_0$-structure clearly becomes

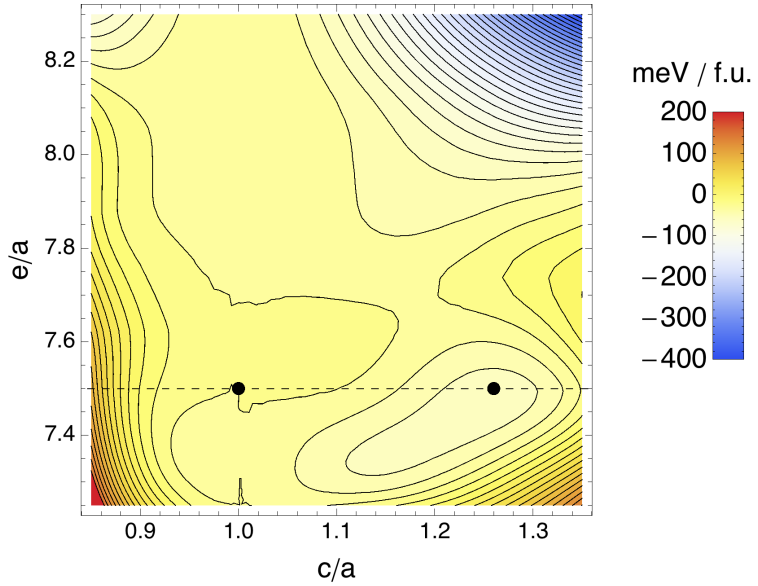

Figure 5.10: Energy difference $E(c/a, e/a) - E(1.0, e/a)$ as a function of c/a and e/a for Ni_2MnGa. The calculations were performed at constant volume for the ground state lattice constant of the $L2_1$-structure ($a_0 = 5.81$ Å).

favoured at a $c/a \approx 1.43$. On the other hand, a reduction of the number of electrons to $e/a = 7.625$ leads to a stabilization of the $L2_1$-structure which means that the flatness of the energy landscape vanishes in favour of a minimum at $c/a = 1$. Both findings are in agreement with the results obtained in section 5.4 (note the similarities between Fig. 5.9 and Fig. 5.5). The plot of the total magnetization M which is included in Fig. 5.9 also gives a hint that it is indeed antiferromagnetism that is responsible for the tetragonal transformation. In particular, the magnetization decreases as the number of electrons is increased in accordance with the Slater-Pauling curve presented in Fig. 5.4.

It has to be mentioned at this point that a recent first-principles investigation of the influence of e/a on the $E(c/a)$-curves in case of Ni_2MnGa predicts that the increase of e/a leads to a stabilization of the cubic structure [109]. These results seem to be in disagreement with the results that are presented here. However, Fig. 5.10 shows that for e/a ratios which are larger than 8.0 a similar behaviour as for Ni-Mn-Sb is observed for Ni-Mn-Ga. Ni_2MnGa is the only compound of Ni-Mn-Z which undergoes a martensitic transformation already in stoichiometric composition. This observation is indicated by the shallow minimum at $c/a = 1.26$ for the valence electron concentration of the stoichiometric composition ($e/a = 7.5$). While this minimum vanishes at $e/a \approx 7.65$ even more pronounced minima at $c/a < 1$ and $c/a > 1$ appear for $e/a > 8$.

5.6.3 Composition-dependence of the Fermi surface

As was already pointed out in section 3.2 the appearance of the martensitic transformation in Ni_2MnGa is often related to nesting effects of the Fermi surface [95, 92]. This raises the question whether such signs of Fermi surface nesting also appear in Ni-Mn-Z ($Z =$ Ga, In, Sn, Sb) in general, especially in the off-stoichiometric Mn-rich alloys. In the following two different methods to calculate the Fermi surface of off-stoichiometric alloys will be presented. The first method makes use of the rigid band approach which assumes that a change of the valence electron concentration does not influence the band structure itself but only the band filling, i.e. the position of the Fermi level. This means that the calculation of the band structure of the stoichiometric composition gives rise to the Fermi surfaces of different e/a ratios by shifting the Fermi energy E_F. The change of e/a that is related with the shift can be obtained by an integration over the electronic density of states $D(E)$ defined by

$$\Delta e/a(E) = \frac{1}{4}\int_{E_\mathrm{F}}^{E} D(E')dE' \tag{5.1}$$

where the prefactor $\frac{1}{4}$ arises from the fact that $D(E)$ refers to a formula unit of the stoichiometric composition which contains four atoms. Using equation (5.1) the Fermi surfaces for different energies E can be related to the e/a ratio of these energies which is obtained by the sum of the e/a ratio of the respective stoichiometric composition and $\Delta e/a(E)$. Fig. 5.11 contains the Fermi surfaces of Ni-Mn-Z ($Z =$ Ga, In, Sn, Sb) for different e/a ratios that have been obtained using the described approach. For the calculations a k-point grid consisting of $31 \times 31 \times 31$ points was used. It is eye-catching that the four different alloy systems reveal rather similar Fermi surfaces at the same e/a ratios. This applies especially for the case of $e/a = 7.5$ which corresponds to stoichiometric Ni_2MnGa and Ni_2MnIn. The similarities can be explained by the fact that the stoichiometric compositions of the four different materials only differ in the number of p-type valence electrons. As this type of electrons is not that much present as the d-electrons near the Fermi level, the density of states and thus also the Fermi surfaces are not influenced significantly by the substitution of Ga by In, Sn or Sb. However, there also appear some differences between the Fermi surfaces of the different alloy systems for certain e/a ratios. For example the band which is marked blue only appears in the Fermi surfaces of Ni_2MnGa and Ni_2Min at $e/a = 7.75$ and the appearance of the orange band within the Fermi surface of Ni_2MnGa clearly is different compared to the other Fermi surfaces at $e/a = 8$.

The Fermi surfaces obtained using the rigid band approach seem to be reasonable in so far, as the basic shape properties are obtained independently from the material and only depend on e/a. Therefore, the rigid band approach in principle can be used to obtain the Fermi surfaces of off-stoichiometric compositions. However, the approach misses one important feature which is present in the off-stoichiometric compositions of Ni-Mn-Z, namely the antiferromagnetic interactions. As a band structure calculated for the stoichiometric composition, where no

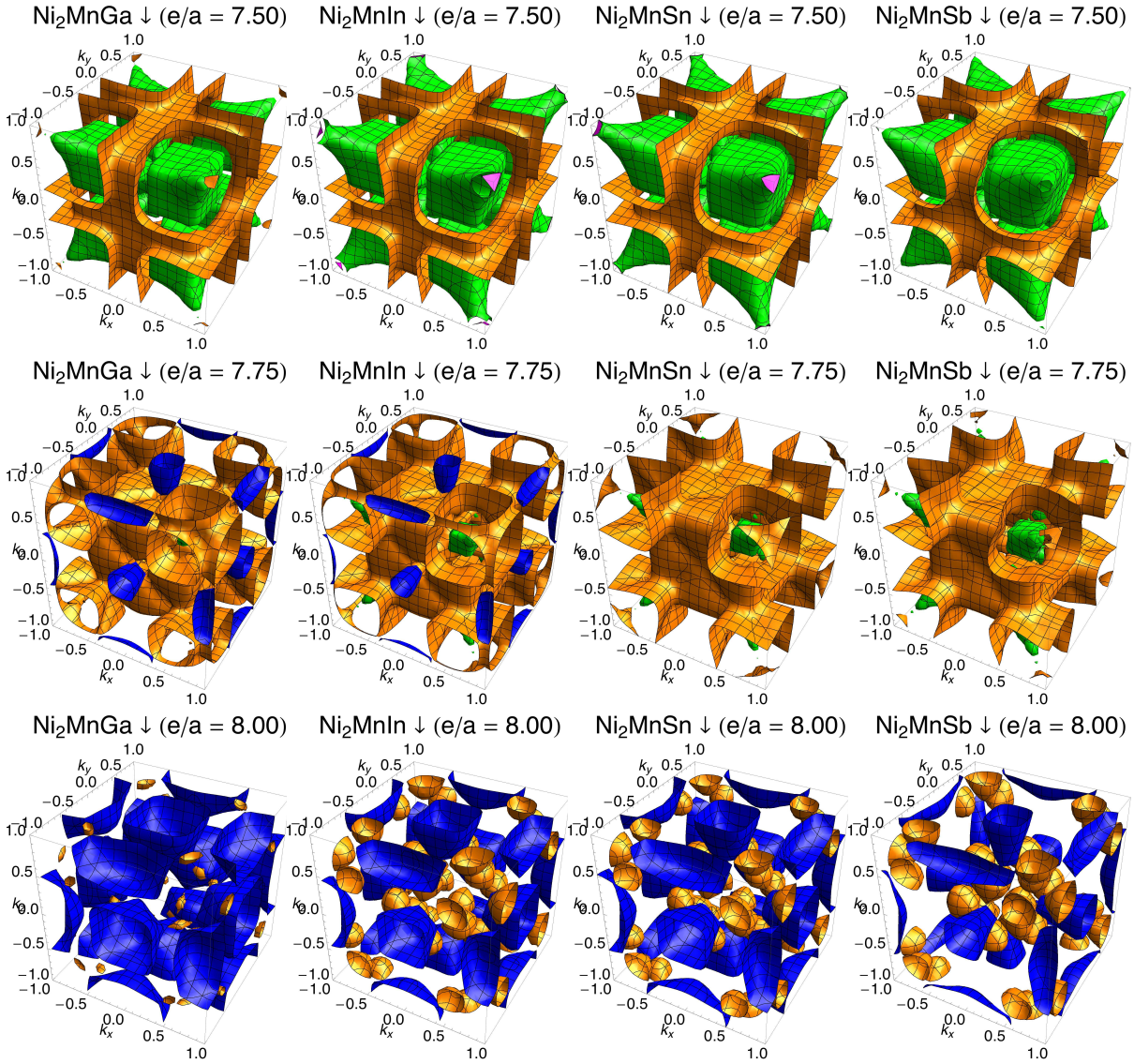

Figure 5.11: Fermi surfaces of the minority spin-channel for different e/a values of Ni_2MnGa, Ni_2MnIn, Ni_2MnSn and Ni_2MnSb within the rigid band approach. Here, different colors are related to different bands and the Γ-point is situated in the center and at each corner of the surrounding boxes. Adapted from Refs. [92, 135].

antiferromagnetic tendencies appear, is used to obtain the Fermi surfaces for different e/a ratios, these Fermi surfaces do not contain effects that are caused by the substituted Mn atoms on the Z sites.

A possible way to study the influence of antiferromagnetic interactions on the Fermi surfaces is the calculation of the Fermi surfaces of the off-stoichiometric supercells with Mn excess. While in principle this method should give feasible results, a problem arises from the fact that the volume of the supercells is larger than the volume of the primitive cell of the stoichiometric compositions. This means that at the same time the Brillouin zone that belongs to the supercells is smaller than the Brillouin zone that corresponds to the cell which consists of only four atoms. The reduced size of the Brillouin zone goes hand in hand with a folding of the band structure and therefore also with a folding of the Fermi surface sheets. This folding can be seen when looking at the Fermi surface of a supercell with the same atomic concentration as the stoichiometric composition. The Fermi surface of this supercell, namely $Ni_8Mn_4Ga_4$, is plotted in Fig. 5.12 (a). The green cubes that appear in the primitive cell are now folded into each other, as well as the flat orange sheets. Fig. 5.12 (a) already illustrates the problems that arise from the folding of the Fermi surfaces as it is not possible to identify all nesting properties that are present in the primitive cell within the supercell.

Nevertheless, the investigation of the off-stoichiometric Fermi surfaces of Ni-Mn-Z allows to look for certain trends that are introduced when increasing the Mn content. Fig. 5.12 contains the results for the Ni-Mn-Ga system. In contrast to the primitive cells, the Fermi surfaces of the supercells have been calculated using a k-point grid containing $21 \times 21 \times 21$ points. For off-stoichiometric compositions the supercells containing 16 atoms are already the primitive cells which means that the Fermi surfaces cannot be folded back in case of these compositions. The symmetry-breaking that is related with this property is for example expressed in the splitting of the green bands (a) into four bands with different shapes (b-d) in Fig. 5.12. This splitting leads to a reduction of the parallel sheets of the Fermi surface which means that the nesting effects are reduced. This means, that the obtained results suggest that the increased martensitic transformation temperatures that appear in Mn-rich compositions cannot be related to Fermi surface nesting. Thus, nesting effects of the Fermi surface can only be regarded as an accompanying feature of the martensitic transformation, in a similar manner as the band Jahn-Teller effect. It should be reminded that due to the fact that the binary NiMn is an antiferromagnet the addition of Mn leads to an adjustment of the spin-up and spin-down Fermi surface until both quantities become equal in case of the binary alloy.

5.7 Conclusion

Within this chapter the results of the calculations for a broad range of compositions of the alloy series Ni-Mn-Z (Z= Ga, In, Sn, Sb) have been presented. It turns out that the experimentally known properties of this alloy series can be reproduced using *ab initio* methods. In particular, a

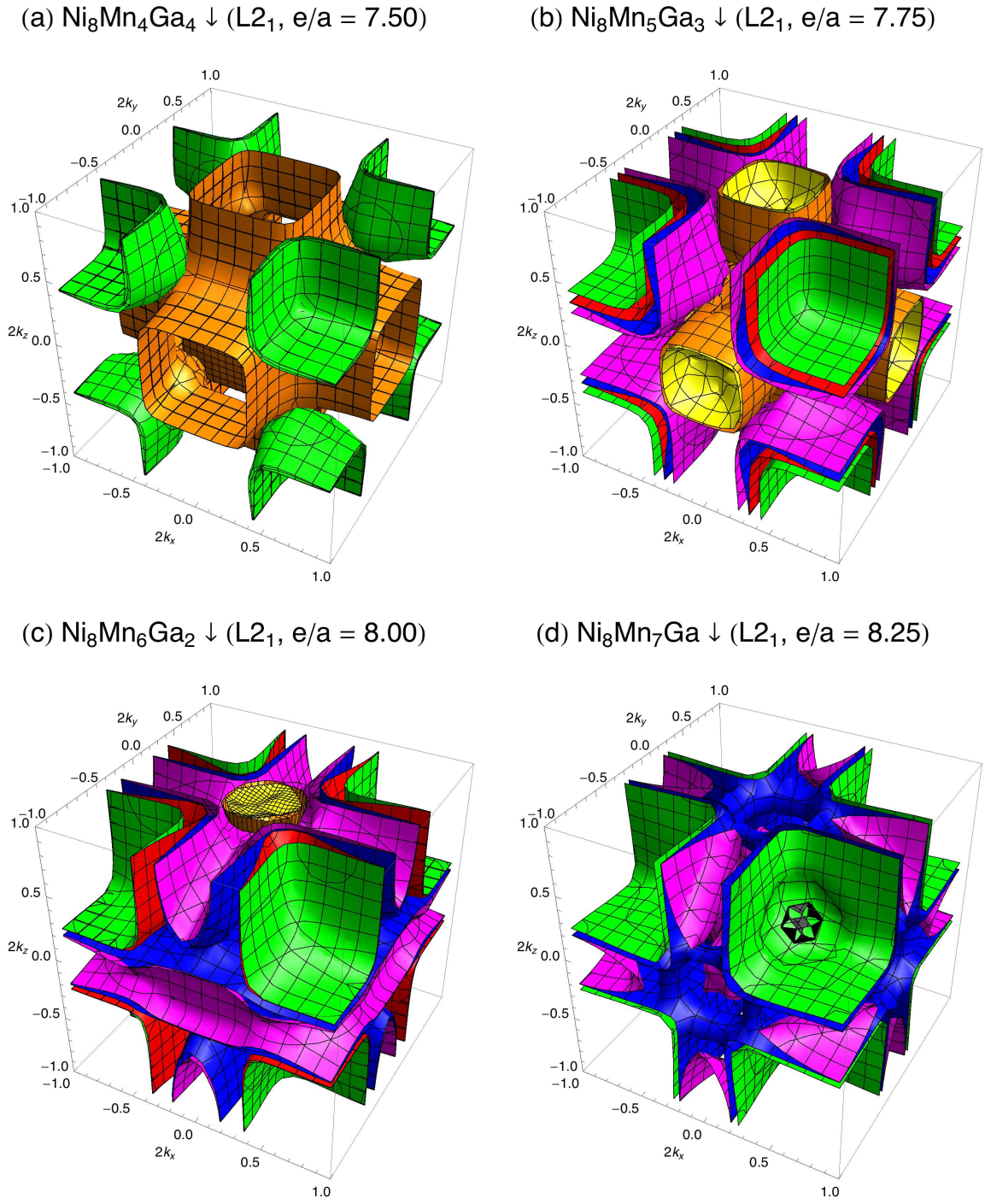

Figure 5.12: Fermi surfaces of the stoichiometric and off-stoichiometric compositions (a) $Ni_8Mn_4Ga_4$, (b) $Ni_8Mn_5Ga_3$, (c) $Ni_8Mn_6Ga_2$, and (d) Ni_8Mn_7Ga. The Γ-point is situated at the center of the surrounding boxes. Adapted from Ref. [135].

linear increase of the martensitic transformation temperature with increasing valence electron concentration e/a is obtained. The first-principles calculations allow to study the effect of the martensitic transformation in detail. The investigation of the electronic structure reveals that the addition of Mn on the one hand increases the martensitic transformation temperature but on the other hand does not give evidence that the increased energy differences between austenite and martensite structure are related to the band Jahn-Teller effect or the nesting effects which can be observed in the Fermi surface. Although both effects are also present in the off-stoichiometric compositions which have been studied here it is reasonable to assume that the increase of T_{M} with increasing e/a cannot be related to these effects. On the contrary, the so far obtained results show clear evidence that the antiferromagnetic alignment of magnetic moments which is preferred by the additional Mn atoms on the Z site is responsible for the increase of T_{M}. In particular, the linear increase of the transformation temperature can be directly related to the linear decrease of the magnetization with e/a. These results are in agreement with previous findings from Enkovaara *et al.* who showed that the martensite structure in Mn-doped Ni_2MnGa is stabilized by the antiferromagnetic interactions that are present in the material [172]. The calculations of the phase diagrams show that this behaviour is found for the whole alloy series Ni-Mn-Z (Z= Ga, In, Sn, Sb).

It is remarkable that for Ni-Mn-Sn and Ni-Mn-Sb a nearly quantitative agreement between the calculated and measured transformation temperatures is found while deviations between these two values appear in case of Ni-Mn-Ga and Ni-Mn-In. A possible explanation is the occurence of Fermi surface nesting in the stoichiometric case of the latter compounds and especially in the case of Ni_2MnGa. For the case of Ni-Mn-In it turns out that the preference for antiferromagnetic alignments is not so strong as it is the case in the Mn-rich compositions of the other investigated alloys. This may be explained by the reduced e/a ratio for a given amount of excess Mn compared to Ni-Mn-Sn and Ni-Mn-Sb and the enlarged volume compared to the Ni-Mn-Ga system. The reduced preference for antiferromagnetic alignments in Ni-Mn-In and the effects devoted to Fermi surface nesting in Ni_2MnGa are however not considered in the calculation of the energy difference between the austenite and martensite structure which might explain the deviations from the experimental results.

For the compositions of Ni-Mn-Ga with Ni excess it is known that the increase of the martensitic transformation temperature goes hand in hand with a reduction of the lattice constant [184, 185]. In this context it was considered that the change of the structural transformation temperature is directly related to the change of the volume. This is interesting as Ni_2MnGa has the smallest lattice constant and at the same time is the only martensitically transforming system of the four stoichiometric compounds that have been considered here. In a systematic investigation of the lattice constants for several compositions of Ni-Mn-Z (Z = Ga, In, Sn, Sb) Planes *et al.* suggested a critical lattice constant of the cubic structure of $a_{\mathrm{c}} \approx 6\,\text{Å}$ as a threshold for the appearance of the martensitic transformation [105]. The results that are presented here are basically in agreement with this suggestion.

Chapter 6

The quaternary alloy system Ni-Pt-Mn-Z

In the last chapter the physical properties of the alloy series Ni-Mn-Z ($Z =$ Ga, In, Sn, Sb) have been studied in detail with special emphasis on the martensitic transformation that appears for certain compositions of this material class. It has been shown that the experimentally observed properties like the transformation temperature or the magnetic moment are basically also found when applying *ab initio* methods. However, the results of the first-principles calculations that have been undertaken so far in this thesis confirm that the investigated materials still face problems regarding their industrial relevance. This is mainly due to the fact that high structural transformation temperatures which are needed for industrial applications can only be achieved in Mn-rich samples which at the same time reveal rather smaller magnetic moments due to the antiferromagnetic alignments of spins that appear upon the addition of excess Mn. At the same time also the critical magnetic temperature T_{C} decreases with increasing Mn content. The opposite trends of T_{M} and T_{C} are still hindering the usage of the Ni-Mn-Z alloys in a variety of applications and restrict it to only a few reference applications. [1]

The aim of this chapter is to show that the *ab initio* methods which have been applied to an experimentally classified material in the last chapter can also be used to predict new materials which are expected to reveal better material properties with regard to the magnetic shape memory effect. In particular, the effect of the addition of platinum to Ni-Mn-Z ($Z =$ Ga, Sn) will be studied using *ab initio* methods. The investigation is motivated by the fact that certain compositions of Ni-Pt-Mn-Ga reveal characteristic features of ferromagnetic shape memory alloys [186]. In addition, Fe_3Pt which is an Fe-based compound consisting of platinum is also known to show magnetic shape memory behaviour [66, 187].

6.1 The influence of platinum addition in Ni-Mn-Ga

In the following the results of the substitution of Ni by Pt will be discussed. The idea behind this type of substitution is the fact that the valence electron concentration remains constant as Ni and Pt are situated in the same main group of the periodic table of the elements and therefore have the same number of valence electrons. As the band Jahn-Teller effect and Fermi surface nesting are most pronounced for the valence electron concentration of Ni_2MnGa ($e/a =$

[1] Although the Ni-Mn-Ga alloy faces additional issues like its brittleness and the problems that arise from sample preparation there are actually industrial devices available that are based upon this material (see www.adaptamat.com).

7.5) it is reasonable to assume that the isoelectronic substitution might retain these phenomena of the electronic structure while at the same time changing other physical properties of the system. Nevertheless it should be mentioned that although the number of valence electrons of Ni and Pt is the same the electronic configurations are different as Pt has one *d*-type valence electron more but one *s*-type valence electron less than Ni.

Several Heusler alloys based on Pt have been reported in the literature [188, 189]. Pt_2MnGa which is part of the $Ni_{2-x}Pt_xMnGa$ alloy series that will be discussed here was already mentioned in 1971 by Hames *et al.* [189]. In this context the compound was considered to be antiferromagnetic with $T_N = 75\,K$ (see also Ref. [190]). However, the density functional theory calculations using VASP, PAW pseudopotentials and the generalized gradient approximation (PBE) reveal that a ferromagnetic structure is energetically favoured over an antiferromagnetic structure. The latter one which is 26.1 meV/f.u. higher in energy than the ferromagnetic alignment correponds to a structure with a layerwise arrangement of the magnetic moments of the Mn atoms. The disagreement between the theoretical density functional theory calculations and the experimental observations suggests that either a ferromagnetic alignment or a complex antiferromagnetic alignment that is not commensurate with the used supercell is expected to be the ground state of Pt_2MnGa. In 2004, Pt_2MnGa but also $Pt_{0.4}Ni_{1.6}MnGa$ have been investigated with regard to the magnetic shape memory effect by Kishi *et al.* [186]. In this study a martensitic transformation of the materials into a tetragonal or orthorhombic structure was observed.

In the following, the influence of a partial and total substitution of Ni by Pt in Ni_2MnGa shall be discussed. The behaviour of the total energy as a function of tetragonality for several compositions of the alloy series $Ni_{2-x}Pt_xMnGa$ with $0 \leq x \leq 2$ is plotted in Fig. 6.1. It is clearly visible that the addition of platinum leads to an increase of the energy difference between the $L2_1$- and $L1_0$-structure which is already present in Ni_2MnGa at $c/a > 1$. A second observation that can be made is the onset of a second pronounced minimum at $c/a < 1$ with increasing amount of platinum. In the last chapter the structural energy difference between austenite ($c/a = 1$) and martensite ($c/a > 1$) structure that turned up in the $E(c/a)$-curve have been associated with the martensitic transformation temperatures of the respective compositions. As this simple approach yielded feasible results it seems likely to expect that the increased structural energy differences which appear upon the addition of platinum go hand in hand with an increase of the martensitic transformation temperature.

As the Pt atoms are larger than the Ni atoms the addition of platinum increases the ground state lattice constant of the system. In particular, the lattice constant changes from $a = 5.81\,Å$ in the case of Ni_2MnGa ($L2_1$-structure) to $a = 6.05\,Å$ for NiPtMnGa and $a = 6.23\,Å$ for Pt_2MnGa. Additionally the substitution also influences the magnetic properties of the alloy. The magnetic moment of Pt_2MnGa is $M = 4.14\,\mu_B/f.u.$ and therefore higher than in Ni_2MnGa ($M = 4.07\,\mu_B/f.u.$ [3]). The increase of the total magnetic moment can be explained by the increased volume which raises the moments of the Mn atoms up to $3.75\,\mu_B$ while at the

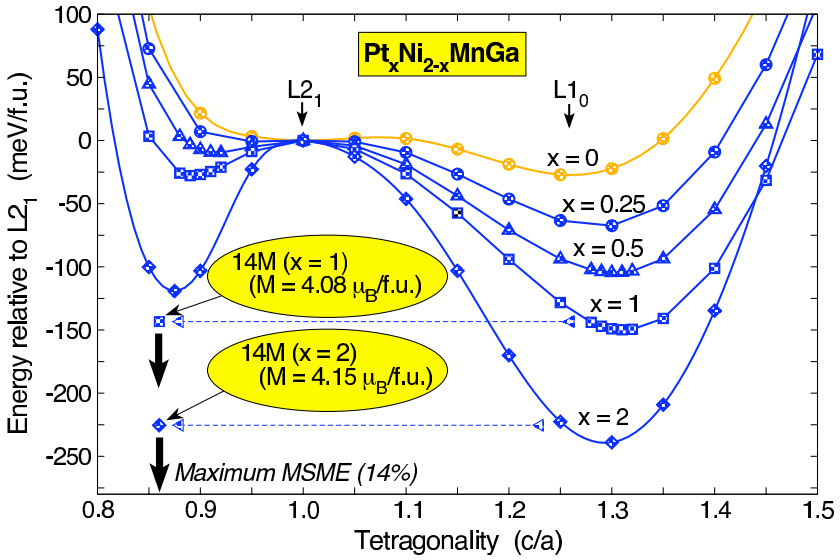

Figure 6.1: Total energy as a function of tetragonality c/a for the alloy series $Ni_{2-x}Pt_xMnGa$. The yellow curve ($x = 0$) corresponds to stoichiometric Ni_2MnGa. The dashed lines are a guide to the eye and are situated at the energy values of the 14M structure of NiPtMnGa (squares) and Pt_2MnGa (diamonds). The curves for $x = 0.25$ and $x = 0.5$ have been calculated within a supercell consisting of 16 atoms. The energy scale has been chosen such that the $L2_1$-structure corresponds to the point of vanishing energy. Figure adapted from Ref. [176].

same time the magnetic moments of the Pt atoms ($0.12\,\mu_B$) are significantly smaller than the magnetic moments of the Ni atoms in Ni_2MnGa ($0.35\,\mu_B$ [3]). Thus, the addition of Pt leads to two opposing trends in the material. On the one hand the increased volume increases the magnetic moments of the individual elements while on the other hand the substitution of Ni atoms by Pt atoms leads to a decrease of the sum of magnetic moments in the cell because the magnetic moments of the Pt atoms are smaller than the magnetic moments of the Ni atoms. From the compositions that have been investigated here, $Ni_{1.5}Pt_{0.5}MnGa$ ($a = 5.95$ Å) shows the highest total magnetic moment (M=4.17 μ_B).

Fig. 6.1 also contains energy values for the 14M-structures of NiPtMnGa and Pt_2MnGa. The energy values of these structures have been obtained by taking the coordinates and crystal cell of the 14M structure of Ni_2MnGa [191] as a starting point of a DFT calculation which involved a full relaxation of the crystal structure, the volume and the atomic positions with a conjugate gradient algorithm [179]. The calculations have been performed in a unit cell consisting of 56 atoms making use of a different k-point grid ($10 \times 4 \times 8$ k-points) than the calculations within the 4-atomic unit cells ($15 \times 15 \times 15$ k-points). Therfore, the comparison of the different energies has to be done carefully. In order to approximate the error in the energy comparison that is related to the cell size and number of k-points, the total energy of

the $L2_1$-structure of Pt_2MnGa has also been calculated in a 56 atom supercell with exactly the same k-point grid as for the modulated structure. It turns out that the total energy per atom between the two different setups changes by 0.3 meV/atom in the case of the $L2_1$-structure. At the same time the energy difference between the 14M-structure and the $L2_1$-structure changes by 0.9% depending on the cell parameters. The result of these calculations allow to draw the conclusion that the different cell geometries and k-points only have minor influence on the total energy per atom and that it is reasonable to compare the $E(c/a)$-curves and the 14M-structures that have been calculated using different parameters.

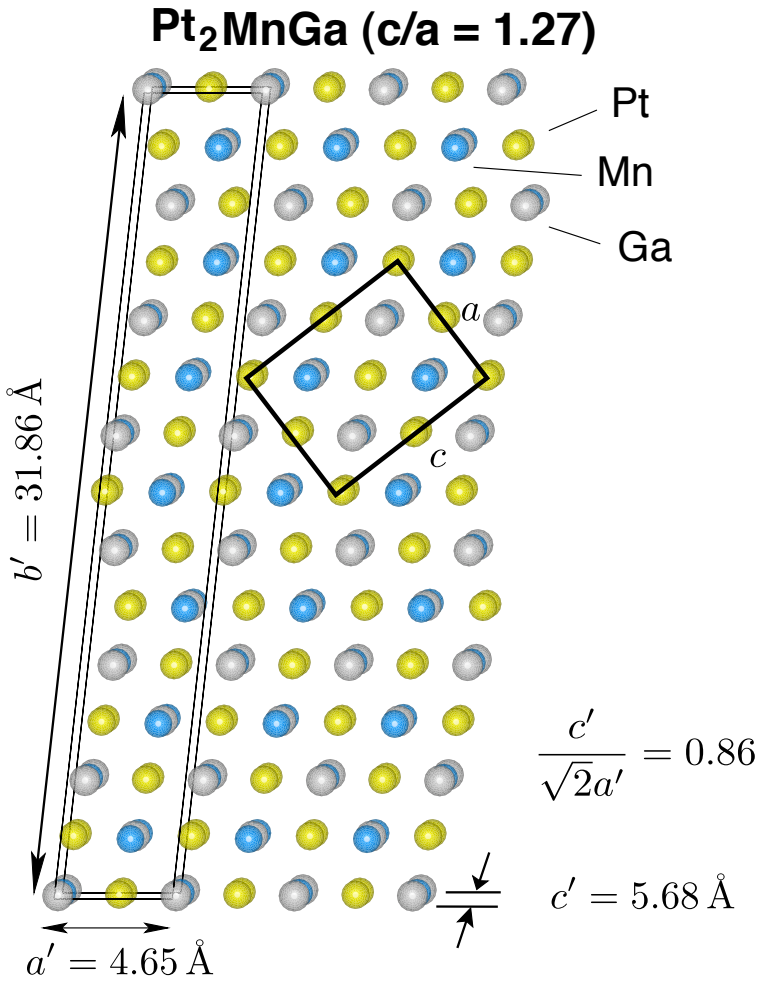

Figure 6.2: 14M structure of Pt_2MnGa. The black square illustrates the appearance of the $L1_0$-structure with $c/a = 1.27$ in the martensitic variants of the modulated structure. The c/a ratio of the 14M structure is 0.86. Figure adapted from Ref. [175].

The total energy calculations for the 14M structure show that the situation in the Pt-rich alloys is similar to the situation in Ni_2MnGa. In both cases the energy difference between the monoclinic modulated structure with $c/a < 1$ and the nonmodulated tetragonal structure

(NM) with $c/a > 1$ is rather small. The small energy difference is related to a small energy of twin boundary formation as the $L1_0$-structure and the 14M structure only differ by the additional twin boundaries that are introduced in the crystal cell of the modulated structure. The resemblance between the two structures is illustrated in Fig. 6.2 where the $L1_0$-structure is indicated as a black rectangle within one martensitic variant that appears in the 14M structure. [2] The periodic appearance of twin boundaries in the 14M structure has recently been investigated for Ni-Mn-Ga [193, 90]. In this context these twin boundaries on the nanoscale have been associated with the concept of adaptive martensite [91]. Fig. 6.2 also illustrates that the c/a ratio of the modulated structure is 0.86. As the c/a ratio of the modulated structures with $c/a < 1$ corresponds to the maximum strain that may be achieved in the system under the effect of an external magnetic field [194], magnetic field induced strains (MFIS) up to 14 % are expected in case of Pt_2MnGa.

Besides a tetragonal structure an orthorhombic structure also was considered as the crystal structure of the martensite in the past [186]. The preference for an orthorhombic structure can easily be checked by calculating the total energy E as a function of c/a and b/a. The resulting energy surface for Pt_2MnGa is plotted in Fig. 6.3. It is clearly visible that the minima of the energy surface turn up at tetragonal structures with either $b/a = 1$ or $c/a = 1$ which are symmetrically equivalent (the third minimum that is starting to evolve along the diagonal with $b/a = c/a < 1$ which is equal to $a/b = a/c > 1$ also corresponds to this tetragonal structure). This means that in the case of Pt_2MnGa the nonmodulated tetragonal structure is expected to be the ground state just as it is the case in Ni_2MnGa.

6.2 Phase stability and its relationship to magnetism

So far, the properties of the Ni-Pt-Mn-Ga alloys reveal many similarities to the Ni-Mn-Ga alloys while at the same time higher martensitic transformation temperatures might be expected for the Pt-rich alloys due to the energy differences between austenite and martensite structure which appear in the $E(c/a)$-curves. In order to further investigate the influence of magnetism on the stability of the nonmodulated martensite phase with respect to the austenite phase but also with respect to the 14M phase, the change of the $E(c/a)$-curves upon a reduction of the magnetic moment will be discussed within the following section. While a fixed spin moment calculation with a reduced magnetization which corresponds to the magnetization that is expected for a specific temperature is far away from an effective finite temperature description of relevant material properties it still can be used to investigate certain trends that appear at finite temperatures.

Fig. 6.4 contains the $E(c/a)$-curves and the energy of the respective 14M structure of NiPtMnGa for the ground state magnetization M_0 and three reduced magnetizations, namely

[2] The differences between the modulated and the tetragonal structure for the case of Ni-Mn-In have also been highlighted by Khovaylo *et al.* in 2009 [192].

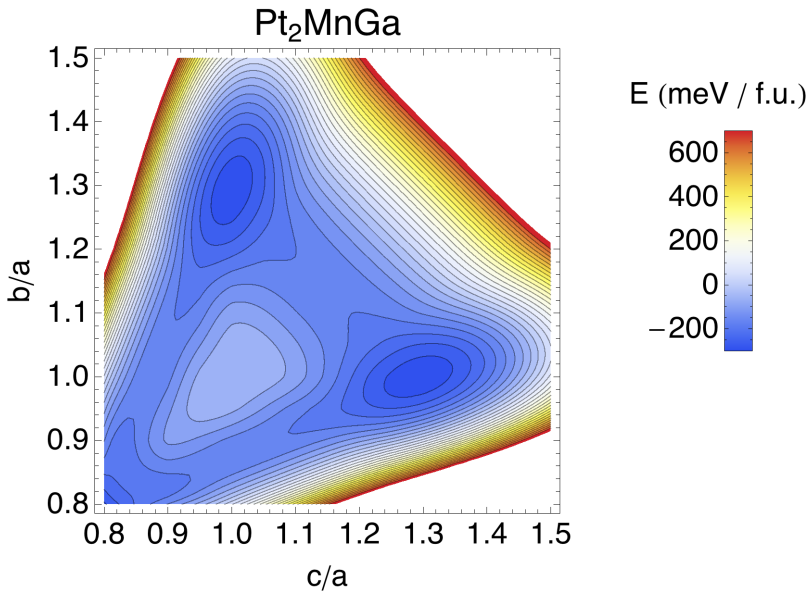

Figure 6.3: Total energy E as a function of b/a and c/a for Pt_2MnGa. The cubic structure with $b/a = c/a = 1$ corresponds to the case $E = 0$. Areas which are not coloured lie outside the plot range which means that the energy difference compared to the cubic structure is larger that 700 meV/f.u. for these regions.

$\frac{5}{6}\,M_0$, $\frac{2}{3}\,M_0$ and $\frac{1}{2}\,M_0$. The curves for the reduced magnetizations have been obtained using the fixed spin moment method. From the results of the calculations basically two trends can be extracted. First of all, the energy difference between the austenite structure ($c/a = 1$) and the nonmodulated martensite structure ($c/a > 1$) changes under a variation of the total magnetic moment. While it decreases upon reduction of the magnetic moment to two thirds of the ground state magnetization the energy difference increases again upon further reduction of the magnetic moment to half of the ground state magnetization. While a decrease of the energy difference upon reduction of the magnetization is also found in Ni_2MnGa [131] the increase of the energy difference at rather low magnetic moments seems to be unusual at first glance. However, as this unexpected behaviour appears at a magnetic moment which corresponds to half of the ground state magnetization it seems reasonable to assume that the predictive power of the fixed spin moment approach might already be decreased at such a significant reduction of the magnetic moment.

A second observation that can be made when looking at the results which are presented in Fig. 6.4 is the fact that the 14M structure always is lower in energy compared to the nonmodulated structure for the calculations with reduced magnetic moments. As this is not the case for the ground state magnetization where the nonmodulated structure is the global energy minimum one may assume that at finite temperature, but still below the martensitic transformation temperature the 14M structure is energetically favoured over the nonmodulated

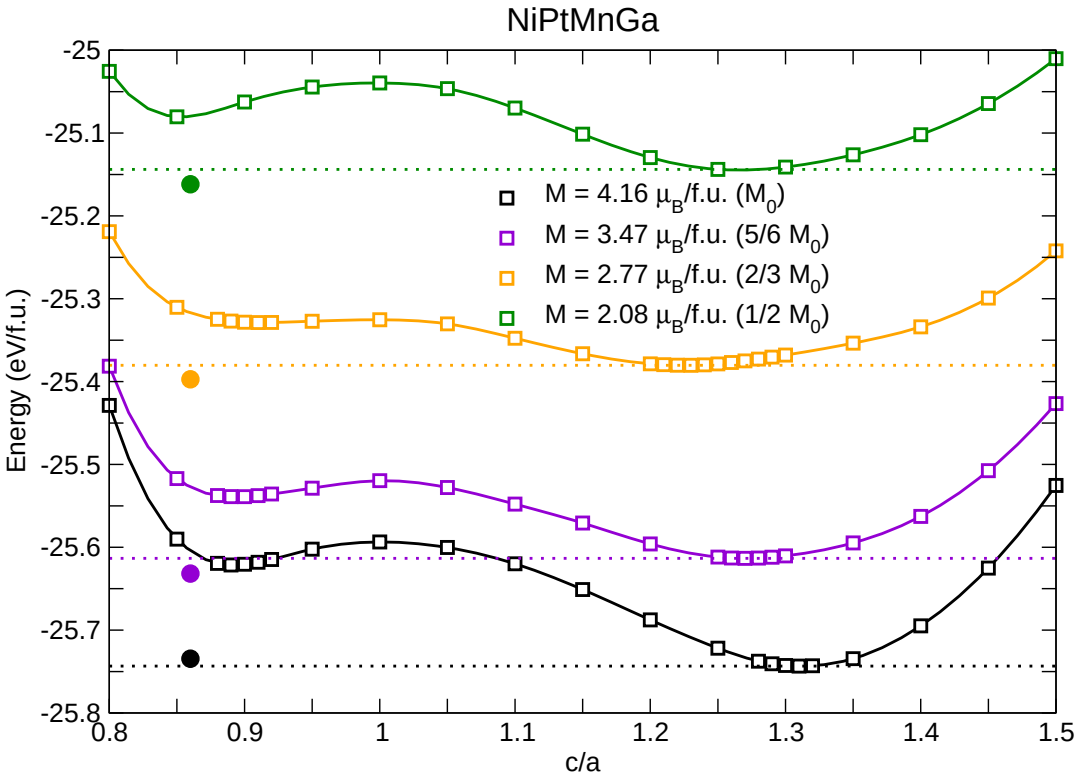

Figure 6.4: Total energy of NiPtMnGa as a function of tetragonality (c/a) for different values of the magnetic moment. For each curve (and the corresponding 14M structure which is marked as a dot in the same color coding) the total magnetic moment has been constrained to the value that is enlisted in the legend. The calculations which are coloured in black have been performed with no constraint for the magnetic moment. Here, $M = \mathrm{M}_0 = 4.16\,\mu_\mathrm{B}/f.u.$ refers to the magnetic moment of the cubic structure ($c/a = 1$).

tetragonal martensite structure whereas only for very low temperatures the nonmodulated structure is preferred. A similar behaviour is observed for a certain composition range of Ni-Mn-Ga [195]. Thus, the results which have been presented here give rise to the assumption that a similar sequence of phase transformations as in Ni_2MnGa, namely *Austenite* $\rightarrow$ *14M* $\rightarrow$ *NM* is also expected for NiPtMnGa. It should be noted here that the 5M structure has not been considered in the fixed spin moment calculations. However, similar to the situation in Ni_2MnGa the 5M structure also has to be considered from an energetic point of view in NiPtMnGa. In particular, the ground state energy of the 5M structure is only 1.7 meV/atom higher than the ground state energy of the 14M structure.

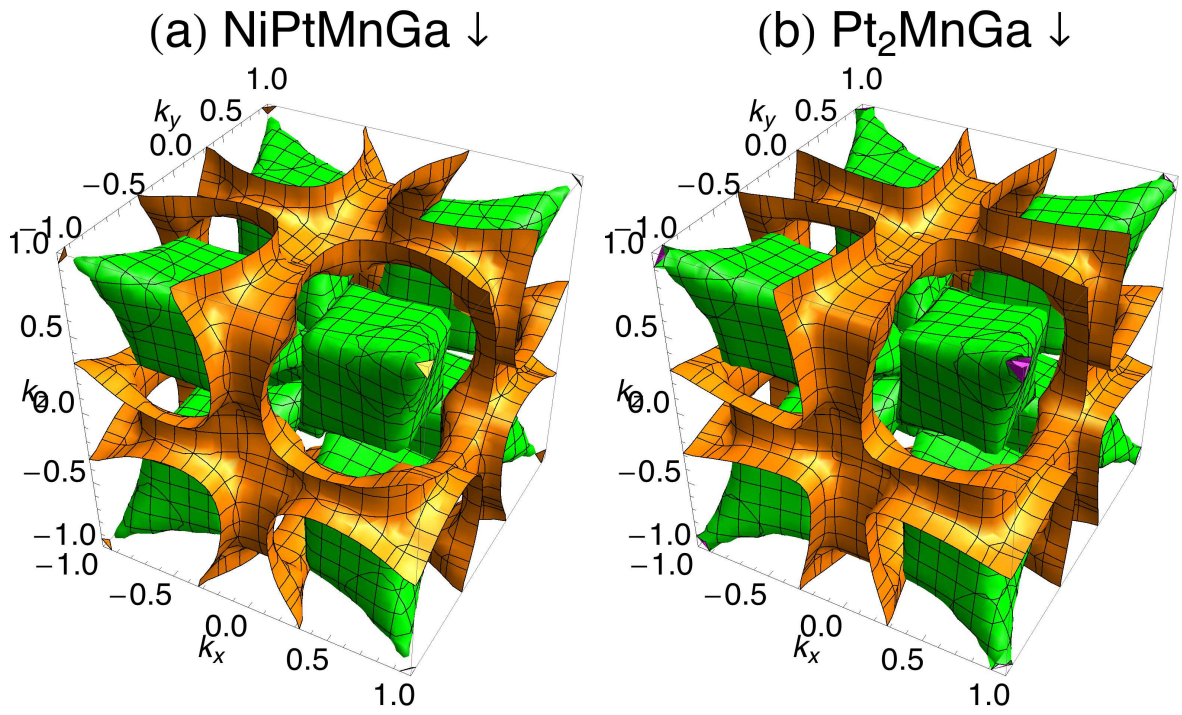

Figure 6.5: Spin-down Fermi surface of (a) NiPtMnGa and (b) Pt_2MnGa. The different colors denote different bands.

6.3 The change of electronic properties under an isoelectronic substitution

It was already mentioned that the substitution of Ni by Pt is isoelectronic which means that the alloy series $Ni_{2-x}Pt_xMnGa$ always has the valence electron density 7.5 independent from the amount of platinum that is added to the system. As $e/a = 7.5$ has been identified as a somewhat special number where all of the Fermi surfaces calculated for Ni-Mn-Z ($Z =$ Ga, In, Sn, Sb) within the rigid band approach reveal nesting features, the influence of the addition of platinum on the Fermi surface of Ni_2MnGa will be discussed in the following.

Fig. 6.5 shows the Fermi surfaces of the minority spin-channel of NiPtMnGa and Pt_2MnGa calculated for $31 \times 31 \times 31$ k-points. At first glance the Fermi surfaces reveal many similarities to the corresponding Fermi surface of Ni_2MnGa (see Fig. 3.5). However, there are also slight differences between the different surfaces. For example, the parallel sheets of the Fermi surface seem to be bended a little in case of Pt_2MnGa and even more in case of NiPtMnGa. In the latter case this behaviour can be attributed to the reduced symmetry of the NiPtMnGa compound where the simple cubic sublattice which consists of either Ni or Pt in case of X_2MnGa ($X =$ Ni, Pt) is replaced by a NaCl-type structure consisting of Ni and Pt.

A more detailed description of the influence of the addition of Pt on the Fermi surface is obtained by looking at the generalized susceptibility $\chi(\mathbf{q})$ as this quantity reveals peaks for wave vectors which correspond to nesting vectors of the Fermi surface [99]. In Fig. 6.6 the

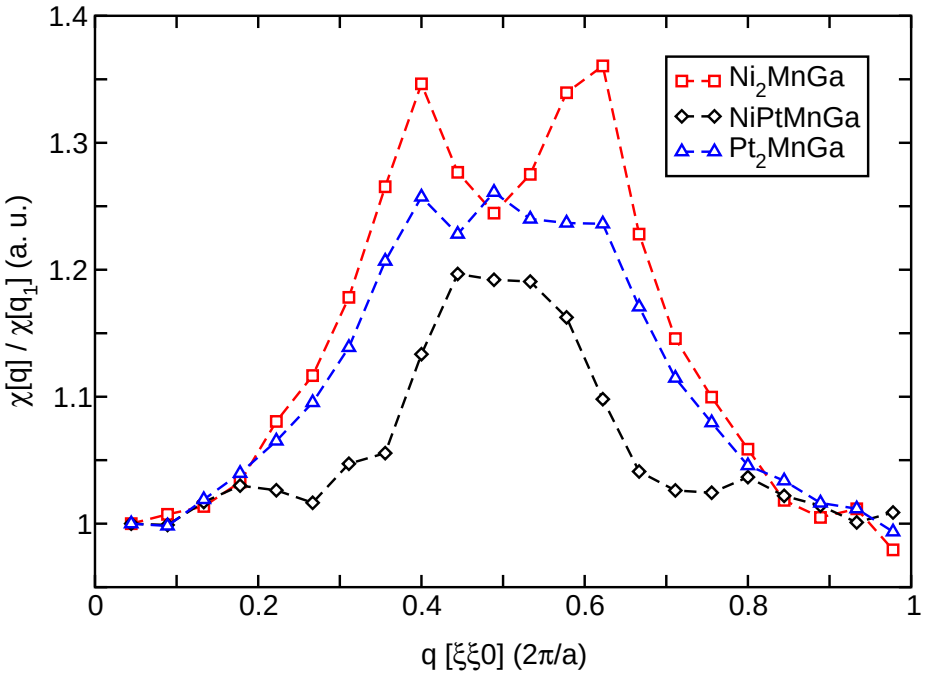

Figure 6.6: Generalized susceptibility $\chi(\mathbf{q})$ relative to $\chi(\mathbf{q}_1)$ for Ni_2MnGa, NiPtMnGa, and Pt_2MnGa along the [110] direction. For each compound the corresponding $\chi(\mathbf{q})$-curve has been divided by the value of $\chi(\mathbf{q}_1)$ where $\mathbf{q}_1$ is the first $\mathbf{q}$-point near the Γ point that was considered in the calculations ($\xi = \frac{2}{45}$).

generalized susceptibilities along the [110] direction which have been obtained from electronic structure calculations using $45 \times 45 \times 45$ k-points taking into account the spin-down bands according to equation (4.2) are plotted for Ni_2MnGa, NiPtMnGa, and Pt_2MnGa. For the purpose of comparison the curves for the different compounds each have been divided by the value of the respective susceptibility at the point $\mathbf{q}_1 = (\frac{2}{45}, \frac{2}{45}, 0)$. $\mathbf{q}_1$ is the $\mathbf{q}$-point which is situated nearest to the Γ point when considering all points that have been calculated along the [110] direction. Thus, the scale of Fig. 6.6 gives rise to the relative change of the susceptibility with regard to the wave vector $\mathbf{q}_1$ which is situated closely to the Γ point.

It is clearly visible that the most pronounced peaks of $\chi(\mathbf{q})$ relative to $\chi(\mathbf{q}_1)$ appear in the case of Ni_2MnGa. A second observation that can be made when looking at Fig. 6.6 is the merging of the two peaks that are present in the generalized susceptibility of Ni_2MnGa into one more or less diffuse peak in case of the systems containing platinum. Interestingly the bending of the parallel sheets of the Fermi surface in the Pt-rich alloys which was noticed especially in the case of NiPtMnGa (see Fig. 6.5) also turns up in the generalized suceptibilities as $\chi(\mathbf{q})$ reveals a rather smeared out peak in the case of this compound. Nevertheless it can be concluded that the resemblance between Ni_2MnGa and the Pt-rich alloys in general also is present with respect to Fermi surface nesting and the shape of the generalized susceptibility.

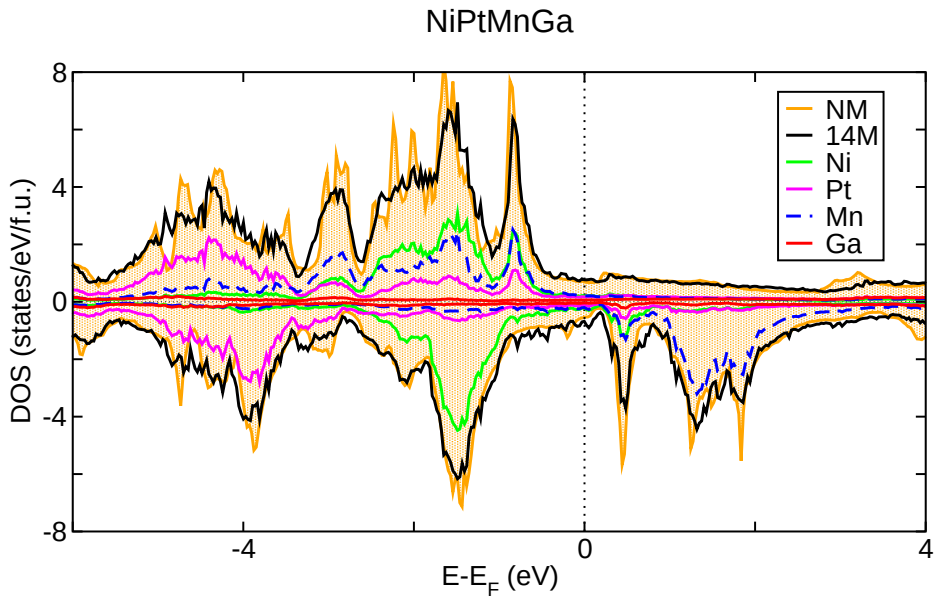

Figure 6.7: Electronic density of states of NiPtMnGa. The yellow curve refers to the total density of states of the nonmodulated martensite (NM) structure while the black curve refers to the total density of states of the 14M-structure. The elemental contributions that are plotted belong to the density of states of the 14M-structure. Figure adapted from Ref. [175].

However, the Fermi surface nesting and therefore also the peaks of $\chi(\mathbf{q})$ are not as pronounced as in the case of Ni_2MnGa.

It was pointed out in section 6.1 that the 14M-structure and the structure of the nonmodulated martensite (NM) are closely connected in the spirit of the concept of adaptive martensite. It is therefore not surprising that the resemblance between these two structures also appears in the electronic density of states. The electronic density of states of both, the 14M-structure and the NM-structure are plotted in Fig. 6.7. The similarities between the densities of states of the two structures are clearly visible and can be explained by the fact that the two structures only differ by the twin boundaries on the nanoscale that are introduced in order to obtain the modulated structure. It should be noted at this point that besides Fermi surface nesting, which is still present in the Pt-based alloys but weaker than in Ni_2MnGa, the band Jahn-Teller effect is also present in NiPtMnGa [175]. Thus, not only the structural but also the electronic properties are not affected significantly by the addition of platinum with the exception that the preference of tetragonal structures is increased as the amount of Pt in the alloy is increased.

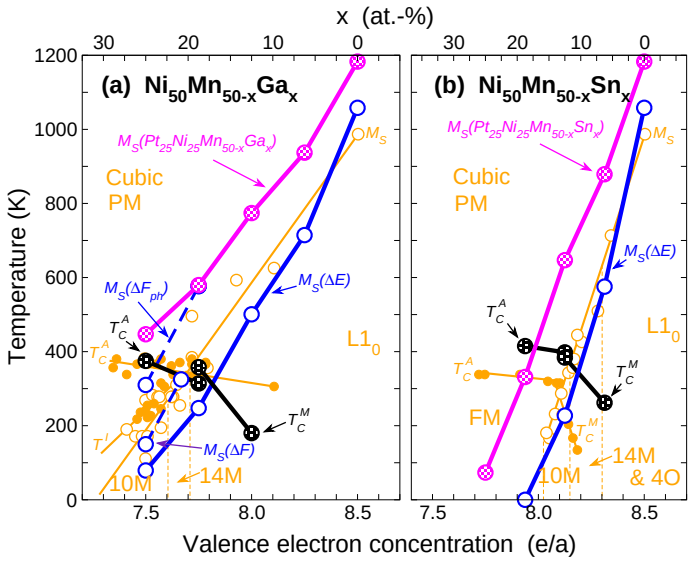

Figure 6.8: Phase diagram of Ni-Pt-Mn-Z ($Z =$ Ga, Sn). The magenta curves refer to the transformation temperatures obtained from the calculations of structural energy differences that appear in the alloys containing 25 at.% Pt. For an explanation of the other elements in the graph see Fig. 5.6 and the corresponding explanation. Figure adapted from Ref. [176].

6.4 The phase diagram of Ni-Pt-Mn-Z

It was already pointed out in section 6.1 that the martensitic transformation temperatures of $Ni_{2-x}Pt_xMnGa$ are expected to increase with increasing Pt content. At this point the question arises whether a further increase of T_M can be expected when replacing Ga by Mn just as it is known for the Ni-Mn-Z ($Z =$ Ga, In, Sn, Sb) compounds.

In the following the results of the calculation of the structural energy differences of two compounds, namely Ni-Pt-Mn-Ga and Ni-Pt-Mn-Sn will be presented. In both cases the ratio of Ni and Pt was fixed to 25 at.%. Thus, the alloy series $NiPtMn_{1+x}Z_{1-x}$ ($Z =$ Ga, Sn) have been studied. The investigations have been undertaken using the same *ab initio* methods and procedures that have already been discussed in chapter 5. It turns out that the alloys containing platinum reveal a similar behaviour regarding the magnetic structure and the change of the martensitic transformation temperature with valence electron concentration as the alloys where Pt is absent. In particular, an antiferromagnetic alignment of the magnetic moments of the additional Mn atoms on the Z sites is preferred over a purely ferromagnetic alignment. The onset of antiferromagnetism results in increased structural energy differences between the austenite and martensite structure, in analogy to the situation in Ni-Mn-Z.

The phase diagram that has been obtained for the two alloy series is plotted in Fig. 6.8. For comparison, the experimental and theoretical results for the systems without Pt are also in-

cluded in the figure. It is clearly visible that also for the Ni-Pt-Mn-Z alloys a linear dependency of the martensitic transformation temperature T_{M} (M_{S}) on the valence electron concentration e/a is obtained. However, due to the presence of the Pt atoms which result in an increased preference of tetragonal structures, higher transformation temperatures than for the materials without platinum are expected.

6.5 Conclusion

The *ab initio* investigation of Ni-Pt-Mn-Z ($Z = \mathrm{Ga}$, Sn) reveals that the substitution of Ni by Pt is expected to beneficially increase or at least retain the material properties which are relevant for the magnetic shape memory effect. In particular, the calculation of the $E(c/a)$-curves gives rise to the expectation of higher martensitic transformation temperatures because the energy difference between austenite and martensite structure increases, as the amount of platinum is increased. At the same time, the energy relation between the nonmodulated martensite structure and the 14M-structure is similar to Ni_2MnGa. The fixed spin moment calculations for reduced magnetizations show, that a similar sequence of phase transitions as in the magnetic shape memory reference material is also expected upon cooling in case of the Ni-Pt-Mn-Ga. A detailed analysis of the electronic structure reveals that the peaks which appear along the [110] direction in the generalized susceptibility are not as pronounced as in Ni_2MnGa. However, the general trends that appear in the Fermi surface of Ni_2MnGa are also present in the isoelectronic compounds with Pt excess. Finally, also the behaviour of the martensitic transition temperature under an increase of the valence electron concentration has been found to coincide with the situation that is present in the Ni-based Heusler alloys. Thus, the Pt-based alloys seem to be rather promising candidates for the industrial application of the magnetic shape memory effect. Nevertheless, there also remain some issues to be solved regarding this material class. First of all platinum is a rather expensive material which hinders the use of compositions with large amount of platinum in many application fields. However, as only small amounts of Pt already significantly change the energy landscape (see Fig. 6.1) the usage of quaternary alloys Ni-Pt-Mn-Z with only small amounts of Pt (around 10 at.%) could still be useful from an economic point of view. Secondly, the proposed composition range also is of particular interest from another point of view as the type of magnetic ordering in Pt_2MnGa is not clear and it is also not clear whether compositions like NiPtMnGa will order in the crystal structure that has been assumed here. Compositions containing only small amounts of platinum should avoid this problem as the stability of the Ni sublattice would most likely be retained while also the influence of the doping on the magnetic ordering should be of minor importance for such compositions. Last but not least compositions containing only small amounts of Pt also reveal lattice constants which are below the critical value of $a_{\mathrm{c}} \approx 6\,\text{Å}$ which has been suggested by Planes *et al.* as a prerequisite for martensitically transforming Heusler alloys in case of the Ni-Mn-Z compounds [105]. Interestingly, the here proposed addition of

small amounts of Pt reveals analogies to the idea of Enkovaara *et al.* who proposed already in 2003 that the replacement of small amounts of Ni by non-magnetic elements like Cu could lead to an increase of T_C in Ni_2MnGa [196].

Very recently, some new experimental results on Pt-based magnetic shape memory alloys have been published. In particular, higher martensitic transformation temperatures ($M_S = 283\,K$) than for Ni_2MnGa have been reported for the composition $Ni_{1.8}Pt_{0.2}MnGa$ [176]. Furthermore, the formation of the 7M structure in a sample of the same composition was experimentally demonstrated within neutron diffraction studies [197]. In the same article, higher martensitic transformation temperatures ($M_S = 285\,K$) and a higher magnetic moment in the martensite phase than for Ni_2MnGa have also been reported for this composition. This means that on the one hand the theoretical and experimental results both give evidence for the interesting properties of the Pt-based alloys which require a further investigation in the future. On the other hand the Ni-Pt-Mn-Z alloys are also interesting from a fundamental point of view as they effectively demonstrate how new materials can be designed making use of an intense interplay between theoretical and experimental methods.

Chapter 7

Co-Ni-Ga

The Heusler alloys based on Ni and Mn that have been investigated in the previous chapters still face problems regarding their use in industrial applications of the magnetic shape memory effect. Besides the brittleness, the most important issue that has to be solved concerns the transformation temperatures. For most applications both, T_C and T_M require to be above room temperature. However, while the addition of Mn increases T_M, the antiferromagnetic interactions that are introduced by the excess Mn atoms reduce the magnetization (see chapter 5). While the addition of platinum in principle increases the transformation temperature without reducing the magnetization (see chapter 6), such type of substitution is promising at first glance. However, from an economic point of view the use of Pt does not seem to be ideal regarding the material price while at the same time the use of quaternary alloys might introduce additional issues in the production process.

Due to these circumstances, other materials which do not contain Mn have been considered in the past, when searching for magnetic shape memory alloys with ideal material properties. One of these materials is the alloy system Co-Ni-Ga which was considered as a magnetic shape memory material already in 2001 by different groups [69, 70]. Meanwhile, magnetic field induced strains (MFIS) of about 7.6 % have been obtained for off-stoichiometric compositions at room temperature under the application of external stress [198]. A major difference of Co-Ni-Ga in comparison to Ni-Mn-Ga is the preference for disorder which however depends on the composition and sample preparation [199, 71]. Furthermore it has been observed that the sample preparation also may influence the transformation temperature [200].

The properties of Co-Ni-Ga that have been derived by making use of *ab initio* calculations and especially the differences compared to Ni_2MnGa will be discussed in the following chapter.

7.1 Co_2NiGa

In this section the results for the stoichiometric composition Co_2NiGa will be presented. The stoichiometric composition is of interest as it allows a close comparison with the stoichiometric composition Ni_2MnGa and at the same time also can be handled with feasible computational effort. While the absence of Mn in Co_2NiGa avoids the appearance of antiferromagnetic interactions it also leads to a reduced magnetization as the magnetic moment in Ni_2MnGa is mainly contributed by the Mn atoms. The replacement of Ni by Co partially compensates this loss

as the magnetic moments of the Co atoms in Co_2NiGa are significantly larger ($1.15\,\mu_B$/atom) than the magnetic moments of the Ni atoms in Ni_2MnGa ($0.35\,\mu_B$/atom [3]). However, the total magnetization of Co_2NiGa ($2.67\,\mu_B$/f.u.) still is about 34% reduced compared to Ni_2MnGa. At the same time, the lattice constant is also smaller than in Ni_2MnGa. The calculated value within the GGA (PBE) approximation is $a = 5.695\,$Å [201].

A significant difference to the Ni_2MnGa reference system becomes evident when comparing the preference for different types of crystal structure. Here, basically the two structures known as conventional (or regular) and inverse Heusler structure will be considered. In the literature the conventional structure is sometimes also referred to as Cu_2MnAl-type structure while the inverse structure is denoted as Hg_2CuTi-type structure in these cases [202]. The conventional Heusler structure consists of two interpenetrating simple cubic sublattices of which one is completely occupied by one atom type while the other atom is occupied by two atom types in the same way as is the case in the NaCl-structure (B1-structure). The inverse Heusler structure is obtained from the conventional Heusler structure denoted as X_2YZ by exchanging one of the two X atoms in the one sublattice with either the Y or the Z atom from the other sublattice. The notation of the inverse Heusler structure is (XY)XZ in analogy to the conventional structure. Thus, both structures only differ in the site occupancy while the positions of the lattice sites are equal for both structures. This means that the conventional as well as the inverse structure both are $L2_1$-type structures [202]. Fig. 7.1 schematically shows the differences between the two structures in case of Co_2NiGa. As a direct consequence of the atom substitution the X atoms which all occupy the same sublattice in the conventional structure become nearest neighbours in the inverse structure. The inverse structure was mentioned already in 1978 by Jaggi *et al.* in the context of Fe_2CoGa [203]. While a recent *ab initio* study of this material class revealed that the inverse structure indeed is of importance for this type of alloys [204, 205] it also is found for Mn_2NiGa [206, 207, 208]. In fact, a computational study published by Gillessen and Dronskowski in 2009 predicts, that the inverse structure is expected for many ternary compounds [209].

In Ni_2MnGa, the inverse Heusler structure does not require further discussion because the energy of this crystal structure is 116 meV/atom higher than the energy of the conventional Heusler structure at $T = 0$K. The appearance of the partially ordered B2-structure at high temperatures [80] gives an additional evidence that an intermixing of the Ni-sublattice and the Mn/Ga-sublattice is not likely to appear within an experimental sample. In Co_2NiGa, the situation is completely different. In this case the energy difference between the two structures amounts to 3.66 meV/atom at $c/a = 1$ with the inverse Heusler structure having the lowest energy and a slightly increased lattice constant of $a = 5.711\,$Å compared to the conventional structure. [1]

[1] It has been observed that the inverse Heusler structure often is preferred for alloys of the type X_2YZ where the number of $3d$ electrons of the Y atoms is larger than that of the X atoms [210]. Interestingly the Ni_2MnGa alloy as well as Co_2NiGa are both consistent with this observation.

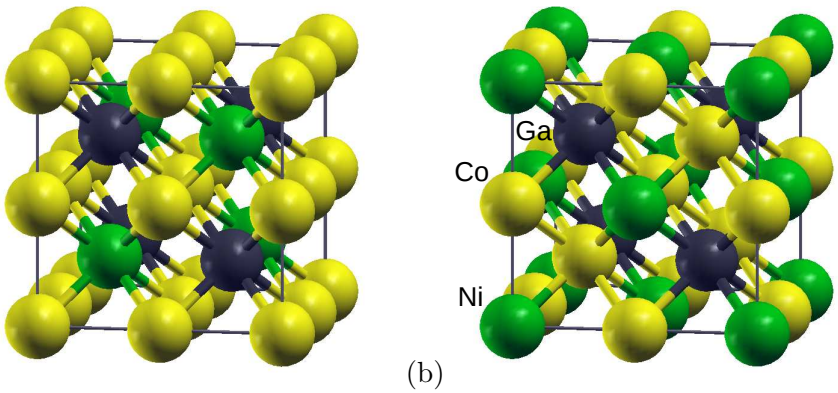

(a) (b)

Figure 7.1: Schematic representation of (a) the conventional (or regular) Heusler structure and (b) the inverse Heusler structure of Co_2NiGa. The Co atoms are marked yellow, the Ni atoms are marked green, and the Ga atoms are colored in black. One of the simple cubic lattices corresponding to a NaCl-structure is fully occupied by the Co atoms in case of the conventional structure. By exchanging the Co atoms on one of the two lattice sites of the NaCl-structure with either the Ni or the Ga atoms of the other sublattice the inverse Heusler structure is obtained. In this structure, the Co atoms become nearest neighbours. Adapted from Ref [201].

In contrast to Ni_2MnGa which is found in the $L2_1$-structure it has been found experimentally that the crystal structure of Co-Ni-Ga depends on the sample preparation and composition. While an experimental study by Oikawa *et al.* revealed a B2-type structure which transforms martensitically into the $L1_0$-structure for a wide range of compositions [69] neutron diffraction studies by Brown *et al.* did not reveal a B2-structure for a composition with Ga excess ($Co_{1.8}Ni_{0.92}Ga_{1.28}$) [71]. For a stoichiometric composition, Dai *et al.* observed an ordered structure (Pt_2FeCu-type) as well as a completely disordered structure [199]. However, the theoretical methods which are applied here do not allow to simulate ideally disordered structures. Nevertheless, the investigation of the two different structures, namely the conventional and the inverse structure, proves sufficient to reveal the essential physical trends. In this context it should also be mentioned that an *ab initio* investigation of Arróyave *et al.* revealed that the B2-structure is not favoured over the conventional Heusler structure in Co_2NiGa [211].

A more detailed insight to the energetic relationship between the different crystal structures is obtained by calculating the $E(c/a)$-curves of the specific structure in a similar manner as it has been done for the other investigated materials before. Fig. 7.2 (a) contains the results of these calculations for the conventional Heusler structure and inverse Heusler structure of Co_2NiGa. As can be seen, the inverse structure is favoured over nearly the whole range of c/a-ratios. However, as it has been pointed out before the difference between the two structures becomes very small in case of $c/a = 1$. From the curvature of the $E(c/a)$-curve of the inverse structure at this point it is already clear that the system will be dynamically unstable and

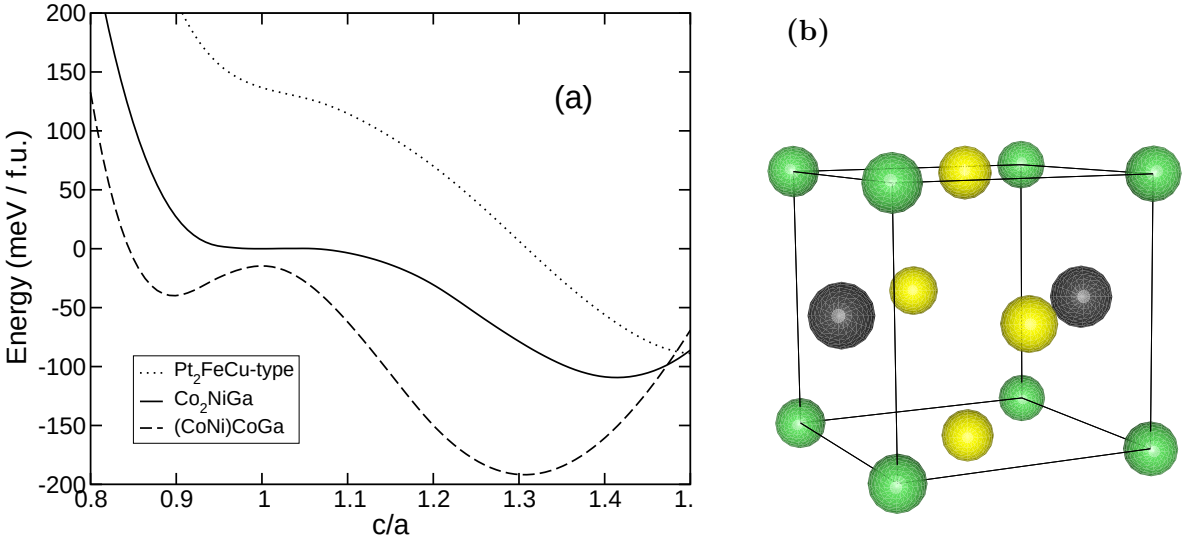

Figure 7.2: (a) Total energy as a function of c/a for different crystal structures of stoichiometric Co_2NiGa. Besides the conventional Heusler structure, denoted as Co_2NiGa, and the inverse Heusler structure, denoted as (CoNi)CoGa, also results for the so-called Pt_2FeCu-type structure are presented. All calculations have been performed at the ground state volume of the respective cubic structures. The energy scale has been chosen such that the cubic cell of the conventional Heusler structure corresponds to the point of vanishing energy. (b) Schematic representation of the Pt_2FeCu-type structure. The Ni atoms are marked green whereas the Ga atoms are marked black and the Co atoms are marked yellow. Figure partially adapted from Ref. [212].

reveal imaginary phonon frequencies. While this issue will be discussed in detail later, Fig. 7.2 (a) already gives a hint that Co_2NiGa should be further investigated with regard to the magnetic shape memory effect as tetragonal distorted structures are favoured over the cubic structure at very low temperatures. In particular, the $E(c/a)$-curve of the inverse structure reveals a global energy minimum at $c/a = 1.31$ while the corresponding minimum of the conventional structure is situated at $c/a = 1.41$. Thus, the conventional structure in fact favours an fcc-type structure as a c/a ratio of $\sqrt{2}$ corresponds to a perfect fcc lattice within the Bain transformation.

While the energy difference between conventional and inverse Heusler structure is small for $c/a = 1$ it increases with increasing c/a until it reaches a maximum of 31.21 meV/atom at $c/a = 1.25$. The energy difference between the cubic structure ($c/a = 1$) and the global energy minimum amounts to 27.3 meV/atom in case of the conventional structure and 37.98 meV/atom in case of the inverse Heusler structure. These values are by a factor of 4 (conventional) and 6.5 (inverse) higher than the energy difference that occurs for the conventional Heusler structure

of Ni_2MnGa (6.81 meV/atom [3]).

Besides the two discussed crystal structures, namely the conventional and inverse structure, Fig. 7.2 (a) also contains the results of Co_2NiGa for the so-called Pt_2FeCu-type structure which is illustrated in 7.2 (b). This structure corresponds to a fcc-type structure where the Ni atom is placed in the origin of the primitive unit cell and the faces of the cell are occupied by the Ga atom and the two Co atoms. While this structure was found by Dai *et al.* in a stoichiometric sample in 2007 [199], the density functional theory calculations reveal that this structure is energetically not favoured at low temperatures. However, Dai *et al.* also observed that the structure of the crystal depends significantly on the sample preparation and that disordered structures are also observed in the stoichiometric composition [199]. Therefore, the Pt_2FeCu-type structure will not be considered in the further discussion.

7.1.1 The phonon spectrum of Co_2NiGa

As the conventional Heusler structure of Co_2NiGa reveals a similar $E(c/a)$-curve as Ni_2MnGa, it seems nearby to investigate the stability of the conventional structure by a calculation of the phonon dispersion curve which is plotted in Fig. 7.3. It turns out that although the cubic structure with $c/a = 1$ seems to be situated rather on a saddle point than on a mininum, the phonon spectrum does not reveal instabilities caused by imaginary phonon modes. Nevertheless, the phonon spectrum of the conventional structure reveals that also in this material the TA_2 branch is found at rather small phonon frequencies along the [110] direction. Although no softening, but a regular, sinusoidal behaviour is observed the branch does not reveal frequencies larger than 1.5 THz. At the zone boundary, the value becomes even smaller and is in the range of 1 THz. The results that are represented here are in very good agreement with *ab initio* results obtained by Arróyave *et al.* [211].

Fig. 7.3 also contains the results of neutron scattering measurements of the TA_2 branch along the [110] direction which have been performed using an off-stoichiometric experimental sample with the specific composition $Co_{48}Ni_{22}Ga_{30}$ at $T = 300$ K by S. M. Shapiro *et al.*. Also in this case, no signs for phonon softening appear. It is remarkable that the stoichiometric calculations and the off-stoichiometric measurements perfectly agree in the part of the Brillouin zone that is situated near the Γ-point while significant deviations appear in the other part of the Brillouin zone which is close to the zone boundary. The composition $Co_{48}Ni_{22}Ga_{30}$ is of interest as it transforms martensitically. The experimentally obtained transformation temperatures are 284.1 K (M_S), 269.4 K (M_F), 280.8 K (A_S), and 295.2 K (A_F) [201].

As was pointed out before, the phonon spectrum of the inverse structure has to be unstable in case of the cubic structure due to the curvature of the $E(c/a)$-curve at $c/a = 1$. However, in the neutron scattering measurements of $Co_{48}Ni_{22}Ga_{30}$ no signs for phonon softening are observed. Fig. 7.4 contains temperature dependent measurements for the specific composition which reveal that in contrast to Ni_2MnGa no temperature dependent softening is observed. This means that the driving forces of the martensitic transformation in the Co-Ni-Ga sample are different

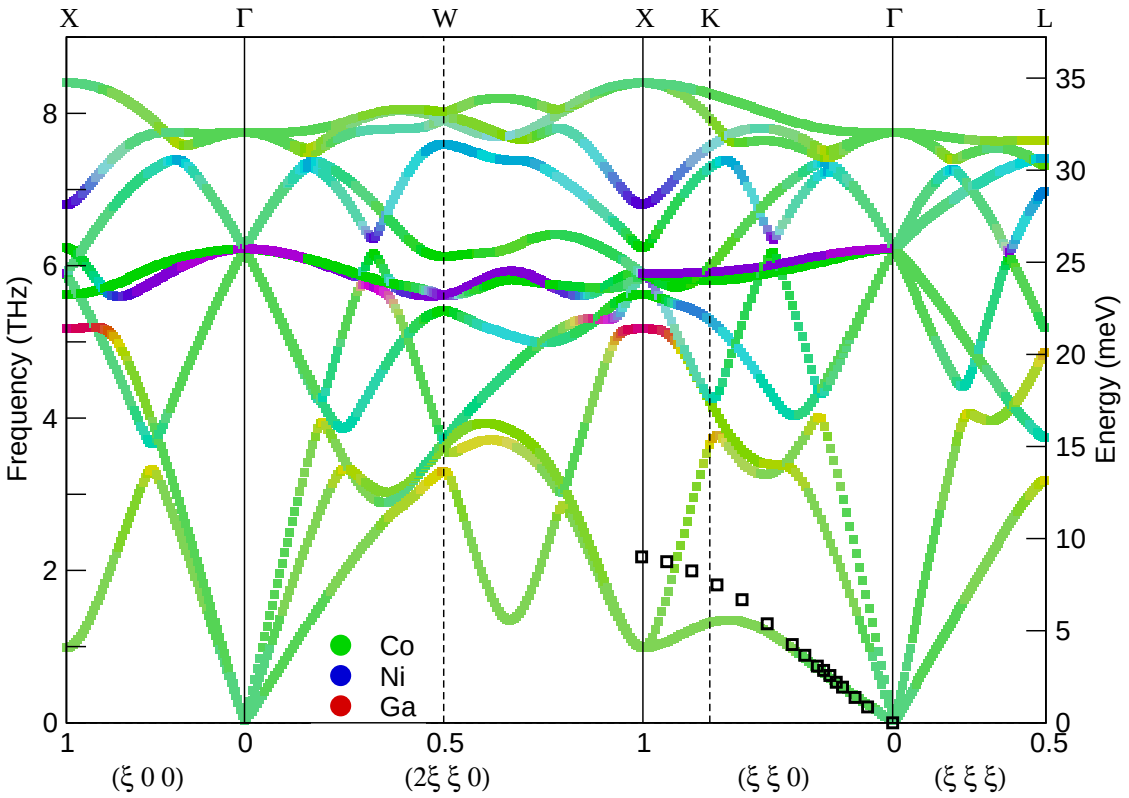

Figure 7.3: Phonon dispersion curve of the conventional Heusler structure of cubic Co_2NiGa. The black squares refer to neutron scattering measurements of $Co_{48}Ni_{22}Ga_{30}$ [201]. The color coding represents the contribution of the different atoms to the respective phonon modes. Adapted from Ref. [212].

compared to Ni_2MnGa. As the crystal structure of the experimental sample is not clear and also because of the appearance of deviations between the theoretical phonon dispersion for the stoichiometric composition and the experimental phonon dispersion for an off-stoichiometric composition further investigations taking into account off-stoichiometric compositions in the calculations are required to understand the results which have been obtained in the neutron scattering experiments. The first-principles investigation of off-stoichiometric compositions will be part of the following section.

7.2 Off-stoichiometric compositions

The calculation of off-stoichiometric compositions is not only motivated by the attempt to theoretically model the composition for which the neutron scattering measurements in Fig. 7.4 have been undertaken but also by the fact that it is known that the martensitic transformation temperature in Co-Ni-Ga significantly depends on the composition of the sample [213]. The experimental phase diagram of Co-Ni-Ga which is depicted in Fig. 7.5 consists of several

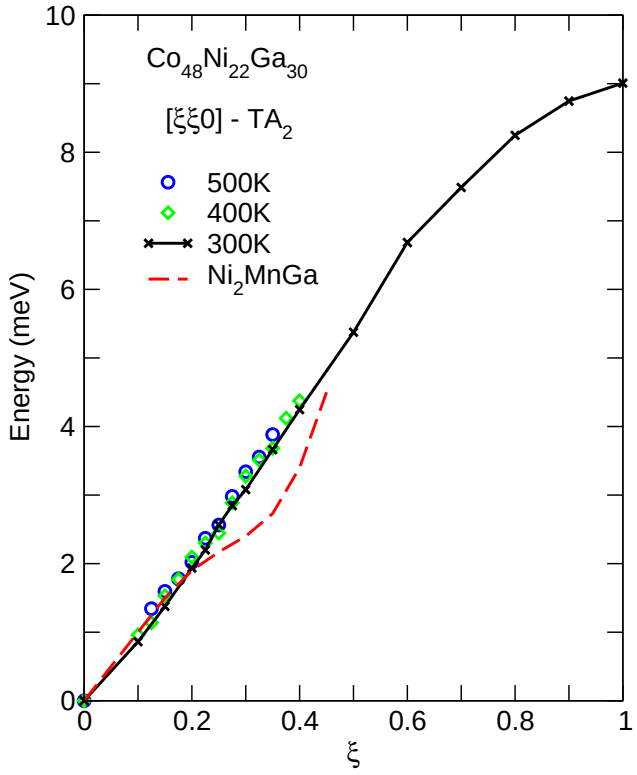

Figure 7.4: Temperature dependence of the phonon frequencies of $Co_{48}Ni_{22}Ga_{30}$ along the [110] direction. For comparison, the experimental phonon dispersion of Ni_2MnGa which was taken from Ref. [81] is also plotted. Adapted from Ref. [201].

phases. The important phase with respect to the magnetic shape memory effect is the β'-phase which corresponds to a tetragonal distorted bcc phase. The stoichiometric composition Co_2NiGa is denoted as a yellow circle in Fig. 7.5 and lies in between the bcc- and the fcc-region. The $E(c/a)$-curve of the conventional Heusler structure of this composition which is plotted in Fig. 7.2 (a) is in agreement with this attribute, as the global minimum at $c/a = 1.41$ already corresponds to an fcc-type structure while still a local minimum at $c/a = 1$ is present.

The experimental sample with the atomic composition $Co_{48}Ni_{22}Ga_{30}$, which undergoes a martensitic transformation, is situated at the edge of the β'-phase in the phase diagram (depicted as a white square). In order to model off-stoichiometric alloys, just as for the Ni-Mn-Z compounds, supercells consisting of 16 atoms were used. The two compositions that are closest to the experimental sample ($Co_{1.92}Ni_{0.88}Ga_{1.2}$) using this size of supercell are $Co_2Ni_{0.75}Ga_{1.25}$ ($Co_8Ni_4Ga_5$ supercell) and $Co_{1.75}NiGa_{1.25}$ ($Co_7Ni_4Ga_5$ supercell). Both supercell compositions are depicted as white circles in Fig. 7.5. The number of valence electrons per atom e/a, which is 7.75 for the stoichiometric composition is decreased for the compositions in the region of the β'-phase. In particular, the composition of the experimental sample has an e/a-ratio of $e/a = 7.42$, while the two off-stoichiometric supercell compositions that have been considered

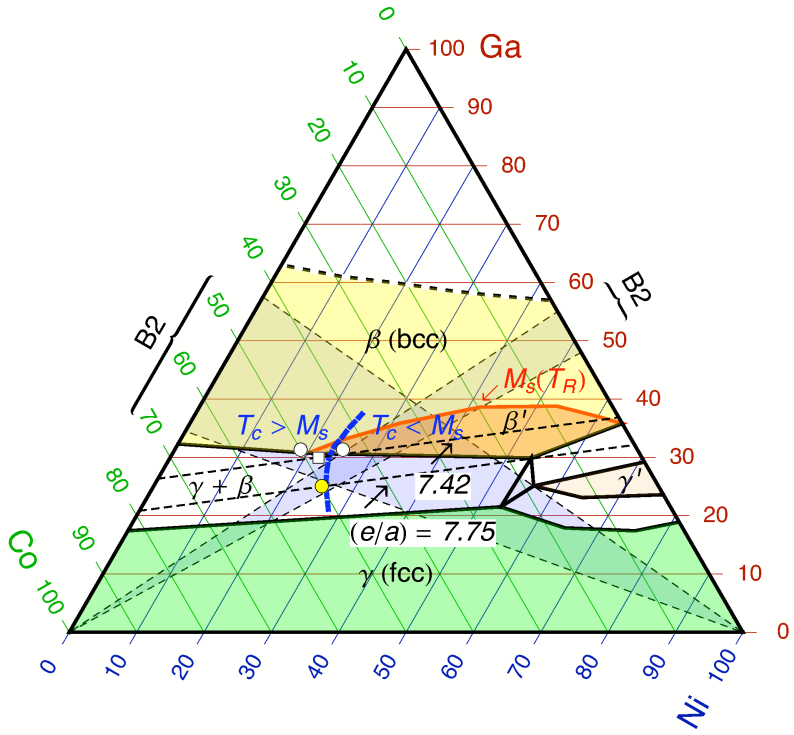

Figure 7.5: Ternary phase diagram of the Co-Ni-Ga alloy reconstructed from experimental data. The dashed triangles mark the extrapolated B2 phases which already give a hint in which parts of the phase diagram $L2_1$-like structures that are relevant for the magnetic shape memory effect are likely to be expected [214]. The red curve represents the points where M_S is found at room temperature (T_R) [215]. The thick blue dashed lines separate the regions where T_C is larger or smaller than M_S [216]. The dashed lines mark the points of constant e/a (7.42 and 7.75). Adapted from Ref. [201].

here have an e/a ratio of 7.31 ($Co_2Ni_{0.75}Ga_{1.25}$) and 7.38 ($Co_{1.75}NiGa_{1.25}$). It should be mentioned that the first of these compositions is situated in a region of the phase diagram where the magnetic shape memory effect ($Co_{50}Ni_{20}Ga_{30}$) and pseudoelasticity ($Co_{49}Ni_{21}Ga_{30}$) have already been observed experimentally in the past [217, 218].

The calculations of the off-stoichiometric compositions of Co-Ni-Ga face some issues that are not present in the Ni-Mn-Z alloys. Due to the fact that the conventional and inverse structure do not differ significantly in energy, one cannot assume that particular sublattices are not affected by the atomic substitution that is applied to end up in an off-stoichiometric composition of the supercell. In particular, depending on the type of Heusler structure (conventional or inverse) the density functional theory calculations suggest that the substituted atom does not directly occupy the lattice site of the atom which it is replacing in some cases.

Instead, for these cases a configuration where the substituted atom occupies the lattice sites of a third atom which therefore moves to the lattice site of the atom that has been replaced during the substitution is favoured. This behaviour is not only observed for the compositions that are discussed here, but also for the Ni-rich composition $Co_2Ni_{1.25}Ga_{0.75}$, which will be discussed in section 7.3. In addition to the correct choice of the atomic configuration atomic relaxations also have to be considered within the off-stoichiometric supercells in order to obtain a proper description of the energy landscape for the respective compositions. This is in contrast to Ni-Mn-Z where it turned out that atomic relaxations are of minor importance (see Table 5.2).

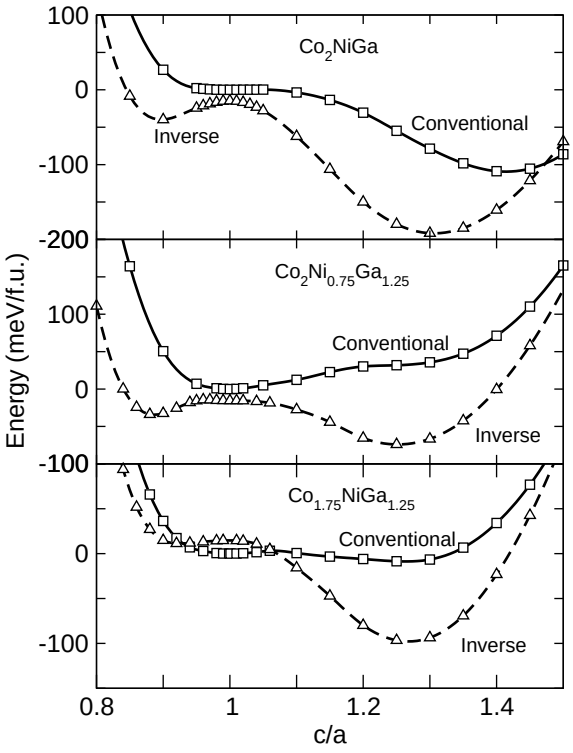

Figure 7.6: Total energy for different crystal structures as a function of tetragonality c/a for Co_2NiGa, $Co_2Ni_{0.75}Ga_{1.25}$, and $Co_{1.75}NiGa_{1.25}$. The calculations for $Co_{1.75}NiGa_{1.25}$ have been performed by M. E. Gruner [201]. Figure adapted from Ref. [201].

The $E(c/a)$-curves for the conventional and inverse Heusler structure of the stoichiometric as well as for the two off-stoichiometric compositions which have been considered here are presented in Fig. 7.6. For each crystal structure the curve of the atomic arrangement with the lowest energy is plotted, taking into account different types of configurations and atomic relaxations, as described in the last paragraph. It is remarkable that the energy difference between the conventional and inverse Heusler structure at $c/a = 1$ is in the range between

3.65 meV/atom ($Co_{1.75}NiGa_{1.25}$) and 3.86 meV/atom ($Co_2Ni_{0.75}Ga_{1.25}$) for all three compositions. Thus, the energy difference between the two different crystal structures also is small for the off-stoichiometric compositions. This means that a mixture of the structures, i.e. disorder, is likely to be expected within an experimental sample in the complete region of the ternary phase diagram that is defined by the investigated compositions. A second observation that can be made when looking at Fig. 7.6 is that for the off-stoichiometric compositions the phonon dispersion spectrum of the inverse structures should also be unstable at $c/a = 1$ because the $E(c/a)$-curves reveal a maximum at this point. A third property which can be extracted from Fig. 7.6 is the fact that the energy difference between the cubic and tetragonal distorted structure with $c/a > 1$ decreases or even changes its sign in case of the off-stoichiometric compositions. While the inverse structure still has a global minimum at $c/a > 1$ for both off-stoichiometric compositions the energy landscape is rather degenerated for the conventional structure of $Co_7NiGa_{1.25}$. In case of $Co_2Ni_{0.75}Ga_{1.25}$ the global energy minimum of the conventional structure even is situated at $c/a = 1$ while the energy curve only reveals a saddle-point like shoulder for $c/a > 1$. This means, that for the Co-Ni-Ga system a similar trend as for the Ni-Mn-Z compounds is observed, namely that tetragonal structures become preferred with increasing valence electron concentration e/a. The phase diagram plotted in Fig. 7.5 contains two dashed lines corresponding to constant e/a ratios of 7.42 and 7.75. While $e/a = 7.42$ corresponds to the value of the experimental sample, the latter value corresponds to the stoichiometric composition which favours tetragonally distorted structures. The two off-stoichiometric compositions that have been considered here have an even smaller e/a ratio as the experimental sample and lie therefore above the dashed line which corresponds to $e/a = 7.42$. The fact that the cubic structure with $c/a = 1$ becomes more preferred for these compositions is in agreement with the results for Ni-Mn-Z presented in chapter 5 where tetragonal structures become preferred, as the valence electron concentration is increased.

7.2.1 The phonon dispersion of off-stoichiometric Co-Ni-Ga

As the off-stoichiometric sample with the composition $Co_{48}Ni_{22}Ga_{30}$ which undergoes a martensitic transformation reveals no phonon softening in neutron scattering measurements, the question arises whether in the phonon dispersion curves of the off-stoichiometric compositions obtained from *ab initio* calculations, phonon softening is also absent. As it was pointed out before, imaginary phonons and thus an instability is expected for the inverse structures of $Co_2Ni_{0.75}Ga_{1.25}$ and $Co_{1.75}NiGa_{1.25}$ at $c/a = 1$ due to the curvature of the $E(c/a)$-curves at this point. The phonon calculations for the inverse structure of $Co_2Ni_{0.75}Ga_{1.25}$ verify this expectation as they reveal imaginary phonon frequencies. The phonon dispersion along the [110] direction that belongs to the inverse Heusler structure of $Co_2Ni_{0.75}Ga_{1.25}$ is contained in Fig. 7.7.

Due to the fact that the phonon dispersions for the off-stoichiometric composition have been calculated using a supercell with the respective off-stoichiometric composition, two major

differences turn up when comparing the so obtained phonon dispersion curves to the results for the stoichiometric composition Co_2NiGa. First of all the number of phonon branches is increased because of the increased number of atoms that are contained in the unit cell. At the same time the increased volume of the unit cell results in a decreased size of the Brillouin zone. In fact, the original Brillouin zone as well as the phonon branches therein are folded in case of the supercell calculations which explains the apperance of the additional phonon branches. In case of the off-stoichiometric composition it is not possible to unfold the branches without making further assumptions [219]. Instead, the measured dispersion of $Co_{48}Ni_{22}Ga_{30}$ which is depicted as squares in Fig. 7.7 has been folded in the same way as the phonon branches of the *ab initio* calculations in order to allow a reasonable comparison.

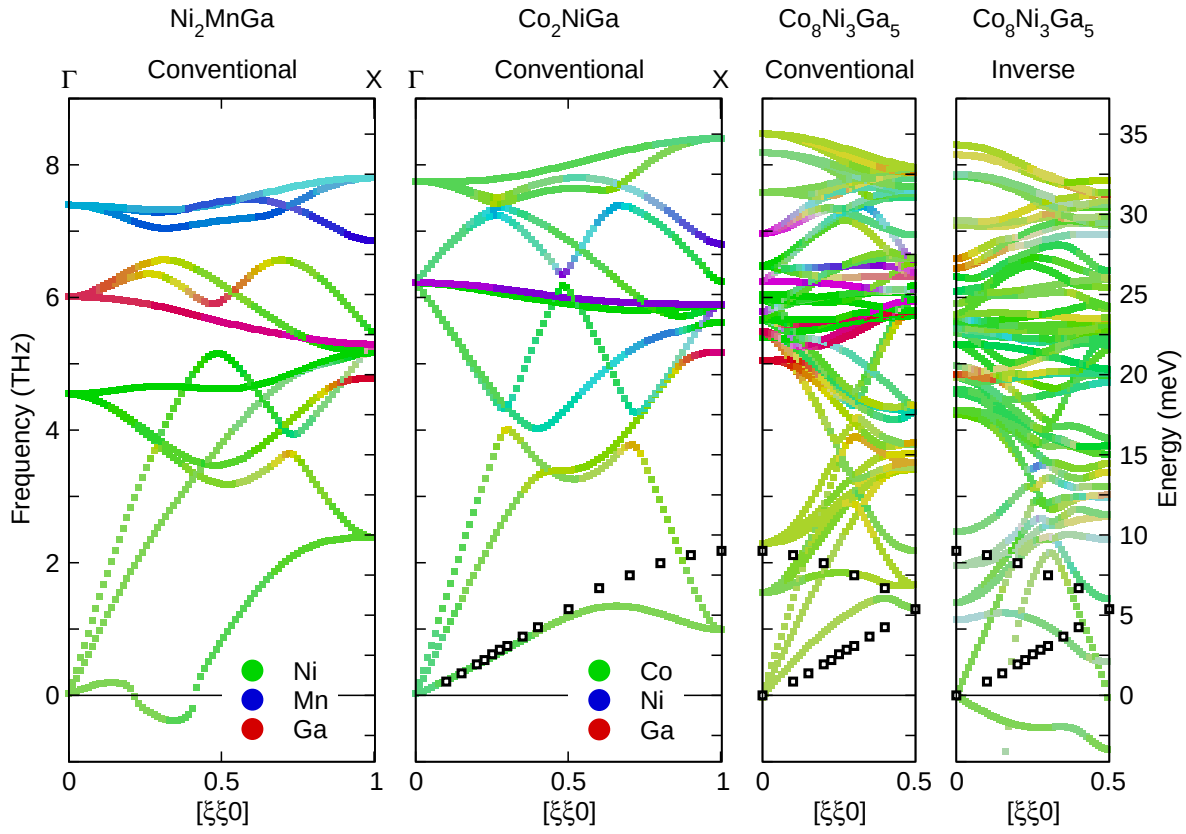

Figure 7.7: Phonon dispersion of Ni_2MnGa, Co_2NiGa, and the conventional and inverse Heusler structure of $Co_2Ni_{0.75}Ga_{1.25}$ ($Co_8Ni_3Ga_5$ supercell). along the [110] direction. The color coding represents the contribution of the different atoms to the respective phonon modes. The squares refer to neutron scattering measurements of $Co_{48}Ni_{22}Ga_{30}$. The calculations for the inverse structure have been performed by M. E. Gruner [201]. Figure adapted from Ref. [201].

In contrast to the inverse structure the conventional structure of $Co_2Ni_{0.75}Ga_{1.25}$ does not

reveal imaginary phonon frequencies as can be seen in Fig. 7.7. It is remarkable, that for this composition phonon branches at about 2 THz turn up near the point where the measured dispersion reaches this value while this was not the case for the computed dispersion of the stoichiometric composition. Since the phonon dispersion of the stoichiometric composition did not contain any optical branches in the region around 2 THz at the Γ point is is reasonable to relate the branches which turn up at the Γ in case of the conventional structure of $Co_2Ni_{0.75}Ga_{1.25}$ ($Co_8Ni_3Ga_5$ supercell) to branches which would have to be folded back in the original representation of the Brillouin zone. Hence, the addition of Ga is expected to increase the frequencies of the lowest lying acoustic branches at the zone boundary of the Brillouin zone in the unfolded original representation to values which are observed experimentally at this point. The differences that still remain between theory and experiment might on the one hand be devoted to the fact that the theoretical and experimental compositions are not equal. On the other hand it is also possible that the experimental sample is partially disorded and therefore also contains local environments of the inverse structure. One should however also keep in mind that the measurements are performed at around room temperature while the calculations refer to $T = 0\,\mathrm{K}$.

7.2.2 Electronic structure and Fermi surface of Co-Ni-Ga

It was pointed out in the previous section that, depending on the type of structure, the phonon spectrum of Co-Ni-Ga is either unstable or completely stable without any signs for phonon softening. This raises the question whether explanations for this behaviour are found when investigating the electronic structure of the respective composition since it has been shown that there is a strong correlation between the electronic and dynamical properties in other magnetic shape memory materials such as Ni_2MnGa (see chapter 4). In particular it is of interest if physical phenomena like the band Jahn-Teller effect or Fermi surface nesting which have been identified as accompanying features of the martensitic transition in other shape memory materials are also present in the Co-Ni-Ga alloys.

It turns out that not only phonon softening but also Fermi surface nesting are absent in the Co-Ni-Ga alloy system. Fig. 7.8 contains the Fermi surface for the spin-down channel of the conventional and inverse structure of Co_2NiGa. The Fermi surface of the conventional structure is plotted for two different e/a ratios which have been obtained within the rigid band approach making use of equation (5.1). It is remarkable that the area of the Fermi surface which belongs to the inverse structure is rather small compared to the areas of the other Fermi surfaces (for comparison the Fermi surface of the spin-down channel of Ni_2MnGa is also plotted in Fig. 7.8). The reduced area that belongs to the Fermi surface goes hand in hand with a small value of the electronic density of states of the inverse structure at the Fermi level (see Fig. 7.9 (c) for comparison).

The spin-down Fermi surface of the conventional structure of Co_2NiGa does not reveal planar sheets which are as pronounced as in the case of Ni_2MnGa. In fact, for the e/a ratio

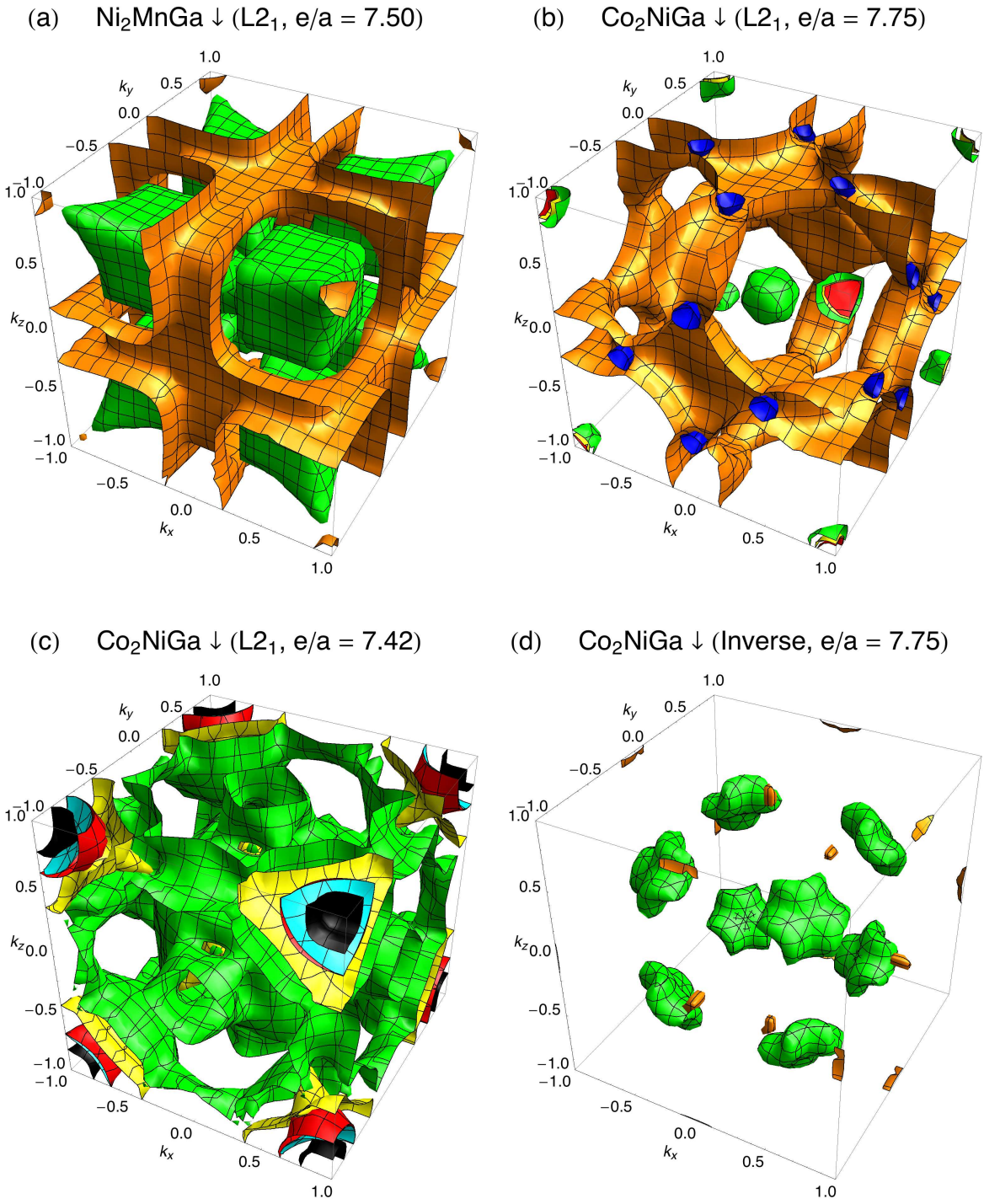

Figure 7.8: Fermi surfaces of the spin-down channel of (a) Ni_2MnGa and (b-d) Co_2NiGa. The Fermi surface of the conventional structure Co_2NiGa is plotted for two different e/a ratios within the rigid band approach, namely (b) $e/a = 7.75$ and (c) $e/a = 7.42$. The Fermi surface of the inverse structure of Co_2NiGa is plotted in (d). Adapted from Refs. [201, 92].

of the stoichiometric composition ($e/a = 7.75$) only one band is significantly contributing to the Fermi surface. For the reduced e/a ratio of the experimental composition $Co_{48}Ni_{22}Ga_{30}$ ($e/a = 7.42$) the overall area of the Fermi surface increases and is also not dominated as much by one band as for the case $e/a = 7.75$. However, at the same time the rather flat portions of the Fermi surface that still were present for $e/a = 7.75$ have totally vanished in the Fermi surface of $e/a = 7.42$. Thus, independently from the type of crystal structure or valence electron density it can be concluded that Fermi surface nesting will be weak or even absent in Co-Ni-Ga in contrast to Ni_2MnGa which is in agreement with the phonon dispersions presented previously within this chapter.

Besides Fermi surface nesting the band Jahn-Teller effect is another important phenomenon which is considered to be responsible for the appearance of the martensitic transformation in Ni_2MnGa. It therefore seems reasonable to look for signs of the band Jahn-Teller effect also in the Co-Ni-Ga alloy system. However, in contrast to Ni_2MnGa and Ni-Mn-Z in general, the densities of states of the considered compositions of Co-Ni-Ga do not reveal properties that can be explicitly linked to a band Jahn-Teller effect. In particular, no peak that is situated just below the Fermi level can be identified in the minority spin-channel of the electronic density of states of the conventional structure of Co_2NiGa which is plotted in Fig. 7.9 (a). Looking at the density of states of the $L1_0$-structure with a c/a ratio of 1.41 the number of states that can be found just below the Fermi level even has increased in the spin-down channel as is depicted in Fig. 7.9 (b). While at the same time the changes in the majority spin-channel between the two structures are small it can be concluded that at least for the conventional structure of the stoichiometric composition no band Jahn-Teller effect is observed. The same is true for the inverse structure of this composition whose density of states is plotted in Fig. 7.9 (c). Here a small pseudo-gap is found in the spin-down channel just at the Fermi level which explains the small area of the Fermi surface in Fig. 7.8 (d). However, the width of the gap is so small that it is likely to disappear at elevated temperature. Fig. 7.9 (d) contains the electronic density of states for the conventional structure of the off-stoichiometric composition $Co_2Ni_{0.75}Ga_{1.25}$. Here, the situation around the Fermi level is rather similar to the situation found for the stoichiometric composition. In particular, a pseudo-gap is situated just below the Fermi level in the spin-down channel which means that also in this case no clear signs for the band Jahn-Teller effect are present.

It should be noted that the changes that can be observed in the densities of states for the different crystal structures, c/a ratios and compositions of Co-Ni-Ga are mainly restricted to the spin-down channel in the region around the Fermi level. This can be explained by the fact that while the d-bands of the majority spin-channel are situated below the Fermi level for this type of Heusler compounds the d-bands of the minority channel are found at or even above E_F (see Fig. 7.9) due to the finite magnetic moment of the system. As the spin-up density of states is therefore not very sensitive to changes of the system it is not that surprising that the spin-up Fermi surfaces of different Heusler systems reveal a rather similar shape of the Fermi

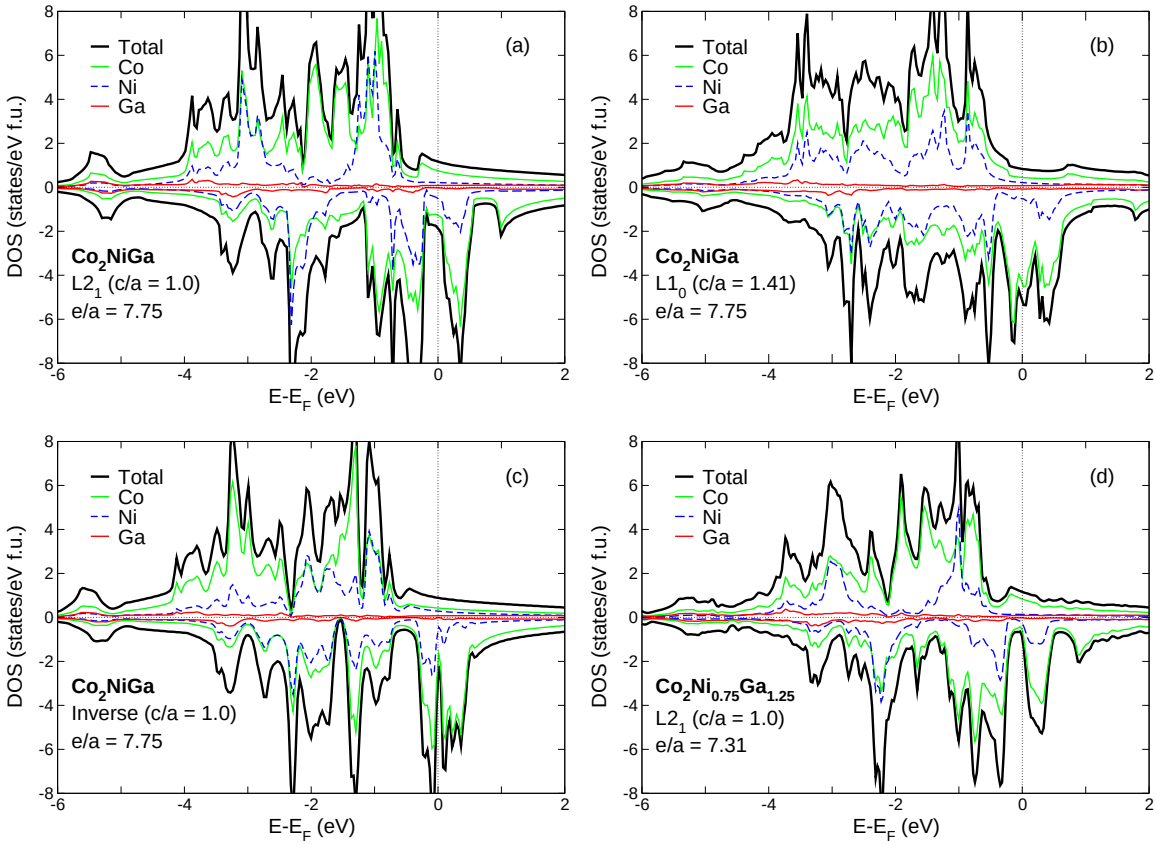

Figure 7.9: Electronic density of states of (a-c) Co_2NiGa for different crystal orderings and c/a ratios and (d) the conventional structure of $Co_2Ni_{0.75}Ga_{1.25}$. Positive values of *DOS* refer to the spin-up channel, negative values to the spin-down channel, respectively. Figure adapted from Ref. [201].

surface [212].

7.3 The influence of e/a on the tetragonal transformation in Co-Ni-Ga

So far it has turned out that the Co-Ni-Ga alloy shows a different behaviour regarding the phonon dispersion and the electronic structure as compared to the magnetic shape memory reference system Ni_2MnGa. These results suggest that the mechanism which is driving the martensitic transformation in Co-Ni-Ga is different from the case of Ni_2MnGa. In order to clarify this point the influence of the valence electron concentration on the martensitic transformation of Co-Ni-Ga will be investigated in the following as it has turned out that the change of e/a and the antiferromagnetic tendencies that arise from these changes are responsible for the change of T_M with e/a in Ni-Mn-Z (see chapter 5).

In contrast to the Mn-rich Ni-Mn-Z (Z = Ga, In, Sn, Sb) compounds nearly no antiferromagnetic interactions are present in Co-Ni-Ga according to *ab initio* investigations [220].

Table 7.1: Selected properties of the three different compositions of Co-Ni-Ga that have been considered in the evaluation of the influence of e/a on the tetragonal transformation. Besides the e/a ratio the magnetic moments for $c/a = 1$ of the conventional and inverse structure are listed. E_{Order} describes the energetic preference of the inverse structure over the conventional structure in the respective composition. Adapted from Ref. [135].

System	e/a	$\mathrm{M}_{\mathrm{Conventional}}$ (μ_{B}/f.u.)	$\mathrm{M}_{\mathrm{Inverse}}$ (μ_{B}/f.u.)	E_{Order} (meV/f.u.)
$Co_2Ni_{0.75}Ga_{1.25}$	7.31	2.15	2.79	15.4
Co_2NiGa	7.75	2.67	3.05	14.6
$Co_2Ni_{1.25}Ga_{0.75}$	8.13	2.96	3.48	91.4

Nevertheless it is still reasonable to investigate the behaviour of the tetragonal transformation as a function of e/a in a similar manner as it was done in case of the Ni-Mn-Z alloys. In case of Co-Ni-Ga three different compositions, namely $Co_2Ni_{0.75}Ga_{1.25}$ ($Co_8Ni_3Ga_5$ supercell), Co_2NiGa and $Co_2Ni_{1.25}Ga_{0.75}$ ($Co_8Ni_5Ga_3$ supercell) have been considered. Thus, instead of substituting Ga by Mn like in Ni-Mn-Ga the increase of the valence electron concentration in Co-Ni-Ga is realized by a substitution of Ga by Ni. Both types of substitution have in common that the X atoms in the Heusler formula unit X_2YZ are not affected by the substitution and that high valence electron concentrations are obtained for systems containing less Ga in both cases. This type of substitution is different from the substitution with constant Ga ratio that has been studied by Sarma and Srinivasan [221]. As in the latter case an increase of M_{S} with e/a was observed experimentally, the question arises whether the same also is true for compositions with constant Co ratio.

For both types of crystal structure the addition of Ni increases the total magnetic moment M. The increase of M with e/a is in contrast to the behaviour which is observed in Ni-Mn-Z and another indicator for the fact that antiferromagnetic tendencies are more or less absent in Co-Ni-Ga. The magnetic moments for all considered compositions are also listed in table 7.1. Another interesting aspect that appears upon the addition of Ni is the strong preference for the inverse structure at $c/a = 1$. Table 7.1 contains composition-dependent values of a variable denoted as E_{Order} which is defined as

$$E_{\mathrm{Order}} = E_{\mathrm{Conventional}}(c/a = 1) - E_{\mathrm{Inverse}}(c/a = 1). \tag{7.1}$$

While E_{Order} is small and also does not change significantly in the e/a interval between 7.31 and 7.75 it significantly increases by a factor of about 6 for $e/a = 8.13$. This means that at the respective composition a pronounced energetic preference of the inverse structure appears at $c/a = 1$.

In agreement with the results obtained for Ni-Mn-Z and also for the Pt-rich systems the

preference of tetragonal transformations at low temperatures increases with e/a in case of the Co-Ni-Ga compound. The behaviour of the structural energy difference ΔE upon the variation of the valence electron concentration e/a is plotted in Fig. 7.10. In particular ΔE refers to the energy difference between the cubic structure with $c/a = 1$ and the tetragonal structure with $c/a > 1$ which corresponds to the global minimum of the $E(c/a)$-curve (see Fig. 4.6 (a) for a schematic representation of ΔE). For both, the regular Heusler as well as the inverse structure an increase of ΔE with e/a is observed. However, while this increase is nearly linear for the regular structure, a non-linear behaviour is found in case of the inverse structure. While at the same time the energy differences are always larger for the inverse structure, the absolute value of ΔE nearly becomes equal for both structures at $e/a = 8.19$. It should be noted here that the structural energy differences have been obtained by taking into account different atomic configurations as well as atomic relaxations as has been described in section 7.2.

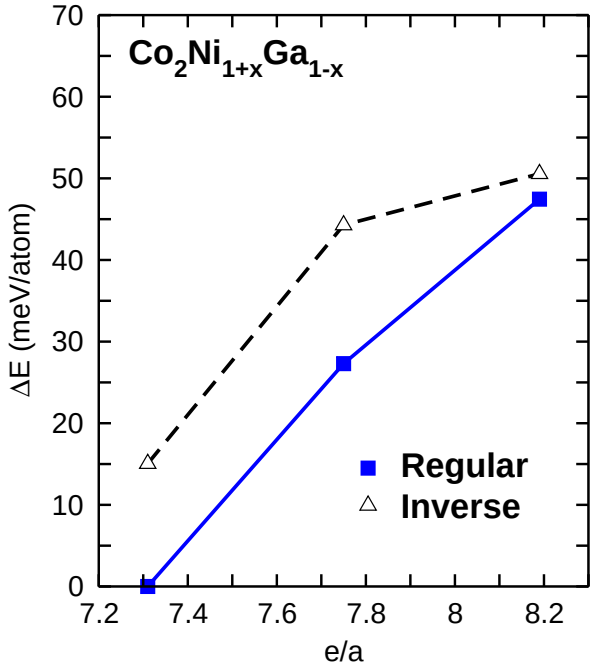

Figure 7.10: Evolution of the energy difference ΔE between the cubic structure ($c/a = 1$) associated with the austenite structure and the tetragonal structure ($c/a > 1$) which reveals a minimum in the $E(c/a)$-curve as a function of the valence electron concentration e/a for the alloy series $Co_2Ni_{1+x}Ga_{1-x}$ ($-0.25 \leq x \leq 0.25$). The calculations were carried out at constant volumes of the respective cubic structures. Figure adapted from Ref. [135].

The results presented in Fig. 7.10 suggest that in the case of Co-Ni-Ga an increase of T_M is also expected for increasing e/a values from a theoretical point of view in agreement with the observations for Ni-Mn-Z ($Z =$ Ga, In, Sn, Sb). Although it seems to be remarkable that such a

behaviour is observed in the Co-Ni-Ga compound where antiferromagnetic interactions, which have been identified as a main driving force of the stabilization of the martensite structure in the Ni-based alloys in chapter 5, are absent, such behaviour is also known from Ni-Fe-Ga [222]. At the same time the observed behaviour also fits into the trend of decreasing lattice constants with increasing martensitic transformation temperatures which has been observed for $Ni_{2+x}Mn_{1-x}Ga$ [184].

The fact that tetragonal transformations become energetically preferred with increasing valence electron concentration however does not guarantee that Co-Ni-Ga is a candidate for industrial applications of the magnetic shape memory effect. In fact, the structural energy differences that are obtained for large e/a ratios are in the same range as the energy differences which are obtained for compositions of Ni-Mn-Z with a similar e/a ratio. At the same time, however, the $E(c/a)$-curves of Co-Ni-Ga reveal that the martensite structure at $c/a > 1$ appears at rather high c/a ratios which can be associated with a fct-phase. These results can be related to the ternary phase diagram which is plotted in Fig. 7.5. Looking at the phase diagram it becomes evident that an increase of the e/a ratio shifts the system towards the γ-phase which has an fcc-type structure. Although this phase is not suitable for the magnetic shape memory effect the results obtained using *ab initio* calculations suggest that tetragonal structures which are of interest with regard to the magnetic shape memory effect can nevertheless still be obtained for certain compositions of Co-Ni-Ga.

7.4 Conclusion

The investigation of the Co-Ni-Ga compound shows that the situation that is present in the Ni-Mn-Z compounds and especially in Ni_2MnGa is not a necessary prerequisite for the appearance of the magnetic shape memory effect. While the $E(c/a)$-curves of different compositions of Co-Ni-Ga look rather similar to the respective curves of the Ni-Mn-Z alloys which undergo a martensitic transformation, phenomena like Fermi surface nesting or the band Jahn-Teller effect are not observed in the Co-Ni-Ga system. A second difference between the two material classes turns up when looking at the stability of different crystal structures. While at low temperatures the conventional structure clearly is favoured in Ni_2MnGa the situation is rather diffuse in Co-Ni-Ga due to the competition between the conventional and inverse structure which are found in the same energy region for a wide range of compositions. A recent theoretical investigation on Co_2NiGa taking into account the partially-ordered B2-structure (see Fig. 3.4 for a comparison of the B2- and $L2_1$-structure) revealed that this structure is not favoured over the two other structures in Co_2NiGa [211]. Therefore, a completely disordered structure is likely to be expected in agreement with experimental results [199].

The results of the calculation of off-stoichiometric phonon dispersions which are presented in section 7.2.1 give further evidence for the assumption of the preference of a totally disordered crystal structure. While no phonon softening and instabilities are found in case of

the conventional structure in agreement with results from neutron scattering measurements the $E(c/a)$-curves reveal that only the inverse structure should undergo a martensitic transformation at the respective composition. However, the phonons of the inverse structure are dynamically unstable and reveal imaginary phonon frequencies while no signs for phonon softening are observed in the experiment.

The investigation of the behaviour of the structural energy differences as a function of the valence electron concentration reveals a rather similar behaviour as found in Ni-Mn-Z. The energy difference between the austenite and martensite structure increases for compositions with increased e/a ratio. However, while the increase of the martensitic transformation temperature was related to the appearance of antiferromagnetic tendencies in Ni-Mn-Z such tendencies are absent in Co-Ni-Ga [220].

Thus, although the observed transformation temperatures are not as high as in Ni_2MnGa the Co-Ni-Ga system is at least of theoretical interest as it is a system which undergoes a martensitic transformation while at the same time no signs for Fermi surface nesting or the band Jahn-Teller effect are found and also the type of magnetic interaction is different from the one that is present in the Ni_2MnGa reference system. The absence of these effects might be explained by the preference of disorder which itself may be related to the similarities between Co and Ni. Both elements are not only ferromagnetic but differ only by one proton (and accordingly by one valence electron) from each other and nearly have the same mass. [2]

[2] Actually the atomic number of Co is smaller than that of Ni while the mass number of Co (58.9332) is larger than that of Ni (58.6934).

Chapter 8

Conclusion

In this work the electronic, magnetic, and thermodynamic properties of magnetic shape memory alloys have been investigated using first-principles calculations. The investigation focused on Heusler alloys starting from the well known ferromagnetic shape memory alloy Ni_2MnGa. The martensitic phase transformation which is observed in this compound has been investigated in detail by looking at the structural stability of the different phases and considering magnetic excitations and lattice vibrations. In this context it has been shown that the lattice entropy stabilizes the austenite structure at finite temperatures while the martensite structure is stabilized by magnetism. The investigation of the influence of electronic correlations in Ni_2MnGa reveals that the onset of a Hubbard U strongly influences the results. As however no definite trend is observed for different values of U the size of the Coulomb interaction needs to be chosen very carefully. The investigation of Fermi surface nesting effects in Ni_2MnGa by the calculation of the generalized susceptibility $\chi(\mathbf{q})$ suggests that the phonon softening which appears in the alloy is not solely driven by the Fermi surface nesting. Also, both Fermi surfaces (spin-up and spin-down channel) contribute to the nesting.

A second part of this work concentrated on the alloy series Ni-Mn-Z ($Z =$ Ga, In, Sn, Sb) and especially the Mn-rich site of the phase diagram. It is shown that a simple approach which relates the structural energy difference between the cubic and tetragonal structure to the structural transition temperature gives feasible results when compared to experimental measurements. The increase of the transformation temperature with increasing e/a is devoted to the appearance of antiferromagnetic alignments of Mn spins which are observed for Mn-rich compositions. An increased preference for tetragonal transformations and a reduction of the magnetic moment is also observed when increasing the valence electron concentration by changing the number of electrons that are considered in the *ab initio* calculations.

In the third part of this thesis the influence of the isoelectronic substitution of Ni by Pt was studied for Ni-Pt-Mn-Z ($Z =$ Ga, Sn). It turned out that the addition of platinum increases the energy difference between the cubic austenite and tetragonal martensite structure which means that higher transformation temperatures are expected compared to the compounds without Pt. Moreover, a similar relationship between the modulated 14M-structure and the tetragonal $L1_0$-structure as in Ni_2MnGa as well as signs of Fermi surface nesting are observed in the Pt-rich alloys. A calculation of the transformation temperatures for different off-stoichiometric compositions revealed that T_M increases linearly with the valence electron concentration e/a just as is the case in Ni-Mn-Z. Thus, it is expected that the addition of Pt may result

in ferromagnetic shape memory alloys which are relevant for industrial applications. These findings are underlined by recent experimental observations [197, 176].

The last part of this work focused on the ferromagnetic shape memory system Co-Ni-Ga which is of interest as disordered structures are observed experimentally for a wide range of compositions including the stoichiometric case Co_2NiGa [69, 199]. In agreement with these experimental findings the *ab initio* calculations reveal a competition between two different kinds of structures which are the conventional and inverse Heusler struture. As a neutron scattering measurement on an off-stoichiometric composition which transformed martensitically did not reveal any signs for phonon softening as observed in Ni_2MnGa the phonons for stoichiometric and off-stoichiometric compositions near the composition of the experimental sample have been calculated. It turns out that the stability of the phonon spectrum depends on the type of crystal structure. As no clear signs of Fermi surface nesting and the band Jahn-Teller are present in the material, the driving forces of the martensitic transformation are different compared to Ni_2MnGa. The basic trend that the energetic preference of the tetragonal martensite structure increases with increasing valence electron concentration is however also present in Co-Ni-Ga.

Chapter 9

Outlook

In this thesis different types of alloy systems were investigated with regard to their electronic, magnetic, and thermodynamic properties using first-principles calculations. The results that have been obtained give rise to a better understanding of the different martensitic driving forces. However, because of the complexity of the research field there still remain unsolved problems like for example the formation of modulated structures or the size of the electron phonon coupling matrix elements. Some of these problems have not been approached yet as they require huge computational demand or methods which have not yet been implemented in common density functional theory codes. The following chapter will contain a brief outlook pointing out two specific issues which arise from the topic that has been discussed within this thesis and which should be addressed in the future in order to further extend the understanding of magnetic shape memory alloys.

9.1 Magnetic excitations

It was already pointed out in the discussion of the obtained transformation temperatures for Mn-rich compositions of Ni_2MnZ ($Z =$ Ga, In, Sn, Sb) that the considered collinear alignments of the magnetic spins may be not sufficient for a realistic description of the physics within the materials. In particular, the neglect of non-collinear alignments might explain the deviations that are observed when comparing first-principles results to experimental measurements. The complex magnetic order which arises from the onset of antiferromagnetism in Mn-rich compositions when considering collinear alignments gives rise to the assumption that by considering non-collinear magnetic alignments an even more complex structure is found to be the ground state. As non-collinear magnetic calculations are however computationally very demanding it might be more effective to consider non-collinear alignment of spins by calculating magnon dispersion spectra. Fig. 9.1 shows the magnon dispersions of Ni_2MnZ ($Z =$ Ga, In, Sn, Sb) which have been calculated by A. Ernst within the KKR approach [125, 126, 127]. It is clearly visible that the different Z atoms have an influence on the energy of the optical magnon branches but also on the acoustic branch. As was already mentioned in chapter 4 the magnetic entropy can be derived from the magnon spectrum in a similar manner as the lattice entropy is obtained from the phonon spectrum of the system. A detailed investigation of the magnetic contribution to the free energy for different compositions of Ni_2MnZ ($Z =$ Ga, In, Sn, Sb) would be of particular interest especially as disordered compositions can be treated within the coherent

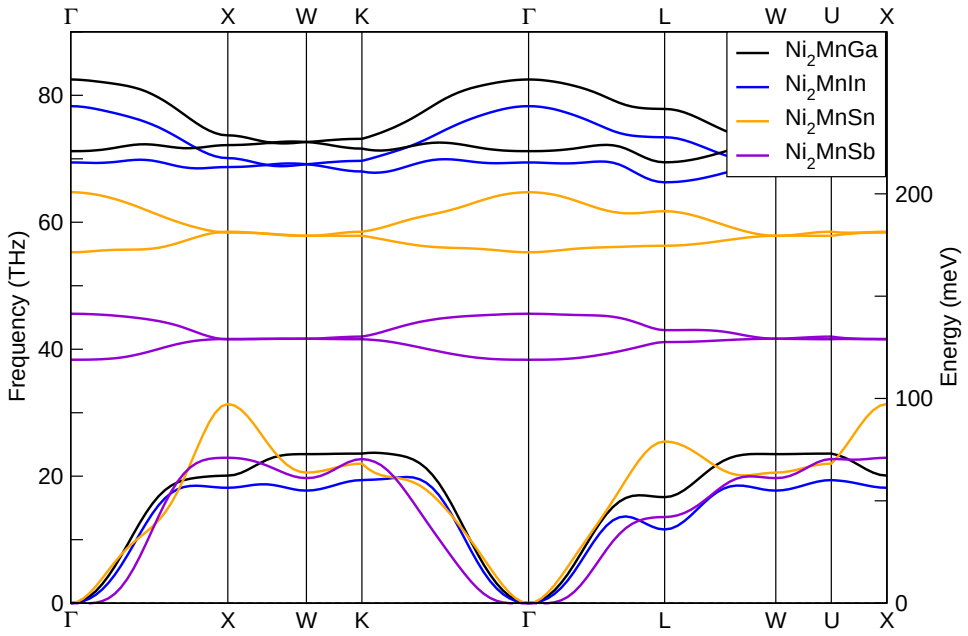

Figure 9.1: Magnon dispersion spectra of Ni_2MnZ ($Z =$ Ga, In, Sn, Sb) calculated by A. Ernst [127].

potential approximation (CPA) within the KKR approach [223].

9.2 Hexagonal transformations of Heusler compounds

While for Ni_2MnGa the different crystallograpic structures that appear for different temperatures and compositions are well known the situation is different in the alloys containing Pt and also in Co-Ni-Ga. While the former one has not been studied as comprehensively as Ni_2MnGa in literature yet the latter one is known to reveal different types of ordering depending on the sample preparation. A recent first-principles investigation revealed that for Pt_2MnGa as well as Co_2NiGa another transformation path beside the Bain path is of interest. This path which parametrizes the transformation from a bcc to a hcp structure using one parameter was investigated in 2008 by Friák *et al.* for the case of iron [224].

Fig. 9.2 shows the results that have been obtained by applying the introduced path to (a) Ni_2MnGa, Pt_2MnGa, and (b) the conventional and inverse structure of Co_2NiGa. Here, $\delta = 0$ corresponds to the bcc-structure whereas $\delta = 1$ corresponds to the hcp-structure and an energy value of zero refers to the energy of the conventional structure of the respective compound at $\delta = 0$. It is clearly visible that the bcc-hcp transformation path which has been considered here is not favoured by Ni_2MnGa although a shallow local minimum appears at $\delta \approx 0.65$. In case of Pt_2MnGa the situation is different as a global minimum of the total energy is obtained for $\delta \approx 0.7$, cf. Fig. 9.2 (a). It is remarkable that the transformation from the bcc-structure with $\delta = 0$ to the global minimum is not seperated by an energy barrier.

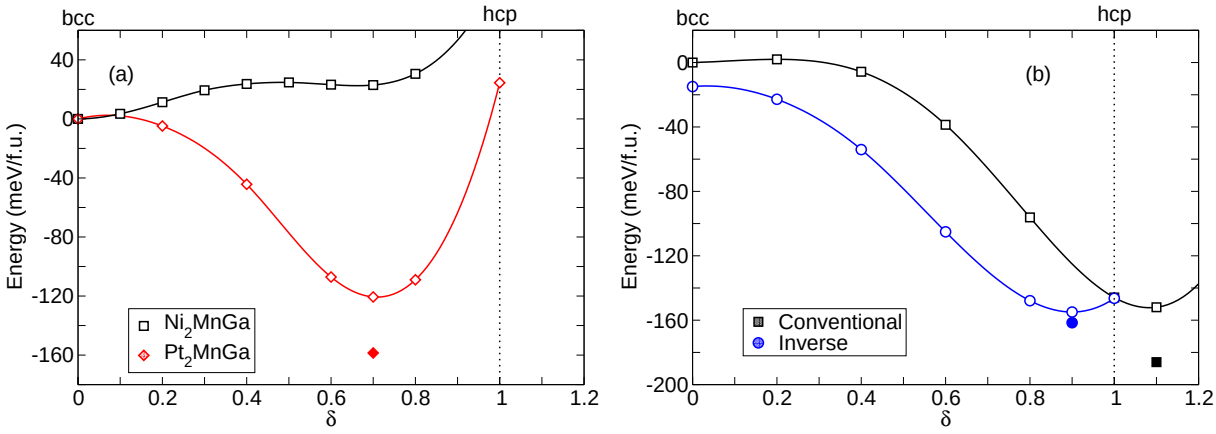

Figure 9.2: The bcc-hcp transformation path defined by the parameter δ for (a) Ni_2MnGa, Pt_2MnGa, and (b) the conventional and inverse structure of Co_2NiGa. The filled symbols denote points where the crystal cell vectors as well as the atomic positions and the volume have been relaxed using a conjugate gradient algorithm [179]. Open symbols refer to crystal structures defined by the bcc-hcp transformation path which is given in Ref. [224].

However, the energy difference between the bcc-structure and the energy minimum amounts to 121 meV/f.u. and is therefore not as large as the difference between the $L2_1$- and the $L1_0$-structure in this compound (239 meV/f.u.). Although a relaxation of the crystal cell vectors and atomic positions at $\delta = 0.7$ increases the energy difference compared to the bcc-structure even further to 159 meV/f.u. the $L1_0$-structure clearly still is predicted to be the ground state from the calculations that have been performed within this thesis.

The effect of the bcc-hcp transformation on the total energy of the conventional and inverse structure of Co_2NiGa is plotted in Fig. 9.2 (b). Similar to the situation in Pt_2MnGa the energy for both crystal structures is lowered without passing an energy barrier. At the same time the energy difference between the bcc-structure and the minimum on the hcp-side of the curve is even higher than the energy difference between the $L2_1$-structure and the $L1_0$-structure in case of the conventional structure (152 meV/f.u.). In case of the inverse structure this is not the fact for the energy minimum at the hcp-side without relaxations. If one allows for relaxation of the atomic positions, the crystal cell vectors, and the volume one finds that the energy difference is even further increased, especially in case of the conventional structure. The energy difference between the conventional bcc and the relaxed near-hcp structure now amounts to 186 meV/f.u. (conventional) and 162 meV/f.u. (inverse). Thus, the energy value of the relaxed near-hcp structure which belongs to the conventional ordering is nearly as low as the energy value of the inverse $L1_0$-structure which is expected to be the ground state of Co_2NiGa. The energy difference between the latter structure and the conventional bcc structure is 192 meV/f.u., cf. Fig. 7.2 (a). This means that hcp-like structures have to be

considered in further investigations of this material.

The investigation of the bcc-hcp transformation of Heusler structures give rise to the idea that the transformation which goes hand in hand with a shuffling of atomic layers within the crystal may explain the mechanism that is responsible for the forming of the modulated structures. However, maybe the preference for a bcc-hcp transformation in Pt_2MnGa and Co_2NiGa also hinders the appearance of the magnetic shape memory effect as it is not clear whether the change of structure can be associated with a martensitic transformation. In this context it should be reminded that Ni_2MnGa which shows feasible magnetic shape memory properties does not favour a bcc-hcp transformation. Therefore, this issue requires further investigation.

Bibliography

[1] R. Meyer, *Molekulardynamiksimulation und Dichtefunktionaltheorie*, Lecture, University of Duisburg-Essen (2006-2007).

[2] R. M. Martin, *Electronic Structure - Basic Theory and Practical Methods*, Cambridge University Press 2004.

[3] M. Siewert, *Ab-Initio Untersuchungen der strukturellen, dynamischen und elektronischen Eigenschaften magnetischer Formgedächtnis-Systeme*, Master's thesis, University of Duisburg-Essen 2008.

[4] L. H. Thomas, *The Calculation of Atomic Fields*, Proc. Camb. Phil. Soc. **23**, 542–548 (1927).

[5] P. Hohenberg and W. Kohn, *Inhomogeneous Electron Gas*, Phys. Rev. **B 136**, B864–B871 (1964).

[6] W. Kohn and L. J. Sham, *Self-Consistent Equations Including Exchange and Correlation Effects*, Phys. Rev. **140**, A1133–A1138 (Nov 1965).

[7] J. P. Perdew and A. Zunger, *Self-interaction correction to density-functional approximations for many-electron systems*, Phys. Rev. B **23**, 5048–5079 (May 1981).

[8] D. M. Ceperley and B. J. Alder, *Ground State of the Elextron Gas by a Stochastic Method*, Phys. Rev. Lett. **45**, 566–569 (1980).

[9] D. C. Langreth and M. J. Mehl, *Beyond the local-density approximation in calculations of ground-state electronic properties*, Phys. Rev. B **28**, 1809–1834 (Aug 1983).

[10] A. D. Becke, *Density-functional exchange-energy approximation with correct asymptotic behavior*, Phys. Rev. A **38**, 3098–3100 (Sep 1988).

[11] J. P. Perdew, J. A. Chevary, S. H. Vosko, K. A. Jackson, M. R. Pederson, D. J. Singh and C. Fiolhais, *Atoms, molecules, solids, and surfaces: Applications of the generalized gradient approximation for exchange and correlation*, Phys. Rev. B **46**, 6671–6687 (Sep 1992).

[12] J. P. Perdew, J. A. Chevary, S. H. Vosko, K. A. Jackson, M. R. Pederson, D. J. Singh and C. Fiolhais, *Erratum: Atoms, molecules, solids, and surfaces: Applications of the generalized gradient approximation for exchange and correlation*, Phys. Rev. B **48**, 4978–4978 (Aug 1993).

[13] J. Perdew, *Electronic Structure of Solids '91 edited by P Ziesche and H Eschrig*, pp. 11–20, Akademie Verlag, Berlin (1991).

[14] J. P. Perdew, K. Burke and M. Ernzerhof, *Generalized Gradient Approximation Made Simple*, Phys. Rev. Lett. **77**, 3865–3868 (1996).

[15] A. Janotti and C. G. Van de Walle, *LDA+U and Hybrid Functional Calculations for Defects in ZnO, SnO_2, and TiO_2*, chap. 9, Advanced Calculations for Defects in Materials: Electronic Structure Methods, Wiley-VCH Weinheim (2011).

[16] F. Aryasetiawan, S. Biermann and A. Georges, *A First-Principles Scheme for Calculating the Electronic Structure of Strongly Correlated Materials: GW+DMFT*, chap. 1, pp. 1–16, Correlation Spectroscopy of Surfaces, Thin Films, and Nanostructures, Wiley-VCH Weinheim (2004).

[17] R. C. Albers, N. E. Christensen and A. Svane, *Hubbard-U band-structure methods*, J. Phys.: Condens. Matter **21**, 343201 (2009).

[18] J. Kohanoff, *Electronic Structure Calculations for Solids and Molecules: Theory And Computational Methods*, Cambridge University Press 2006.

[19] J. Hubbard, *Electron Correlations in Narrow Energy Bands*, Proc. R. Soc. Lond. A **276**, 238–257 (1963).

[20] V. I. Anisimov, J. Zaanen and O. K. Andersen, *Band theory and Mott insulators: Hubbard U instead of Stoner I*, Phys. Rev. B **44**, 943–954 (Jul 1991).

[21] V. I. Anisimov, I. V. Solovyev, M. A. Korotin, M. T. Czyżyk and G. A. Sawatzky, *Density-functional theory and NiO photoemission spectra*, Phys. Rev. B **48**, 16929–16934 (Dec 1993).

[22] A. I. Liechtenstein, V. I. Anisimov and J. Zaanen, *Density-functional theory and strong interactions: Orbital ordering in Mott-Hubbard insulators*, Phys. Rev. B **52**, R5467–R5470 (Aug 1995).

[23] V. I. Anisimov, F. Aryasetiawan and A. I. Lichtenstein, *First-principles calculations of the electronic structure and spectra of strongly correlated systems: the LDA+U method*, J. Phys.: Condens. Matter **9**, 767–808 (1997).

[24] V. I. Anisimov and O. Gunnarsson, *Density-functional calculation of effective Coulomb interactions in metals*, Phys. Rev. B **43**, 7570–7574 (Apr 1991).

[25] S. L. Dudarev, G. A. Botton, S. Y. Savrasov, C. J. Humphreys and A. P. Sutton, *Electron-energy-loss spectra and the structural stability of nickel oxide: An LSDA+U study*, Phys. Rev. B **57**, 1505–1509 (Jan 1998).

[26] S. Hüfner and G. K. Wertheim, *Estimates of the Coulomb Correlation Energy from X-Ray Photoemission Data*, Phys. Rev. B **7**, 5086–5090 (Jun 1973).

[27] T. O. Wehling, E. Şaşıoğlu, C. Friedrich, A. I. Lichtenstein, M. I. Katsnelson and S. Blügel, *Strength of Effective Coulomb Interactions in Graphene and Graphite*, Phys. Rev. Lett. **106**, 236805 (Jun 2011).

[28] E. Şaşıoğlu, C. Friedrich and S. Blügel, *Effective Coulomb interaction in transition metals from constrained random-phase approximation*, Phys. Rev. B **83**, 121101 (Mar 2011).

[29] I. V. Solovyev, P. H. Dederichs and V. I. Anisimov, *Corrected atomic limit in the local-density approximation and the electronic structure of d impurities in Rb*, Phys. Rev. B **50**, 16861–16871 (Dec 1994).

[30] T. Bandyopadhyay and D. D. Sarma, *Calculation of Coulomb interaction strengths for 3 d transition metals and actinides*, Phys. Rev. B **39**, 3517–3521 (Feb 1989).

[31] P. Schwerdtfeger, *The Pseudopotential Approximation in Electronic Structure Theory*, ChemPhysChem **12**, 3143–3155 (2011).

[32] C. Herring, *A new method for calculating wave functions in crystals*, Phys. Rev. **57**, 1169–1177 (1940).

[33] C. Herring and A. G. Hill, *The Theoretical Constitution of Metallic Beryllium*, Phys. Rev. **58**, 132–162 (1940).

[34] D. Vanderbilt, *Soft self-consistent pseudopotentials in a generalized eigenvalue formalism*, Phys. Rev. B **41**, 7892–7895 (1990).

[35] P. E. Blöchl, *Projector augmented-wave method*, Phys. Rev. B **50**, 17953 (1994).

[36] P. Giannozzi, S. Baroni, N. Bonini, M. Calandra, R. Car, C. Cavazzoni, D. Ceresoli, G. L. Chiarotti, M. Cococcioni, I. Dabo, A. Dal Corso, S. de Gironcoli, S. Fabris, G. Fratesi, R. Gebauer, U. Gerstmann, C. Gougoussis, A. Kokalj, M. Lazzeri, L. Martin-Samos, N. Marzari, F. Mauri, R. Mazzarello, S. Paolini, A. Pasquarello, L. Paulatto, C. Sbraccia, S. Scandolo, G. Sclauzero, A. P. Seitsonen, A. Smogunov, P. Umari and R. M. Wentzcovitch, *QUANTUM ESPRESSO: a modular and open-source software project for quantum simulations of materials*, Journal of Physics: Condensed Matter **21**, 395502 (19pp) (2009).

[37] G. Kresse and J. Furthmüller, *Efficient iterative schemes for ab initio total-energy calculations using a plane-wave basis set*, Phys. Rev. B **54**, 11169 (1996).

[38] G. Kresse and D. Joubert, *From ultrasoft pseudopotentials to the projector augmented-wave method*, Phys. Rev. B **59**, 1758 (1999).

[39] J. R. Christman, *Fundamentals of Solid State Physics*, John Wiley & Sons 1988.

[40] H. Ibach and H. Lüth, *Festkörperphysik - Eine Einführung in die Grundlagen*, Springer-Verlag 1981.

[41] K.-H. Hellwege, *Einführung in die Festkörperphysik, 3. korr. Auflage*, Springer-Verlag 1988.

[42] H. Hellmann, *Einführung in die Quantenchemie*, Franz Deuticke, Leipzig-Wien 1937.

[43] R. P. Feynman, *Forces in Molecules*, Phys. Rev. **56**, 340–343 (Aug 1939).

[44] D. Alfè, *PHON: A program to calculate phonons using the small displacement method*, Computer Physics Communications **180**, 2622–2633 (2009).

[45] K. Parlinski, Z. Q. Li and Y. Kawazoe, *First-Principles Determination of the Soft Mode in Cubic* ZrO_2, Phys. Rev. Lett. **78**, 4063–4066 (May 1997).

[46] P. Entel, D. Comtesse, H. C. Herper, M. E. Gruner, M. Siewert, S. Sahoo and A. Hucht, *Ab-initio modeling of Fe-Mn based alloys and nanoclusters*, MRS Proceedings **1296**, mrsf10–1296–o04–01 (2010).

[47] C. Kittel, *Einführung in die Festkörperphysik, 14.überarb. und erw. Aufl.*, Oldenbourg Verlag 2006.

[48] P. W. Anderson, *Theory of Magnetic Exchange Interactions: Exchange in Insulators and Semiconductors*, vol. 14 of *Solid State Physics Advances in Research and Applications*, pp. 99–214, Academic Press (1963).

[49] L. Landau and E. Lifshitz, *On the theory of the dispersion of magnetic permeability in ferromagnetic bodies*, Phys. Zeitsch. der Sowjetunion **8**, 153–169 (1935).

[50] T. L. Gilbert, *A phenomenological theory of damping in ferromagnetic materials*, IEEE Trans. Magn. **40**, 3443–3449 (2004).

[51] L. Delaey, *Diffusionless Transformations*, vol. 5 (Phase Transformations in Materials) of *Materials Science and Technology*, chap. 6, pp. 339–404, VCH, Weinheim (1991).

[52] K. Otsuka and C. M. Wayman, *Introduction*, chap. 1, pp. 1–26, Shape Memory Materials, Cambridge University Press (1998).

[53] W. Kohn, *Image of the Fermi Surface in the Vibration Spectrum of a Metal*, Phys. Rev. Lett. **2**, 393–394 (May 1959).

[54] P. M. Ossi and F. Rossitto, *Phase stability and martensitic transformation in metals and alloys*, J. Phys. F: Metal Phys. **11**, 2037–2043 (1981).

[55] P. K. Kumar and D. C. Lagoudas, *Introduction to Shape Memory Alloys*, chap. 1, pp. 1–51, Shape Memory Alloys, Springer Science+Business Media, New York (2008).

[56] K. Otsuka and C. M. Wayman, *Mechanism of shape memory effect and superelasticity*, chap. 2, pp. 27–48, Shape Memory Materials, Cambridge University Press (1998).

[57] J. R. Patel and M. Cohen, *Criterion for the action of applied stress in the martensitic transformation*, Acta Metallurgica **1**, 531–538 (1953).

[58] A. A. Cherechukin, I. E. Dikshtein, D. I. Ermakov, A. V. Glebov, V. V. Koledov, D. A. Kosolapov, V. G. Shavrov, A. A. Tulaikova, E. P. Krasnoperov and T. Takagi, *Shape memory effect due to magnetic field-induced thermoelastic martensitic transformation in polycrystalline Ni-Mn-Fe-Ga alloy*, Phys. Lett. A **291**, 175–183 (2001).

[59] J. Enkovaara, A. Ayuela, L. Nordström and R. M. Nieminen, *Magnetic anisotropy in Ni_2MnGa*, Phys. Rev. B **65**, 134422 (Mar 2002).

[60] R. D. James and K. F. Hane, *Martensitic transformations and shape-memory materials*, Acta Materialia **48**, 197–222 (2000).

[61] K. Ullakko, J. K. Huang, V. V. Kokorin and R. C. O'Handley, *Magnetically controlled shape memory effect in Ni_2MnGa intermetallics*, Scripta Materialia **36**, 1133–1138 (1997).

[62] K. Ullakko, *Magnetically controlled shape memory alloys: A new class of actuator materials*, Journal of Mater. Eng. and Performance **5**, 405–409 (1996).

[63] A. N. Vasilev, V. D. Buchelnikov, T. Takagi, V. V. Khovailo and E. I. Éstrin, *Shape memory ferromagnets*, Physics Uspekhi **46**, 559–588 (2003).

[64] S. Fujii, S. Ishida and S. Asano, *Electronic Structure and Lattice Transformation in Ni_2MnGa and Co_2NbSn*, Journal of the Physical Society of Japan **58**, 3657–3665 (1989).

[65] A. Sozinov, A. A. Likhachev, N. Lanska and K. Ullakko, *Giant magnetic-field-induced strain in NiMnGa seven-layered martensitic phase*, Appl. Phys. Lett. **80**, 1746 (2002).

[66] T. Kakeshita and T. Fukuda, *Giant Magnetostriction in Fe_3Pt and FePd Ferromagnetic Shape-Memory Alloys*, Materials Science Forum **394-395**, 531–536 (2002).

[67] J. Buschbeck, I. Opahle, M. Richter, U. K. Rößler, P. Klaer, M. Kallmayer, H. J. Elmers, G. Jakob, L. Schultz and S. Fähler, *Full Tunability of Strain along the fcc-bcc Bain Path in Epitaxial Films and Consequences for Magnetic Properties*, Phys. Rev. Lett. **103**, 216101 (Nov 2009).

[68] K. Oikawa, L. Wulff, T. Iijima, F. Gejima, T. Ohmori, A. Fujita, K. Fukamichi, R. Kainuma and K. Ishida, *Promising ferromagnetic Ni-Co-Al shape memory alloy system*, Appl. Phys. Lett. **79**, 3290 (2001).

[69] K. Oikawa, T. Ota, F. Gejima, T. Ohmori, R. Kainuma and K. Ishida, *Phase Equilibria and Phase Transformations in New B2-type Ferromagnetic Shape Memory Alloys of Co-Ni-Ga and Co-Ni-Al Systems*, Materials Transaction **42**, 2472–2475 (2001).

[70] M. Wuttig, J. Li and C. Craciunescu, *A new ferromagnetic shape memory alloy system*, Scripta Materialia **44**, 2393–2397 (2001).

[71] P. J. Brown, K. Ishida, R. Kainuma, T. Kanomata, K.-U. Neumann, K. Oikawa, B. Ouladdiaf and K. R. A. Ziebeck, *Crystal structures and phase transitions in ferromagnetic shape memory alloys based on Co-Ni-Al and Co-Ni-Ga*, Journal of Physics: Condensed Matter **17**, 1301 (2005).

[72] T. Kushima, K. Tsuchiya, Y. Murakami, D. Shindo, Y. Todaka and M. Umemoto, *Phase Transformation and Magnetic Properties of Ferromagnetic Cu-Mn-Ga Alloys*, Materials Transaction **48**, 2840–2846 (2007).

[73] H. E. Karaca, I. Karaman, B. Basaran, Y. Ren, Y. I. Chumlyakov and H. J. Maier, *Magnetic Field-Induced Phase Transformation in NiMnCoIn Magnetic Shape-Memory Alloys - A New Actuation Mechanism with Large Work Output*, Advanced Functional Materials **19**, 983 (2009).

[74] T. Kakeshita, K. Shimizu, T. Maki, I. Tamura, S. Kijima and M. Date, *Magnetoelastic martensitic transformation in an ausaged Fe Ni Co Ti alloy*, Scripta Metallurgica **19**, 973–976 (1985).

[75] Y. Tanaka, Y. Himuro, R. Kainuma, Y. Sutou, T. Omori and K. Ishida, *Ferrous Polycrystalline Shape-Memory Alloy Showing Huge Superelasticity*, Science **327**, 1488–1490 (2010).

[76] J. Ma and I. Karaman, *Expanding the Repertoire of Shape Memory Alloys*, Science **327**, 1468–1469 (2010).

[77] M. E. Gruner and P. Entel, *Simulating functional magnetic materials on supercomputers*, J. Phys. Condens. Matter **21**, 293201 (2009).

[78] P. J. Webster, K. R. A. Ziebeck, S. L. Town and M. S. Peak, *Magnetic order and phase transformation in Ni_2MnGa*, Philosophical Magazine B **49**, 295 (1984).

[79] F. Heusler, Verh. Dtsch. Phys. Ges. **5**, 219 (1903).

[80] R. W. Overholser, M. Wuttig and D. A. Neumann, *Chemical ordering in Ni-Mn-Ga Heusler alloys*, Scripta Materialia **40**, 1095 (1999).

[81] A. Zheludev, S. M. Shapiro, P. Wochner and L. E. Tanner, *Precursor effects and pre-martensitic transformation in Ni_2MnGa*, Phys. Rev. B **54**, 15045–15050 (1996).

[82] P. J. Brown, J. Crangle, T. Kanomata, M. Matsumoto, K.-U. Neumann, B. Ouladdiaf and K. R. A. Ziebeck, *The crystal structure and phase transitions of the magnetic shape memory compound Ni_2MnGa*, Journal of Physics: Condensed Matter **14**, 10159 (2002).

[83] J. Pons, V. A. Chernenko, R. Santamarta and E. Cesari, *Crystal structure of martensitic phases in Ni-Mn-Ga shape memory alloys*, Acta mater. **48**, 3027–3038 (2000).

[84] B. Wedel, M. Suzuki, Y. Murakami, C. Wedel, T. Suzuki, D. Shindo and K. Itagaki, *Low temperature crystal structure of Ni-Mn-Ga alloys*, Journal of Alloys and Compounds **290**, 137–143 (1999).

[85] A. T. Zayak, W. A. Adeagbo, P. Entel and V. D. Buchelnikov, *Crystal Structures of Ni_2MnGa from Density Functional Calculations*, Phase Transitions **78**, 259–266 (2005).

[86] A. T. Zayak, P. Entel, J. Enkovaara, A. Ayuela and R. M. Nieminen, *First-principles investigations of homogeneous lattice-distortive strain and shuffles in Ni_2MnGa*, J. Phys.: Condens. Matter **15**, 159–164 (2003).

[87] V. A. Chernenko, C. Seguí, E. Cesari, J. Pons and V. V. Kokorin, *Sequence of martensitic transformations in Ni-Mn-Ga alloys*, Phys. Rev. B **57**, 2659–2662 (Feb 1998).

[88] S. Wirth, A. Leithe-Jasper, A. N. Vasilev and J. M. C. Coey, *Structural and magnetic properties of Ni_2MnGa*, Jorunal of Magnetism and Magnetic Materials **167**, L7–L11 (1997).

[89] K. Ullakko, J. K. Huang, C. Kantner, R. C. O'Handley and V. V. Kokorin, *Large magnetic-field-induced strains in Ni2MnGa single crystals*, Appl. Phys. Lett. **69**, 1966 (1996).

[90] S. Kaufmann, U. K. Rößler, O. Heczko, M. Wuttig, J. Buschbeck, L. Schultz and S. Fähler, *Adaptive Modulations of Martensites*, Phys. Rev. Lett. **104**, 145702 (Apr 2010).

[91] A. G. Khachaturyan, S. M. Shapiro and S. Semenovskaya, *Adaptive phase formation in martensitic transformation*, Phys. Rev. B **43**, 10832–10843 (May 1991).

[92] P. Entel, V. D. Buchelnikov, M. E. Gruner, A. Hucht, V. V. Khovailo, S. K. Nayak and A. T. Zayak, *Shape Memory Alloys: A Summary of Recent Achievements*, Materials Science Forum **583**, 21 (2008).

[93] L. Mañosa, A. Planes, J. Zarestky, T. Lograsso, D. L. Schlagel and C. Stassis, *Phonon softening in Ni-Mn-Ga alloys*, Phys. Rev. B **64**, 024305 (Jun 2001).

[94] A. Zheludev, S. M. Shapiro, P. Wochner, A. Schwartz, M. Wall and L. E. Tanner, *Phonon anomaly, central peak, and microstructures in Ni_2MnGa*, Phys. Rev. B **51**, 11310 (1995).

[95] C. Bungaro, K. M. Rabe and A. D. Corso, *First-principles study of lattice instabilities in ferromagnetic Ni_2MnGa*, Phys. Rev. B **68**, 134104 (2003).

[96] A. T. Zayak, P. Entel, J. Enkovaara, A. Ayuela and R. M. Nieminen, *First-principles investigation of phonon softenings and lattice instabilities in the shape-memory system* Ni_2MnGa, Phys. Rev. B **68**, 132402 (Oct 2003).

[97] A. W. Overhauser, *Structure of Nuclear Matter*, Phys. Rev. Lett. **4**, 415–418 (Apr 1960).

[98] C. M. Varma and W. Weber, *Phonon dispersion in transition metals*, Phys. Rev. B **19**, 6142–6154 (Jun 1979).

[99] S. Prakash, *Dynamics of transition metals and alloys*, Nova Science Publishers, Inc., Commack, New York 1998.

[100] Y. Lee, J. Y. Rhee and B. N. Harmon, *Generalized susceptibility of the magnetic shape-memory alloy Ni_2MnGa*, Phys. Rev. B **66**, 054424 (2002).

[101] P. J. Brown, A. Y. Bargawi, J. Crangle, K.-U. Neumann and K. R. A. Ziebeck, *Direct observation of a band Jahn-Teller effect in the martensitic phase transition of Ni_2MnGa*, J. Phys. Condens. Matter **11**, 4715–4722 (1999).

[102] M. Matsumoto, M. Ohtsuka, H. Miki, V. V. Khovailo and T. Takagi, *Ferromagnetic Shape-Memory Alloy Ni_2MnGa*, Mater. Sci. Forum **394-395**, 545–548 (2002).

[103] P. Entel, V. D. Buchelnikov, V. V. Khovailo, A. T. Zayak, W. A. Adeagbo, M. E. Gruner, H. C. Herper and E. F. Wassermann, *Modelling the phase diagram of magnetic shape memory Heusler alloys*, J. Phys. D: Appl. Phys. **39**, 865–889 (2006).

[104] V. V. Kokorin, V. A. Chernenko, J. Pons, C. Segui and E. Cesari, *Lattice instability of Ni_2MnGa*, Phys. Solid State **39**, 485–487 (1997).

[105] A. Planes, L. Mañosa and M. Acet, *Magnetocaloric effect and its relation to shape-memory properties in ferromagnetic Heusler alloys*, J. Phys.: Condens. Matter **21**, 233201 (2009).

[106] I. Takeuchi, O. O. Famodu, J. C. Read, M. A. Aronova, K.-S. Chang, C. Craciunescu, S. E. Lofland, M. Wuttig, F. C. Wellstood, L. Knauss and A. Orozco, *Identification of novel compositions of ferromagnetic shape-memory alloys using composition spreads*, Nature Mater. **2**, 180–184 (2003).

[107] N. Lanska, O. Söderberg, A. Sozinov, Y. Ge, K. Ullakko and V. K. Lindroos, *Composition and temperature dependence of the crystal structure of Ni-Mn-Ga alloys*, J. Appl. Phys. **95**, 8074 (2004).

[108] Y. Sutou, Y. Imano, N. Koeda, T. Omori, R. Kainuma, K. Ishida and K. Oikawa, *Magnetic and martensitic transformations of NiMnX(X=In, Sn, Sb) ferromagnetic shape memory alloys*, Appl. Phys. Lett. **85**, 4358 (2004).

[109] B. Himmetoglu, V. M. Katukuri and M. Cococcioni, *Origin of magnetic interactions and their influence on the structural properties of Ni_2MnGa and related compounds*, J. Phys.: Cond. Mat. **24**, 185501 (2012).

[110] A. Ayuela, J. Enkovaara and R. M. Nieminen, *Ab initio study of tetragonal variants in Ni_2MnGa alloy*, J. Phys.: Cond. Mat. **14**, 5325–5336 (2002).

[111] S. Ener, J. Neuhaus, W. Petry, R. Mole, K. Hradil, M. Siewert, I. Titov, M. E. Gruner, P. Entel and M. Acet, *Effect of temperature and compositional changes on the phonon properties of Ni-Mn-Ga shape memory alloys*, Submitted to Phys. Rev. B (2012).

[112] M. Methfessel and A. T. Paxton, *High-precision sampling for Brillouin-zone integration in metals*, Phys. Rev. B **40**, 3616–3621 (Aug 1989).

[113] A. T. Zayak, P. Entel, K. M. Rabe, W. A. Adeagbo and M. Acet, *Anomalous vibrational effects in nonmagnetic and magnetic Heusler alloys*, Phys. Rev. B **72**, 054113 (2005).

[114] A. T. Zayak, *A first-principles investigation of the magnetic, structural and dynamical properties of Ni_2MnGa*, Ph.D. thesis, Universität Duisburg-Essen 2003.

[115] T. Fukuda and T. Kakeshita, *Effect of magnetic field on martensite to intermediate phase transformation in Ni_2MnGa*, Advanced Materials Research **52**, 199–203 (2008).

[116] P. Souvatzis, O. Eriksson, M. I. Katsnelson and S. P. Rudin, *Entropy Driven Stabilization of Energetically Unstable Crystal Structures Explained from First Principles Theory*, Phys. Rev. Lett. **100**, 095901 (Mar 2008).

[117] P. Souvatzis and S. P. Rudin, *Dynamical stabilization of cubic ZrO_2 by phonon-phonon interactions: Ab initio calculations*, Phys. Rev. B **78**, 184304 (Nov 2008).

[118] P. Souvatzis, O. Eriksson, M. I. Katsnelson and S. P. Rudin, *The self-consistent ab initio lattice dynamical method*, Comp. Mater. Science **44**, 888–894 (2009).

[119] M. A. Uijttewaal, T. Hickel, J. Neugebauer, M. E. Gruner and P. Entel, *Understanding the Phase Transitions of the* Ni_2MnGa *Magnetic Shape Memory System from First Principles*, Phys. Rev. Lett. **102**, 035702 (Jan 2009).

[120] J. Enkovaara, A. Ayuela, L. Nordström and R. M. Nieminen, *Structural, thermal, and magnetic properties of Ni_2MnGa*, J. Appl. Phys. **91**, 7798 (2002).

[121] A. Ayuela, J. Enkovaara, K. Ullakko and R. M. Nieminen, *Structural properties of magnetic Heusler alloys*, J. Phys.: Condens. Matter **11**, 2017–2026 (1999).

[122] U. Stuhr, P. Vorderwisch and V. V. Kokorin, *Spin waves and phonon anomaly in the Heusler alloy Ni_2MnGa*, Physica B **234-236**, 135–136 (1997).

[123] M. E. Gruner. private communication.

[124] H. Ebert, *Fully relativistic band structure calculations for magnetic solids - Formalism and Application*, vol. 535 (Electronic Structure and Physical Properties of Solids) of *Lecture Notes in Physics*, pp. 191–246, Springer Berlin (2000).

[125] J. Zabloudil, R. Hammerling, L. Szunyogh and P. Weinberger, *Electron Scattering in Solid Matter*, Springer-Verlag Berlin Heidelberg 2005.

[126] P. Weinberger, *Electron Scattering Theory for Ordered and Disordered Matter*, Oxford University Press, New York 1990.

[127] A. Ernst. private communication.

[128] A. Ernst, *Multiple-scattering theory: new developments and applications*, habilitation thesis at the university of Halle-Wittenberg (2007).

[129] K. Schwarz and P. Mohn, *Itinerant metamagnetism in YCo_2*, J. Phys. F: Met. Phys. **14**, L129–L134 (1984).

[130] V. L. Moruzzi, P. M. Marcus, K. Schwarz and P. Mohn, *Ferromagnetic phases of bcc and fcc Fe, Co and Ni*, Phys. Rev. B **34**, 1784–1791 (1986).

[131] M. E. Gruner, W. A. Adeagbo, A. T. Zayak, A. Hucht, S. Buschmann and P. Entel, *Influence of magnetism on the structural stability of cubic $L2_1$ Ni_2MnGa*, Eur. Phys. J.: Special Topics **158**, 193 (2008).

[132] J. Wan, X. Lei, S. Chen and Z. Xu, *Phonon damping effect during the premartensitic transformation in Heusler alloy Ni_2MnGa*, Phys. Lett. A **327**, 216–220 (2004).

[133] J. F. Wan, X. L. Lei, S. P. Chen and T. Y. Hsu, *Magnon-TA phonon interaction and the specific heat during the premartensitic transformation in ferromagnetic Ni_2MnGa*, Solid State Communications **133**, 433–437 (2005).

[134] Y. Q. Fei and J. F. Wan, *Magnetic susceptibility anomaly associated with premartensitic transition in Heusler alloy*, Physica B: Condensed Matter **389**, 288–291 (2007).

[135] M. Siewert, M. E. Gruner, A. Hucht, H. C. Herper, A. Dannenberg, A. Chakrabarti, N. Singh, R. Arróyave and P. Entel, *A First-principles Investigation of the Compositional Dependent Properties of Magnetic Shape Memory Heusler Alloys*, Adv. Eng. Mater. p. accepted (2012).

[136] M. Cococcioni and S. de Gironcoli, *Linear response approach to the calculation of the effective interaction parameters in the* LDA + U *method*, Phys. Rev. B **71**, 035105 (Jan 2005).

[137] L. C. Davis and L. A. Feldkamp, *Effect of electron correlations on photoemission from narrowband metals*, J. Appl. Phys. **50**, 1944 (1979).

[138] E. Şaşıoğlu and S. Blügel. private communication.

[139] O. I. Velikokhatnyĭ and I. I. Naumov, *Electronic structure and instability of Ni_2MnGa*, Phys. Solid State **41**, 617 (1999).

[140] G.-L. Zhao, T. C. Leung, B. N. Harmon, M. Keil, M. Müllner and W. Weber, *Electronic origin of the intermediate phase of NiTi*, Phys. Rev. B **40**, 7999–8001 (Oct 1989).

[141] I. I. Naumov, O. I. Velikokhatnyĭ and V. Z. Bashirov, *Charge density waves in B2 compounds of titanium*, JETP Lett. **54**, 573 (1991).

[142] G. L. Zhao and B. N. Harmon, *Phonon anomalies in β-phase* Ni_xAl_{1-x} *alloys*, Phys. Rev. B **45**, 2818–2824 (Feb 1992).

[143] I. I. Naumov and O. I. Velikokhatniy, *Simultaneous manifestations of the 2D van Hove singularity and the Fermi surface nesting in the acoustic soft phonon mode of β-NiAl alloys*, Journal of Physics: Condensed Matter **9**, 10339 (1997).

[144] R. Peierls, *More Surprises in Theoretical Physics*, Princeton University Press 1991.

[145] M. D. Johannes and I. I. Mazin, *Fermi surface nesting and the origin of charge density waves in metals*, Phys. Rev. B **77**, 165135 (Apr 2008).

[146] E. J. Woll and W. Kohn, *Images of the Fermi Surface in Phonon Spectra of Metals*, Phys. Rev. **126**, 1693–1697 (Jun 1962).

[147] T. D. Haynes, R. J. Watts, J. Laverock, Z. Major, M. A. Alam, J. W. Taylor, J. A. Duffy and S. B. Dugdale, *Positron annihilation study of the Fermi surface of Ni_2MnGa*, New Journal of Physics **14**, 035020 (2012).

[148] C. P. Opeil, B. Mihaila, R. K. Schulze, L. Mañosa, A. Planes, W. L. Hults, R. A. Fisher, P. S. Riseborough, P. B. Littlewood, J. L. Smith and J. C. Lashley, *Combined Experimental and Theoretical Investigation of the Premartensitic Transition in Ni_2MnGa*, Phys. Rev. Lett. **100**, 165703 (Apr 2008).

[149] S.-K. Chan and V. Heine, *Spin density wave and soft phonon mode from nesting Fermi surfaces*, J. Phys. F: Met. Phys. **3**, 795 (1973).

[150] W. E. Evenson and S. H. Liu, *Theory of Magnetic Ordering in the Heavy Rare Earths*, Phys. Rev. **178**, 783–794 (Feb 1969).

[151] S. M. Shapiro, *Lattice dynamics and structural phase transitions*, Appl. Phys. A **99**, 543–548 (2010).

[152] A. T. Zayak and P. Entel, *A critical discussion of calculated modulated structures, Fermi surface nesting and phonon softening in magnetic shape memory alloys Ni_2Mn(Ga, Ge, Al) and Co_2Mn(Ga, Ge)*, Jorunal of Magnetism and Magnetic Materials **290-291**, 874–877 (2005).

[153] M. Matsumoto, T. Kanomata, T. Kaneko, T. Takagi and J. Tani, *Magnetic Property of Ni_2MnGa*, Journal of the Magnetics Society Japan **23**, 415–417 (1999).

[154] X. Q. Chen, F. J. Yang, X. Lu and Z. X. Qin, *The way composition affects martensitic transformation temperatures of Ni-Mn-Ga Heusler alloys*, phys. stat. sol. (b) **244**, 1047–1053 (2007).

[155] X. Jin, M. Marioni, D. Bono, S. M. Allen, R. C. O'Handley and T. Y. Hsu, *Empirical mapping of Ni-Mn-Ga properties with composition and valence electron concentration*, J. Appl. Phys. **91**, 8222 (2002).

[156] A. T. Zayak, W. A. Adeagbo, P. Entel and K. M. Rabe, *e/a dependence of the lattice instability of cubic Heusler alloys from first principles*, Appl. Phys. Lett. **88**, 111903 (2006).

[157] T. Krenke, E. Duman, M. Acet, E. F. Wassermann, X. Moya, L. Mañosa and A. Planes, *Inverse magnetocaloric effect in ferromagnetic Ni-Mn-Sn alloys*, Nature Mater. **4**, 450 (2005).

[158] V. D. Buchelnikov, P. Entel, S. V. Taskaev, V. V. Sokolovskiy, A. Hucht, M. Ogura, H. Akai, M. E. Gruner and S. K. Nayak, *Monte Carlo study of the influence of antiferromagnetic exchange interactions on the phase transitions of ferromagnetic Ni-Mn-X (X=In,Sn,Sb)*, Phys. Rev. B **78**, 184427 (2008).

[159] P. Lázpita, J. M. Barandiarán, J. Feuchtwanger, J. Gutiérrez, I. Rodríguez, V. A. Chernenko, A. Stunault and C. Mondelli, *Magnetic moment distribution in non-stoichiometric Ni-Mn-Ga ferromagnetic shape memory alloys*, J. Phys.: Conf. Ser. **325**, 012016 (2011).

[160] S. Aksoy, M. Acet, P. P. Deen, L. Mañosa and A. Planes, *Magnetic correlations in martensitic Ni-Mn-based Heusler shape-memory alloys: Neutron polarization analysis*, Phys. Rev. B **79**, 212401 (Jun 2009).

[161] P. E. Blöchl, O. Jepsen and O. K. Andersen, *Improved tetrahedron method for Brillouin-zone integrations*, Phys. Rev. B **49**, 16223–16233 (Jun 1994).

[162] H. J. Monkhorst and J. D. Pack, *Special points for Brillouin-zone integrations*, Phys. Rev. B **13**, 5188–5192 (1976).

[163] J. Kübler, A. R. Williams and C. B. Sommers, *Formation and coupling of magnetic moments in Heusler alloys*, Phys. Rev. B **28**, 1745 (1983).

[164] Y. Ishikawa, *Differing degrees of itinerancy in 3d alloys revealed by measurements of neutron spin wave scattering*, Physica B **91**, 130 (1977).

[165] J. S. Kasper and B. W. Roberts, *Antiferromagnetic Structure of α-Manganese and a Magnetic Structure Study of β-Manganese*, Phys. Rev. **101**, 537 (1956).

[166] J. L. Fry, Y. Z. Zhao, N. E. Brener, G. Fuster and J. Callaway, *Prediction of ferromagnetism in bcc Mn*, Phys. Rev. B **36**, 868 (1987).

[167] I. Galanakis and E. Şaşıoğlu, *Structural-induced antiferromagnetism in Mn-based full Heusler alloys: The case of Ni_2MnAl*, Appl. Phys. Lett. **98**, 102514 (2011).

[168] S. Chikazumi, *Physics of Magnetism*, R. E. Krieger Publishing Company, Huntington, New York 1978.

[169] C. Jiang, Y. Muhammad, L. Deng, W. Wu and H. Xu, *Composition dependence on the martensitic structures of the Mn-rich NiMnGa alloys*, Acta Materialia **52**, 2779–2785 (2004).

[170] S. Aksoy, M. Acet, E. F. Wassermann, T. Krenke, X. Moya, L. Mañosa, A. Planes and P. P. Deen, *Structural properties and magnetic interactions in martensitic Ni-Mn-Sb alloys*, Philosophical Magazine **89**, 2093–2109 (2009).

[171] T. Krenke, X. Moya, S. Aksoy, M. Acet, P. Entel, L. Mañosa, A. Planes, Y. Elerman, A. Yücel and E. F. Wassermann, *Electronic aspects of the martensitic transition in Ni-Mn based Heusler alloys*, J. of Magn. and Magn. Mater. **310**, 2788 (2007).

[172] J. Enkovaara, O. Heczko, A. Ayuela and R. M. Nieminen, *Coexistence of ferromagnetic and antiferromagnetic order in Mn-doped Ni_2MnGa*, Phys. Rev. B **67**, 212405 (2003).

[173] T. Büsgen, J. Feydt, R. Hassdorf, S. Thienhaus, M. Moske, M. Boese, A. Zayak and P. Entel, *Ab initio calculations of structure and lattice dynamics in Ni-Mn-Al shape memory alloys*, Phys. Rev. B **70**, 014111 (2004).

[174] M. Ye, A. Kimura, Y. Miura, M. Shirai, Y. T. Cui, K. Shimada, H. Namatame, M. Taniguchi, S. Ueda, K. Kobayashi, R. Kainuma, T. Shishido, K. Fukushima and

T. Kanomata, *Role of Electronic Structure in the Martensitic Phase Transition of* $Ni_2Mn_{1+x}Sn_{1-x}$ *Studied by Hard-X-Ray Photoelectron Spectroscopy and Ab Initio Calculation*, Phys. Rev. Lett. **104**, 176401 (Apr 2010).

[175] P. Entel, M. Siewert, M. E. Gruner, A. Chakrabarti, S. R. Barman, V. V. Sokolovskiy and V. D. Buchelnikov, *Optimization of smart Heusler alloys from first principles*, J. of Alloys and Comp. p. submitted to (2011).

[176] M. Siewert, M. E. Gruner, A. Dannenberg, A. Chakrabarti, H. C. Herper, M. Wuttig, S. R. Barman, S. Singh, A. Al-Zubi, T. Hickel, J. Neugebauer, M. Gillessen, R. Dronskowski and P. Entel, *Designing shape-memory Heusler alloys from first-principles*, Appl. Phys. Lett. **99**, 191904 (2011).

[177] A. Dannenberg, *Ab initio and Monte Carlo investigations of structural, electronic and magnetic properties of new ferromagnetic Heusler alloys with high Curie temperatures*, Ph.D. thesis, University of Duisburg-Essen 2011.

[178] M. E. Gruner and P. Entel, *Impact of local lattice distortions on the structural stability of Fe-Pd magnetic shape-memory alloys*, Phys. Rev. B **83**, 214415 (Jun 2011).

[179] W. H. Press, B. P. Flannery, S. A. Teukolsky and W. T. Vetterling, *Numerical Recipes*, Cambridge University Press 1986.

[180] M. Kallmayer, P. Pörsch, T. Eichhorn, H. Schneider, C. A. Jenkins, G. Jakob and H. J. Elmers, *Compositional dependence of element-specific magnetic moments in* Ni_2MnGa *films*, J. Phys. D: Appl. Phys. **42**, 084008 (2009).

[181] J. S. Kasper and J. S. Kouvel, *The antiferromagnetic structure of NiMn*, J. Phys. Chem. Solids **11**, 231–238 (1959).

[182] E. Krén, E. Nagy, I. Nagy, L. Pál and P. Szabó, *Structures and Phase Transformations in the Mn-Ni System near Equiatomic Concentration*, J. Phys. Chem. Solids **29**, 101–108 (1968).

[183] V. V. Godlevsky and K. M. Rabe, *Soft tetragonal distortions in ferromagnetic* Ni_2MnGa *and related materials from first principles*, Phys. Rev. B **63**, 134407 (2001).

[184] C.-M. Li, H.-B. Luo, Q.-M. Hu, R. Yang, B. Johansson and L. Vitos, *First-principles investigation of the composition dependent properties of* $Ni_{2+x}Mn_{1-x}Ga$ *shape-memory alloys*, Phys. Rev. B **82**, 024201 (Jul 2010).

[185] C. Jiang, G. Feng, S. Gong and H. Xu, *Effect of Ni excess on phase transformation temperatures of NiMnGa*, Mater. Sci. Eng.: A **342**, 231–235 (2003).

[186] Y. Kishi, Z. Yajima, K. Shimizu and M. Wuttig, *Transformation behavior and microstructures of PtNiMnGa ferromagnetic shape memory alloys*, Mater. Sci. Eng.: A **378**, 361–364 (2004).

[187] C. M. Wayman, *On memory effects related to martensitic transformations and observations in β-brass and Fe_3Pt*, Scripta Metallurgica **5**, 489–492 (1971).

[188] T. Graf, J. Casper, F. Winterlik, B. Balke, G. H. Fecher and C. Felser, *Crystal Structure of New Heusler Compounds*, Zeitschrift für anorganische und allgemeine Chemie **635**, 976–981 (2009).

[189] F. A. Hames and J. Crangle, *Ferromagnetism in Heusler-Type Alloys Based on Platinum-Group or Palladium-Group Metals*, J. Appl. Phys. **42**, 1336 (1971).

[190] E. Uhl, *Magnetic Properties of New Heusler Alloys $(Cu_{1-x}Co_x)_2MnSn$*, Journal of Magnetism and Magnetic Materials **25**, 221–227 (1981).

[191] R. Niemann, U. Rößler, M. E. Gruner, O. Heczko, L. Schultz and S. Fähler, *The Role of Adaptive Martensite in Magnetic Shape Memory Alloys*, Adv. Eng. Mater. p. doi: 10.1002/adem.201200058 (2012).

[192] V. V. Khovaylo, T. Kanomata, T. Tanaka, M. Nakashima, Y. Amako, R. Kainuma, R. Y. Umetsu, H. Morito and H. Miki, *Magnetic properties of $Ni_{50}Mn_{34.8}In_{15.2}$ probed by Mössbauer spectroscopy*, Phys. Rev. B **80**, 144409 (Oct 2009).

[193] S. Kaufmann, R. Niemann, T. T., U. K. Rößler, O. Heczko, J. Buschbeck, B. Holzapfel, L. Schultz and S. Fähler, *Modulated martensite: why it forms and why it deforms easily*, New Journal of Physics **13**, 053029 (2011).

[194] L. Righi, F. Albertini, L. Pareti, A. Paoluzi and G. Calestani, *Commensurate and incommensurate "5M" modulated crystal structures in Ni-Mn-Ga martensitic phases*, Acta Materialia **55**, 5237–5245 (2007).

[195] V. D. Buchelnikov, V. V. Sokolovskiy, H. C. Herper, H. Ebert, M. E. Gruner, S. V. Taskaev, V. V. Khovaylo, A. Hucht, A. Dannenberg, M. Ogura, H. Akai, M. Acet and P. Entel, *First-principles and Monte Carlo study of magnetostructural transition and magnetocaloric properties of $Ni_{2+x}Mn_{1-x}Ga$*, Phys. Rev. B **81**, 094411 (Mar 2010).

[196] J. Enkovaara, A. Ayuela, J. Jalkanen, L. Nordström and R. M. Nieminen, *First-principles calculations of spin spirals in Ni_2MnGa and Ni_2MnAl*, Phys. Rev. B **67**, 054417 (2003).

[197] S. Singh, K. R. A. Ziebeck, E. Suard, P. Rajput, S. Bhardwaj, A. M. Awasthi and S. R. Barman, *Modulated structure in $Ni_{1.8}Pt_{0.2}MnGa$: a neutron diffraction study*, submitted to APL (2012).

[198] H. Morito, K. Oikawa, A. Fujita, K. Fukamichi, R. Kainuma and K. Ishida, *Stress-assisted large magnetic-field-induced strain in single variant Co-Ni-Ga ferromagnetic shape memory alloy*, J. Phys.: Cond. Mat. **21**, 256002 (2009).

[199] X. Dai, G. Liu, Y. Li, J. Qu, J. Li, J. Chen and G. Wu, *Structure and magnetic properties of highly ordered Co_2NiGa alloys*, J. Appl. Phys. **101**, 09N503 (2007).

[200] J. Liu, M. Xia, Y. Huang, H. Zheng and J. Li, *Effect of annealing on the microstructure and martensitic transformation of magnetic shape memory alloys CoNiGa*, J. Alloys and Comp. **417**, 96–99 (2006).

[201] M. Siewert, M. E. Gruner, A. Dannenberg, A. Hucht, S. M. Shapiro, G. Xu, D. L. Schlagel, T. A. Lograsso and P. Entel, *Electronic structure and lattice dynamics of the magnetic shape-memory alloy Co_2NiGa*, Phys. Rev. B **82**, 064420 (Aug 2010).

[202] J. Li, Y. Li, G. Zhou, Y. Sun and C. Q. Sun, *A first principles study on the full-Heusler compound Cr_2MnAl*, Appl. Phys. Lett. **94**, 242502 (2009).

[203] N. K. Jaggi, K. R. P. M. Rao, A. K. Grover, L. C. Gupta, R. Vijayaraghavan and D. Le Khoi, *Mössbauer and NMR study of site preference and local environment effects in Co_2FeGa & Fe_2CoGa*, Hyperfine Interactions **4**, 402–406 (1978).

[204] A. Dannenberg, M. Siewert, M. E. Gruner, M. Wuttig and P. Entel, *Competing structural ordering tendencies in Heusler-type alloys with high Curie temperatures: $Fe_2CoGa_{1-x}Zn_x$ studied by first-principles calculations*, Phys. Rev. B **82**, 214421 (Dec 2010).

[205] A. Dannenberg, M. Siewert, M. E. Gruner, M. Wuttig and P. Entel, *Erratum: Competing structural ordering tendencies in Heusler-type alloys with high Curie temperatures: $Fe_2CoGa_{1-x}Zn_x$ studied by first-principles calculations [Phys. Rev. B 82, 214421 (2010)]*, Phys. Rev. B **83**, 059903 (Feb 2011).

[206] G. D. Liu, X. F. Dai, S. Y. Yu, Z. Y. Zhu, J. L. Chen, G. H. Wu, H. Zhu and J. Q. Xiao, *Physical and electronic structure and magnetism of Mn_2NiGa: Experiment and density-functional theory calculations*, Phys. Rev. B **74**, 054435 (Aug 2006).

[207] S. R. Barman and A. Chakrabarti, *Comment on "Physical and electronic structure and magnetism of Mn_2NiGa: Experiment and density-functional theory calculations"*, Phys. Rev. B **77**, 176401 (May 2008).

[208] S. R. Barman, S. Banik, A. K. Shukla, C. Kamal and A. Chakrabarti, *Martensitic transition, ferrimagnetism and Fermi surface nesting in Mn_2NiGa*, EPL (Europhysics Letters) **80**, 57002 (2007).

[209] M. Gillessen and R. Dronskowski, *A Combinatorial Study of Inverse Heusler Alloys by First-Principles Computational Methods*, J. Comput. Chem. **31**, 612 (2009).

[210] H. C. Kandpal, G. H. Fecher and C. Felser, *Calculated electronic and magnetic properties of the half-metallic, transition metal based Heusler compounds*, J. Phys. D: Appl. Phys. **40**, 1507–1523 (2007).

[211] R. Arróyave, A. Junkaew, A. Chivukula, S. Bajaj, C.-Y. Yao and A. Garay, *Investigation of the structural stability of Co_2NiGa shape memory alloys via ab initio methods*, Acta Materialia **58**, 5220–5231 (2010).

[212] M. Siewert, M. E. Gruner, A. Dannenberg and P. Entel, *Structure, lattice dynamics and Fermi surface of the magnetic shape memory systems Co-Ni-Ga from first principles calculations*, Physics Procedia **10**, 138–143 (2010).

[213] C. M. Craciunescu, Y. Kishi and M. Wuttig, *Cobalt-base ferromagnetic shape memory alloys*, Proc. SPIE **4699**, 235 (2002).

[214] C. Craciunescu, Y. Kishi, T. A. Lograsso and M. Wuttig, *Martensitic transformation in Co_2NiGa ferromagnetic shape memory alloys*, Scripta Materialia **47**, 285 (2002).

[215] R. Ducher, R. Kainuma and K. Ishida, *Phase equilibria in the Ni-Co-Ga alloy system*, Journal of Alloys and Compounds **466**, 208 (2008).

[216] K. Oikawa, T. Ota, Y. Imano, T. Omori, R. Kainuma and K. Ishida, *Phase equilibria and phase transformation of Co-Ni-Ga ferromagnetic shape memory alloy system*, J. Phase Equilib. Diffus. **27**, 75 (2006).

[217] M. Zhang, E. Brück, F. R. de Boer and G. Wu, *Magnetic martensitic transformation, magnetostriction and shape memory effect in $Co_{50}Ni_{20}Ga_{30}$ melt-spun ribbons*, J. Phys. D: Appl. Phys. **38**, 1361 (2005).

[218] J. Dadda, H. J. Maier, I. Karaman, H. E. Karaca and Y. I. Chumlyakov, *Pseudoelasticity at elevated temperatures in [001] oriented $Co_{49}Ni_{21}Ga_{30}$ single crystals under compression*, Scripta Materialia **55**, 663–666 (2006).

[219] V. Popescu and A. Zunger, *Extracting E versus $\vec{k}$ effective band structure from supercell calculations on alloys and impurities*, Phys. Rev. B **85**, 085201 (Feb 2012).

[220] N. Singh, E. Dogan, I. Karaman and R. Arróyave, *Effect of configurational order on the magnetic characteristics of Co-Ni-Ga ferromagnetic shape memory alloys*, Phys. Rev. B **84**, 184201 (Nov 2011).

[221] S. Sarma and S. Srinivasan, *Structural characterization of $Co_{70-x}Ni_xGa_{30}$ ferromagnetic shape memory alloys*, Adv. Mater. Res. **52**, 103–108 (2008).

[222] Y. Li, C. Jiang, T. Liang, Y. Ma and H. Xu, *Martensitic transformation and magnetization of Ni-Fe-Ga ferromagnetic shape memory alloys*, Scripta Materialia **48**, 1255–1258 (2003).

[223] P. Soven, *Coherent-Potential Model of Substitutional Disordered Alloys*, Phys. Rev. **156**, 809–813 (Apr 1967).

[224] M. Friák and M. Šob, *Ab initio study of the bcc-hcp transformation in iron*, Phys. Rev. B **77**, 174117 (May 2008).

[225] A. Kokalj, *Computer graphics and graphical user interfaces as tools in simulations of matter at the atomic scale*, Comp. Mater. Sci. **28**, 155–168 (2003).

[226] K. Momma and F. Izumi, *VESTA: a three-dimensional visualization system for electronic and structural analysis*, J. Appl. Crystallogr. **41**, 653–658 (2008).

List of own publications

Parts of the results which have been presented here have also been published in the following articles:

- S. Ener, J. Neuhaus, W. Petry, R. Mole, K. Hradil, M. Siewert, I. Titov, M. E. Gruner, P. Entel, and M. Acet, *Effect of temperature and compositional changes on the phonon properties of Ni-Mn-Ga shape memory alloys*, submitted to Phys. Rev. B

- P. Entel, S. Sahoo, M. Siewert, M. E. Gruner, H. C. Herper, D. Comtesse, M. Acet, V. D. Buchelnikov, and V. V. Sokolovskiy, *First-principles investigations of caloric effects in ferroic materials*, AIP Conf. Proc. **1461**, 11-23 (2012)

- M. Siewert, M. E. Gruner, A. Hucht, H. C. Herper, A. Dannenberg, A. Chakrabarti, N. Singh, R. Arróyave, and P. Entel, *A First-principles Investigation of the Compositional Dependent Properties of Magnetic Shape Memory Heusler Alloys*, Adv. Eng. Mater., in press

- P. Entel, M. E. Gruner, A. Hucht, A. Dannenberg, M. Siewert, H. C. Herper, T. Kakeshita, T. Fukuda, V. V. Sokolovskiy, and V. D. Buchelnikov, *Phase Diagrams of Conventional and Inverse Functional Magnetic Heusler Alloys: New Theoretical and Experimental Investigations*, Springer Series in Materials Science **148**, Springer, Berlin Heidelberg, pp. 19-47 (2012)

- P. Entel, M. Siewert, M. E. Gruner, A. Chakrabarti, S. R. Barman, V. V. Sokolovskiy, and V. D. Buchelnikov, *Optimization of smart Heusler alloys from first principles*, J. All. Comp., in press

- P. Entel, A. Dannenberg, M. Siewert, H. C. Herper, M. E. Gruner, D. Comtesse, H.-J. Elmers, and M. Kallmayer, *Basic Properties of Magnetic Shape-Memory Materials from First-Principles Calculations*, Metal. Mater. Trans. A **43**, 2891-2900 (2012)

- M. Siewert, M. E. Gruner, A. Dannenberg, A. Chakrabarti, H. C. Herper, M. Wuttig, S. R. Barman, S. Singh, A. Al-Zubi, T. Hickel, J. Neugebauer, M. Gillessen, R. Dronskowski, and P. Entel, *Desiginin shape-memory Heusler alloys from first-principles*, Appl. Phys. Lett. **99**, 191904 (2011)

- P. Entel, A. Dannenberg, M. Siewert, H. C. Herper, M. E. Gruner, V. D. Buchelnikov, and V. A. Chernenko, *Composition-Dependent Basics of Smart Heusler Materials from First-Principles Calculations*, Mater. Sci. Forum **684**, 1 (2011)

- M. Siewert, M. E. Gruner, A. Dannenberg, A. Hucht, S. M. Shapiro, G. Xu, D. L. Schlagel, T. A. Lograsso, and P. Entel, *Electronic structure and lattice dynamics of the magnetic shape-memory alloy Co_2NiGa*, Phys. Rev. B **82**, 064420 (2010)

- P. Entel, M. E. Gruner, A. Dannenberg, M. Siewert, S. K. Nayak, H. C. Herper, and V. D. Buchelnikov, *Fundamental Aspects of Magnetic Shape Memory Alloys: Insights from Ab Initio and Monte Carlo Studies*, Mater. Sci. Forum **635**, 3 (2010)

- P. Entel, M. Siewert, A. Dannenberg, M. E. Gruner, and M. Wuttig, *New Functional Magnetic Shape Memory Alloys from First-Principles Calculations*, MRS Symp. Proc. **1200E**, 1200-G04-01 (2010)

- M. Siewert, M. E. Gruner, A. Dannenberg, and P. Entel, *Structure, lattice dynamics and Fermi surface of the magnetic shape memory system Co-Ni-Ga from first-principles calculations*, Physics Procedia **10**, 138-143 (2010)

In addition, the following articles have been published in relationship with the work that has been presented here:

- A. Grünebohm, M. Siewert, C. Ederer, and P. Entel, *First-Principles Study of the Influence of (110) Strain on the Ferroelectric Trends of TiO_2*, Ferroelectrics **429**, 31-42 (2012)

- P. Entel, D. Comtesse, H. C. Herper, M. E. Gruner, M. Siewert, S. Sahoo, and A. Hucht, *Ab-initio modeling of Fe-Mn based alloys and nanoclusters*, MRS Symp. Proc. **1296**, mrsf10-1296-o04-01 (2011)

- A. Dannenberg, M. Siewert, M. E. Gruner, M. Wuttig, and P. Entel, *Competing structural ordering tendencies in Heusler-type alloys with high Curie temperatures: $Fe_2CoGa_{1-x}Zn_x$ studied by first-principles calculations*, Phys. Rev. B **82**, 214421 (2010)

- A. Dannenberg, M. Siewert, M. E. Gruner, M. Wuttig, and P. Entel, *Structural ordering tendencies in the new ferromagnetic Ni-Co-Fe-Ga-Zn Heusler alloys*, Physics Procedia **10**, 144-148 (2010)

- A. Grünebohm, M. Siewert, H. C. Herper, M. E. Gruner, and P. Entel, *A comparative study of the (Fe, Fe_3Si)/GaAs and Heusler/MgO for spintronics applications*, J. Phys.: Conf. Ser. **200**, 072038 (2010)

Erklärung

Ich versichere, dass ich diese Arbeit selbstständig verfasst und keine anderen als die angegebenen Quellen und Hilfsmittel benutzt und alle wörtlich oder inhaltlich übernommenen Stellen als solche kenntlich gemacht habe.

Duisburg, im Juli 2012

Mario Siewert

Acknowledgements

First of all I would like to thank Professor Entel for giving me the opportunity to work on the interesting topic that has been treated within this thesis and especially for the opportunity to visit a lot of conferences and scientific researchers around Europe. I also would like to thank the people from the group of Professor Entel for fruitful discussions and valuable advices. In this context Markus E. Gruner, Heike C. Herper, and Fred Hucht deserve special credits. A special compliment also goes out to Denis Comtesse for a lot of interesting but also entertaining discussions. As someone had to pay for the obtained results, funding from the DFG, the university of Duisburg-Essen, the WE-Heraeus foundation, my parents, and Karin is grateful acknowledged. I also have to acknowledge to all collaborators who worked together with me on different topics for the experience I obtained during these very nice times. I also would like to thank my parents, not only because they gave me the opportunity to study physics. Figure 7.1 has been created using XCRYSDEN [225]. Figures 3.4, 5.1, 6.2, and 7.2 (b) have been created using VESTA [226].

Finally, I dedicate this work to Marijke and Johanna.